University of London
Imperial College of Science and Technology
Blackett Laboratory

OPTICAL PROPERTIES OF MOLTEN PHOSPHORUS SESQUISULPHIDE AND CHALCOGENIDE IODIDES OF ARSENIC

by

ALAN RICHARD HEDGES

Thesis submitted for the degree of Doctor of Philosophy of the University of London (1987)

ABSTRACT

A refractometer has been modified to enable the measurement of optical properties of melts at temperatures up to 480 deg. C., and to safely confine toxic samples at these elevated temperatures. The experiment is computer automated, which allows the measurement of refractive indices, of a prism shaped sample, over a wavelength range 1.8 to 0.4 microns. The Refractometer can be easily adapted to measure optical absorption coefficients, up to 70 cm^{-1} , from the transmission through a thin sample layer.

Phosphorus Sesquisulphide, with its low auto-ignition temperature of 100 deg. C., was used to test the safe confinement of samples. An industrial sample was purified and the optical properties investigated over its liquid temperature range 190 deg. C to 370 deg. C. The sample is transparent down to 0.5 microns and the refractive index at 1.0 micron varies from 1.80 to 1.90 within the temperature range.

The general behaviour and optical properties of Chalcogenide Glasses have been reviewed and measurements made on some As-S-I glasses. The As-S-I ternary system has an extensive area of low melting point glasses which allowed a systematic investigation of its optical properties, and density, as a function of atomic composition. The prepared samples were red in colour with melting points ranging from 200 deg. C. to as low as room temperature. Their refractive indices varied with composition, ranging from 2.00 at low

arsenic content to 2.24 with high arsenic content (both measurements for 1 micron at 200 deg. C.). A brief study of the As-Se-I system was also undertaken in the region of the equiatomic composition. These melts had good infrared transmission and high refractive indices, (~2.3) however, they tended to crystallise producing a cut-off in transmission.

CONTENTS

	Page No
ABSTRACT	i
INTRODUCTION	2
CHAPTER 1: Introductory Theory	
Section 1: Theory of Absorption and Dispersion	5
Section 2: Band Theory for Solids	22
CHAPTER 2: Experimental Details	30
CHAPTER 3: Optical Properties of Phosphorus Sesquisulphide	59
CHAPTER 4: Chalcogenide Glasses	76
CHAPTER 5: Optical Properties of Chalcogenide Iodides of Arsenic	90
Section 1: Arsenic Sulphur Iodine System	91
Section 2: Arsenic Selenium Iodine System	129
CHAPTER 6: Summary and Conclusions	147
REFERENCES	151
ACKNOWLEDGEMENTS	154

INTRODUCTION

Since well into the last century, the measurement of optical properties has given information on microscopic structure and the behaviour of atoms in oscillating electric fields. Derived permanent dipole moments provide a criterion for choosing between possible molecular structures whilst band gap information enable better parameters to be inserted into theoretical frameworks. Early investigations were usually confined to a few wavelengths in the visible region, where suitable monochromatic sources had been developed. With the advent of stable sources, solid state and infrared detectors it became possible to measure the refractive index and absorption spectrum not only for visible light, but also into the infrared and ultraviolet regions. Despite the availability of such detectors, there is a scarcity of data on optical properties in the liquid state. This is undoubtedly due to the technical difficulties in making optical measurements on liquids at elevated temperatures. The liquid, which may be toxic or corrosive, must be safely confined within a sealed cell. This cell must incorporate optical windows, and not suffer deformation or leakage when heated.

A computer automated refractometer which measures the refractive index, of low melting point melts, as a function of wavelength (1.8 - 0.14 μm) was designed and constructed by A. Donaldson (1983). Using this refractometer we have studied the optical properties of molten phosphorus

sesquisulphide and of chalcogenide iodides of arsenic. A significant part of our work involved designing a cell heating mechanism, which would extend the working temperature range, enabling measurements up to 480 deg C; and would also safely confine highly flammable and toxic samples such as those studied here. A description of the refractometer and experimental details are contained in chapter 2 of this thesis, together with a discussion of the errors involved in the cell alignment.

Chapter 1 considers the response of a medium to electromagnetic radiation and introduces the concepts of complex refractive index, frequency dependent polarisation mechanisms and the dispersion equation. Section 2 of this chapter describes the band theory for solids and illustrates the relation between optical measurements, band gap information and conduction properties of materials.

In chapter 3 we present our experimental results on phosphorus sesquisulphide which was investigated as part of the safety refinements on our cell design. The structure and properties of P_4S_3 are also discussed here, together with a brief discussion and analysis of the results.

Chapter 4 contains a review of chalcogenide glasses, discussing their general and infrared transmitting properties. Chapter 5 presents a more detailed study of two ternary chalcogenide glass systems; Section 1 of this chapter covers the Arsenic-Sulphur-Iodine system which has a large area of glass forming compounds. A systematic study of the variation in optical properties, as a function of

composition, was made for this glass system, and the results are also presented here. Section 2 describes the Arsenic-Selenium-Iodine glass system for which a brief study of the optical properties around the equiatomic composition was made.

Finally in chapter 6 we summarize the important features of our work, and make appropriate concluding remarks.

CHAPTER 1

INTRODUCTORY THEORY

SECTION 1: THEORY OF ABSORPTION AND DISPERSION

The Dielectric Constant, Refractive Index and Optical Absorption Coefficient

The response of a medium to electromagnetic radiation is described by the dielectric constant, however from a microscopic point of view the charges of the medium respond to the influence of the oscillating electric field. The wave equation for this electric field, propagating in a non magnetic energy absorbing medium can be obtained from the differential form of Maxwell's Equations.

$$\nabla^2 \underline{E} - \sigma \mu_0 \frac{d\underline{E}}{dt} - \mu_0 \varepsilon \varepsilon_0 \frac{d^2\underline{E}}{dt^2} = 0 \qquad 1.01$$

where ε = The dielectric constant

σ = The conductivity at optical frequencies

μ_0 = The permeability of free space

ε_0 = The permittivity of free space

The solution of this wave equation may be written:-

$$E = E_0 \exp i [\hat{q}.r - \omega t] \qquad 1.02$$

where the wavevector, $\hat{q}$, must be complex to describe energy dissipation of the wave.

Substituting the solution back into the wave equation gives:-

$$\hat{q}^2 = \frac{\omega^2}{c^2}\left(\varepsilon + \frac{i\sigma}{\omega\varepsilon_0}\right) \qquad 1.03$$

We can now define the complex dielectric constant $\hat{\varepsilon} = \varepsilon_1 + i\varepsilon_2$ and the complex refractive index $\hat{n} = n + ik$ such that:-

$$\hat{q} = \frac{\omega}{c}\hat{n} \quad \text{and} \quad \hat{q}^2 = \frac{\omega^2}{c^2}\hat{\varepsilon} \qquad 1.04$$

where ε_1 = the ε in equation 1.03

$\varepsilon_2 = \sigma/\omega\varepsilon_0$

n = the refractive index

k = the extinction coefficient

Rewriting equation 1.02 now gives:-

$$\underline{E} = \underline{E}_0 \left[\text{Exp} - \left(\frac{\omega}{c}\,\underline{k}\cdot\underline{r}\right)\right] \text{Exp}\, i\left(\frac{\omega}{c}\,\underline{n}\cdot\underline{r} - \omega t\right) \qquad 1.05$$

The first exponential factor describes the attenuation of the wave. The absorption coefficient, α, is defined by:-

$$I = I_0 \exp(-\alpha z) \qquad 1.06$$

where I_0 = Incident Intensity

I = Transmitted Intensity

Z = Thickness

Since the intensity is proportional to the square of the wave amplitude we can deduce:-

$$\alpha = \frac{2\omega k}{c} = \frac{4\pi k}{\lambda} \qquad 1.07$$

The second exponential factor describes a wave travelling with phase velocity c/n, hence the earlier identification of n as the refractive index.

Recalling equation 1.03 for the complex wavevector and comparing coefficients with the complex refractive index:-

$$\hat{q}^2 = \frac{\omega^2}{c^2}\left(\varepsilon + \frac{i\sigma}{\omega\varepsilon_0}\right) = \frac{\omega^2}{c^2}(n+ik)^2 \qquad 1.08$$

Hence $$\varepsilon = n^2 - k^2 = \varepsilon_1 \qquad 1.09$$

$$\frac{\sigma}{\omega\varepsilon_0} = 2nk = \varepsilon_2 \qquad 1.10$$

For a non absorbing medium the extinction coefficient is zero and the refractive index may then be calculated, from the refraction through a prism, using Snell's Law. A more complicated situation exists for absorbing media in that the two parameters, n and k, must be determined, and the experimentally measurable properties are generally

functions of both these parameters. In our experiment, k is low enough to allow some measurable transmission. The refraction at the boundary of the absorber is complicated in that Snell's Law involves the complex refractive index, which in turn requires the introduction of a complex angle of refraction. It can be shown (T.S. Moss, 1959) that for $k^2 << n^2$ the measured real angle of the refracted ray, χ is given by:-

$$\text{Sin}\,\theta \approx n\left[1 + \frac{k^2}{2n^4}\right]\text{Sin}\,\chi \qquad 1.11$$

where θ is the angle of incidence.

In our experimental arrangement it is not possible to measure transmittance when $k \geq 10^{-3}$ and therefore, by measuring the refractive index in exactly the same way as for non absorbing media, the error is only of the order 10^{-7}.

The measurement of the other parameter, k, is done by a two stage transmission experiment through a sample of small thickness.

Polarization

When a dielectric is subjected to an applied electric field the internal charge structure will experience time varying forces. These forces can generate electric dipole

moments and align permanent dipole moments which in turn contribute to the total internal field. For most materials the resultant dipole moment per unit volume is proportional to the applied field, E.

$$E\,(\varepsilon - 1)\,\varepsilon_0 = P \qquad 1.12$$

Orientational Polarisation: Polar molecules have a permanent dipole moment as a result of unequal sharing of valence electrons, eg. H_2O . The molecular dipoles are randomly orientated due to thermal agitation, however an applied electric field will align the dipoles and the dielectric will take on an orientational polarisation.

Electronic Polarisation: In non polar molecules and atoms the applied field distorts the electron cloud thereby producing a dipole moment.

Ionic or Atomic Polarisation: With the introduction of an electric field, the positive and negative ions of an ionic crystal (eg. NaCl) undergo a displacement with respect to each other, hence dipole moments are induced.

The frequency dependence of these different polarisation mechanisms can be illustrated by considering the H_2O water molecule. At high driving frequencies, polar molecules are unable to follow the alternating field, due to their relatively large moments of inertia; hence their contribution to the polarisation decreases. This is evident

in water, where the relative permittivity of water is fairly constant at approximately 80, up to about 10^{10} Hz, after which it falls off quite rapidly. Electrons have little inertia and can continue to follow the alternating field even at optical frequencies, (of about 5 x 10^{14} Hz). The characteristic frequencies of these contributions to the polarisability, and to the dielectric constant, are illustrated in Figure 1.01.

The interaction of light with matter is fully described by Quantum Mechanics. However a simple classical treatment, the Lorentz Oscillator, leads to very similar results and provides a useful conceptual model.

$$\underline{P} = \underline{P}_e + \underline{P}_a + \underline{P}_\mu$$

$\underline{P}_e$ = Electronic polarisation due to displacement of the electron distribution.

$\underline{P}_a$ = Atomic polarisation due to displacement of charged atomic groups relative to each other.

$\underline{P}_\mu$ = Polarisation due to orientation of permanent dipoles.

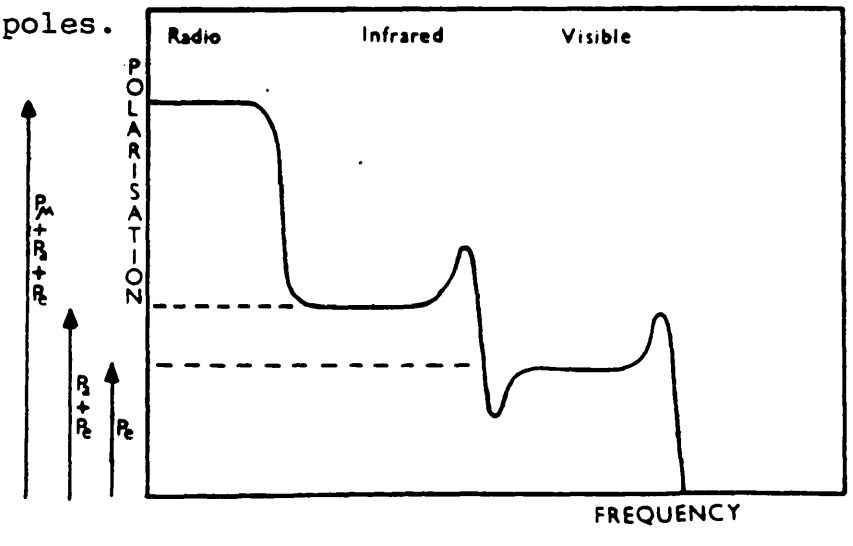


Figure 1.01 Frequency Dependence of Contributions to the Polarisability

Lorentz Oscillator Model

Consider an atom with electrons bound to the nucleus in much the same way as a small mass can be bound to a large mass by a spring. The motion of an electron bound to the nucleus is then described by:-

$$m \frac{d^2\hat{r}}{dt^2} + m\Gamma\frac{d\hat{r}}{dt} + m\omega_0^2\hat{r} = -e\underline{E}_{loc} \qquad 1.13$$

where m is the electronic mass

e is the magnitude of electronic charge

$\underline{E}_{loc}$ is the local electric field acting on the electron

the term $m\Gamma\frac{d\hat{r}}{dt}$ represents viscous damping and $m\omega_0^2\underline{r}$ is a Hooke's Law restoring force.

The local field can be taken to vary in time as $e^{-i\omega t}$, thus the solution to equation 1.13 is:-

$$\hat{r} = \frac{-e\underline{E}_{loc}/m}{(\omega_0^2 - \omega^2) - i\Gamma\omega} \qquad 1.14$$

and the induced dipole moment, P, equals

$$\hat{P} = -e\hat{r} = \frac{e^2}{m}\underline{E}_{loc}\ \frac{1}{(\omega_0^2 - \omega^2) - i\Gamma\omega} \qquad 1.15$$

Now assume that the displacement, r, is sufficiently small that there is a linear relationship between the induced dipole moment and the acting field:-

$$\hat{\underline{P}} = \hat{\alpha}(\omega)\,\underline{E}_{loc} \qquad 1.16$$

where $\hat{\alpha}(\omega)$ is the frequency dependent electronic polarisability and is complex due to the inclusion of a damping term. The polarisability can be extracted from equations 1.15 and 1.16

$$\hat{\alpha}(\omega) = \frac{e^2}{m}\,\frac{1}{(\omega_0^2 - \omega^2) - i\Gamma\omega} \qquad 1.17$$

If there are Nj electrons per unit volume bounded by springs of characteristic frequency ω_j the polarisation is:-

$$\hat{\underline{P}} = \sum_j N_j \hat{\alpha}_j(\omega)\,\underline{E}_{loc} \qquad 1.18$$

where $N = \sum_j N_j$ is the total number of electrons per unit volume.

The internal electric field $\underline{E}$ is the difference between the field $\hat{\underline{D}}/\varepsilon_0$, which would exist in the absence of polarisation, and the field $\hat{\underline{P}}/\varepsilon_0$ arising from polarisation.

$$\text{ie} \quad \underline{E} = \hat{\underline{D}}/\varepsilon_0 - \hat{\underline{P}}/\varepsilon_0 \qquad 1.19$$

For a homogeneous, linear, isotropic dielectric $\underline{P}$ and $\underline{E}$ are proportional, therefore $\underline{D}$ is also proportional to $\underline{E}$

$$\underline{D} = \varepsilon \varepsilon_0 \underline{E} = \varepsilon_0 \underline{E} + \underline{P} \qquad 1.20$$

Substituting the polarisation, equation 1.18, into the above relation for the complex electric displacement, $\hat{\underline{D}}$, gives:-

$$\hat{\varepsilon} \varepsilon_0 \underline{E} = \varepsilon_0 \underline{E} + \sum_j N_j \hat{\alpha}_j (\omega) E_{loc} \qquad 1.21$$

giving the complex dielectric constant as

$$\hat{\varepsilon} = 1 + \frac{1}{\varepsilon_0} \frac{\underline{E}_{loc}}{\underline{E}} \sum_j N_j \hat{\alpha}_j (\omega) \qquad 1.22$$

Recalling equation 1.17 for the polarisability $\hat{\alpha}(\omega)$ and substituting we obtain

$$\hat{\varepsilon} = \varepsilon_1 + i\varepsilon_2 = 1 + \frac{e^2}{m \varepsilon_0} \frac{\underline{E}_{loc}}{\underline{E}} \sum_j \frac{1}{(\omega_j^2 - \omega^2) - i\Gamma_j \omega} \qquad 1.23$$

We can now express the refractive index and the extinction coefficient in terms of the assembly of Lorentz Oscillators

$$n^2 - k^2 = \varepsilon_1 = 1 + \frac{e^2}{m\varepsilon_0} \frac{E_{loc}}{E} \sum_j \frac{N_j (\omega_j^2 - \omega^2)}{(\omega_j^2 - \omega^2)^2 + \Gamma_j^2 \omega^2} \qquad 1.24$$

$$2nk = \varepsilon_2 = \frac{e^2}{m\varepsilon_0} \frac{E_{loc}}{E} \sum_j \frac{N_j \Gamma_j \omega}{(\omega_j^2 - \omega^2)^2 + \Gamma_j^2 \omega^2} \qquad 1.25$$

For a complete description of the interaction of light with matter we must use Quantum Mechanics. The quantum mechanically derived equation corresponding to equation 1.23 is shown by Wooten (1972) to be:-

$$\hat{\varepsilon} = 1 + \frac{e^2}{m\varepsilon_0} \frac{E_{loc}}{E} \sum_j \frac{N f_j}{(\omega_j^2 - \omega^2) - i\Gamma_j \omega} \qquad 1.26$$

This close similarity explains why the simple classical model gives such good results, however, some of the corresponding terms are quite different. Classically ω_j is the resonance frequency of a bound electron whereas in Equation 1.26 it is the transition frequency of an electron between two atomic states separated in energy by $h\omega_j$. The parameter fj is a measure of the relative probability of a quantum mechanical transition and is called the oscillator strength.

The Internal Field and Dielectric Models

The frequency dependence of contributions to the polarisability were illustrated in Figure 1.01. At a frequency high enough that the contribution from orientational and atomic polarisations are insignificant, we can extract the frequency dependent electronic polarisation $\underline{P}_e(\omega)$.

From equation 1.20 for the displacement, D, we have:-

$$D = \varepsilon \varepsilon_0 \underline{E} = \varepsilon_0 \underline{E} + \underline{P} = \varepsilon_0 \underline{E} + \sum_j N_j \hat{\alpha}_j(\omega) \underline{E}_{loc} \qquad 1.27$$

which gives

$$\hat{\underline{P}}_e(\omega) = \varepsilon_0 \underline{E} \, (\hat{\varepsilon}(\omega) - 1) = \sum_j N_j \hat{\alpha}_{ej}(\omega) \underline{E}_{loc\,j} \qquad 1.28$$

Below the onset of absorption $\varepsilon(\omega) = n^2(\omega)$ so we can write equation 1.28 as:-

$$\underline{P}_e(\omega) = \varepsilon_0 \underline{E} \, (n^2(0) - 1) = \sum_j N_j \alpha_{ej}(\omega) \underline{E}_{loc\,j} \qquad 1.29$$

Quantum mechanically we can calculate this polarisability at any frequency. But, as we shall see later, it is convenient and useful to use the optical refractive index extrapolated to zero frequency.

Recall equation 1.26 for the Quantum Mechanically derived dielectric constant, then the real part, ε_1 , is given by

$$\varepsilon_1 = n^2 - k^2 = 1 + \frac{e^2}{m\varepsilon_0} \frac{E}{E}_{loc} \sum_j \frac{N_j f_j (\omega_j^2 - \omega^2)}{(\omega_j^2 - \omega^2)^2 + \Gamma_j^2 \omega^2} \qquad 1.30$$

where the subscript j labels a transition between two particular electronic levels.

As $\omega \Rightarrow 0$ the refractive index reaches a constant long wavelength value, it is this undispersed value that we call the zero frequency refractive index. One method of extrapolating optical measurements to obtain the zero frequency value is by using the single oscillator dispersion equation:-

At frequencies well below the onset of absorption, ie. $\omega << \omega_j$ for all ω_j, we can rewrite equation 1.30 as

$$n^2(\omega) - 1 = \frac{e^2}{m\varepsilon_0} \frac{E}{E}_{loc} \sum_j \frac{N_j f_j (\omega_j^2 - \omega^2)}{(\omega_j^2 - \omega^2)^2 + \Gamma_j^2 \omega^2} \qquad 1.31$$

As $\omega \Rightarrow 0$ the summation simplifies to give

$$n^2(\omega) - 1 = \frac{e^2}{m\varepsilon_0} \frac{E_{loc}}{E} \sum_j \frac{N_j f_j}{\omega_j^2 - \omega^2} \qquad 1.32$$

Mathematically it can be shown that for $x \ll$ all x_j

$$\sum_j \frac{C_j}{x_j^2 - x^2} = \frac{D}{F^2 - x^2} \qquad 1.33$$

Wemple and DiDomenico (1969) used this relation to equate equation 1.32 to a single oscillator expression containing two energy parameters E_d and E_0:

$$n^2(E) - 1 = \frac{E_d E_0}{E_0^2 - E^2} \quad ; \quad \begin{matrix} E = \hbar\omega \\ D = E_d E_0 \\ F = E_0 \end{matrix} \qquad 1.34$$

where any local field effects and transition probabilities have been taken into the constant D.

By plotting graphs of $(n^2(E) - 1)^{-1}$ against E^2, experimental dispersion data from a wide range of materials are found to obey equation 1.34. This straight line graph also enables the two energy parameters, E_d and E_0, to be calculated. E_0 is independent of the scale of $\varepsilon_2(E)$, it is

consequently an average energy gap and can be seen to weight the values of $\varepsilon_2(E)$ most heavily near the absorption threshold. E_0 is directly proportional to the scale of $\varepsilon_2(E)$ and is therefore some measure of the total transition strength ie. it contains the number density of oscillators as well as any local field effects.

The calculation of polarisabilities also requires that the internal field at the site of the j'th particle be known. For gases at low pressure the molecules are far apart and do not polarise each other strongly, therefore we can take the internal field E_{loc} to be equal to the macroscopic field E. For liquids and solids however this internal field has always been one of the major problems in the theory of electric polarisation.

The Lorentz Field

For non-polar dielectrics good results are obtained when the Lorentz model is used for the internal field. Lorentz calculated the internal field in homogeneously polarised matter as the field in a virtual spherical cavity, this virtual cavity is formed by removing material only after all charges have been frozen in position. The field in such a cavity differs from that in a real cavity because the polarisation does not adjust itself to the presence of the cavity and is therefore homogeneous, Figure 1.02.

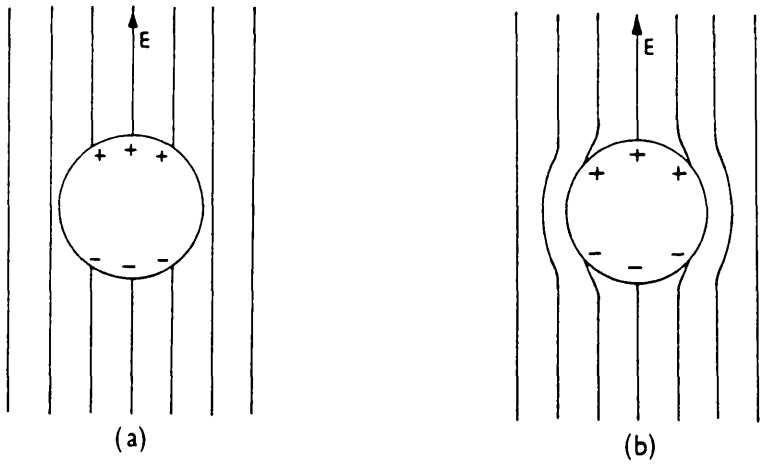


Figure 1.02: Electric field in (a) a virtual and (b) a real cavity

The field in a virtual spherical cavity is the sum of the Maxwell field E caused by the external charges, and of the field Esph induced by the apparent charges on the boundary of the cavity.

$$\text{ie} \quad \underline{E}_{loc} = \underline{E} + \underline{E}_{sph} \qquad 1.35$$

It can be shown that $\underline{E}_{sph}$ is parallel to P with magnitude:-

$$\underline{E}_{sph} = \frac{P}{3\varepsilon_0} \qquad 1.36$$

Substituting for $\underline{P}$, from equation 1.20, gives:-

$$\underline{E}_{sph} = \frac{\underline{E}(\varepsilon - 1)}{3} \qquad 1.37$$

Hence

$$\underline{E}_{loc} = \underline{E} + \frac{\underline{E}(\varepsilon - 1)}{3} = \frac{\underline{E}(\varepsilon + 2)}{3} \qquad 1.38$$

In addition to the Lorentz field the internal field at the site of a central molecule will have a contribution $\underline{E}_{dip}$ from all the dipoles that were removed in forming the virtual cavity. The internal field is therefore $\underline{E}_i = \underline{E}_{loc} + \underline{E}_{dip}$. For a cubical array of identical molecules, or if their distribution is completely random, the field $\underline{E}_{dip}$ becomes zero. In general neither of these conditions will apply, however the Lorentz field does describe the behaviour of non-polar dielectrics fairly well.

If we recall equation 1.28 for the frequency dependent electronic polarisation, then using the Lorentz field we obtain the Optical Frequency Clausius-Mossotti formula for non polar dielectrics.

$$\frac{\varepsilon(\omega) - 1}{\varepsilon(\omega) + 2} = \frac{1}{3\varepsilon_0} \sum_j N_j \alpha_{e_j}(\omega) \qquad 1.39$$

The dielectric constant at optical frequencies almost entirely arises from electronic polarisation mechanisms. This allows measured values of the dielectric constant to be extrapolated to zero frequency, giving $\varepsilon^*(0)$.

$$\frac{\varepsilon^{*}(0)-1}{\varepsilon^{*}(0)+2} = \frac{1}{3\varepsilon_0}\sum_j N_j \alpha_{e_j}(\omega) \qquad 1.40$$

Below the onset of absorption $\varepsilon(\omega) = n^2(\omega)$, so we can write equation 1.40 as:-

$$\frac{n^{*2}(0)-1}{n^{*2}(0)+2} = \frac{1}{3\varepsilon_0}\sum_j N_j \alpha_{e_j}(\omega) \qquad 1.41$$

n*(0) is the optical refractive index extrapolated to zero frequency and Nj is the number of particles of the j'th kind per unit volume. Therefore for one species we can rewrite equation 1.41 as:-

$$Rm = \frac{M}{\rho}\,\frac{n^{*2}(0)-1}{n^{*2}(0)+2} = \frac{N_A \alpha_e}{3\varepsilon_0} \qquad 1.42$$

where, M = Molecular weight

ρ = substance density

N_A = Avogadro's number

Rm is known as the Molar Refraction. If the Lorentz Field were an accurate reflection of the internal field then under conditions of changing number density, as with temperature or pressure, the molar refraction ought to be constant.

SECTION 2: BAND THEORY FOR SOLIDS

The simplest model for a solid is the free electron model which assumes that when atoms are brought together, the distribution of their inner core electrons is not significantly altered, whilst the valence electrons overlap appreciably. The free electron model gives an explanation of the electrical conductivity of solids in terms of the fermi sphere under an applied electric field. It also accounts for the small electronic contribution to the heat capacity, which is due to the fact that only electrons in states near to the fermi-energy are available to take up excitation energy. There are however numerous failures of this model. The band theory of solids takes over where the free electron model fails and many more features of electron behaviour are explained.

As atoms are brought together, their weakly bound valence electrons are considered as free, so that the solid is treated as an array of fixed positive ions immersed in a uniform sea of electrons. These ions produce a pattern of periodically varying electric fields, and as the electrons travel within the solid they experience the influence of this periodic potential V(r). The inability of the ions to scatter these electrons is analogous to the problem of X-ray diffraction in crystals, except we are now interested in the effect of electron waves. For a perfectly periodic lattice the waves are not scattered by the lattice, except when the wave vector K satisfies the Bragg condition. Bragg

reflection of electron waves in crystals is the cause of the energy gaps, which determine whether a solid is an insulator or a conductor.

If we consider the model of an electron in a periodic potential V(r), where the periodicity is that of the lattice, then the Schrodinger equation becomes:-

$$-\frac{\hbar^2}{2m}\frac{d^2\psi}{dr^2} + V(r)\psi = E\psi \qquad 1.43$$

To solve this equation even using approximate methods is difficult, but the most important difference is that the relationship between E and K is no longer a simple parabolic function. Instead the function is multivalued, and there are certain bands of energy which are forbidden ie. no permitted K states exist for them.

The relationship between E and K for 1 dimension of K is shown in Figure 1.03 (a).

All the curves repeat themselves after an interval in K of $2\pi/a$. For each wave vector, there are several permitted energies, one within each energy band eg. B, B', B". In order to avoid confusion it is conventional to use certain sections of the curves chosen so that as K increases so does the energy. This is shown in Figure 1.03 (b) and is called the extended zone scheme. The reduced zone scheme shown in Figure 1.03 (c) uses the same range of K from $-\pi/a$ to π/a to cover all energy bands.

The number of permitted values of K in each zone is equal to the number of ions in the cyrstal, Ni. Associated with each K state is either of the two electron spin states, therefore the total number of states in each zone is 2Ni. If a metal has only one conduction electron per atom, then they will occupy all the states in the lower half of the zone, Figure 1.04 (a). For such monovalent metals, the energy distribution is virtually the same as predicted by the free electron model. If there are an even number of electrons per atom, then they would occupy an integral number of zones, Figure 1.04 (b). An applied electric field will not drive a current through the crystal unless the zones are so close together that electrons at the top of the uppermost filled zone can obtain enough extra energy to jump the forbidden energy gap. Since the energy gap can be a few eV, excitation to the next band cannot occur and so no current can flow. These materials would therefore be insulators. If the energy gap is 1eV or less, a few electrons can be excited across the energy gap at room temperature. The amount of excitation will increase with temperature, therefore the conductivity increases as the temperature is raised. This behaviour is typical of a semiconductor whilst in metals the increased electron scattering due to lattice vibrations cause the electronic conductivity to decrease with increasing temperature.

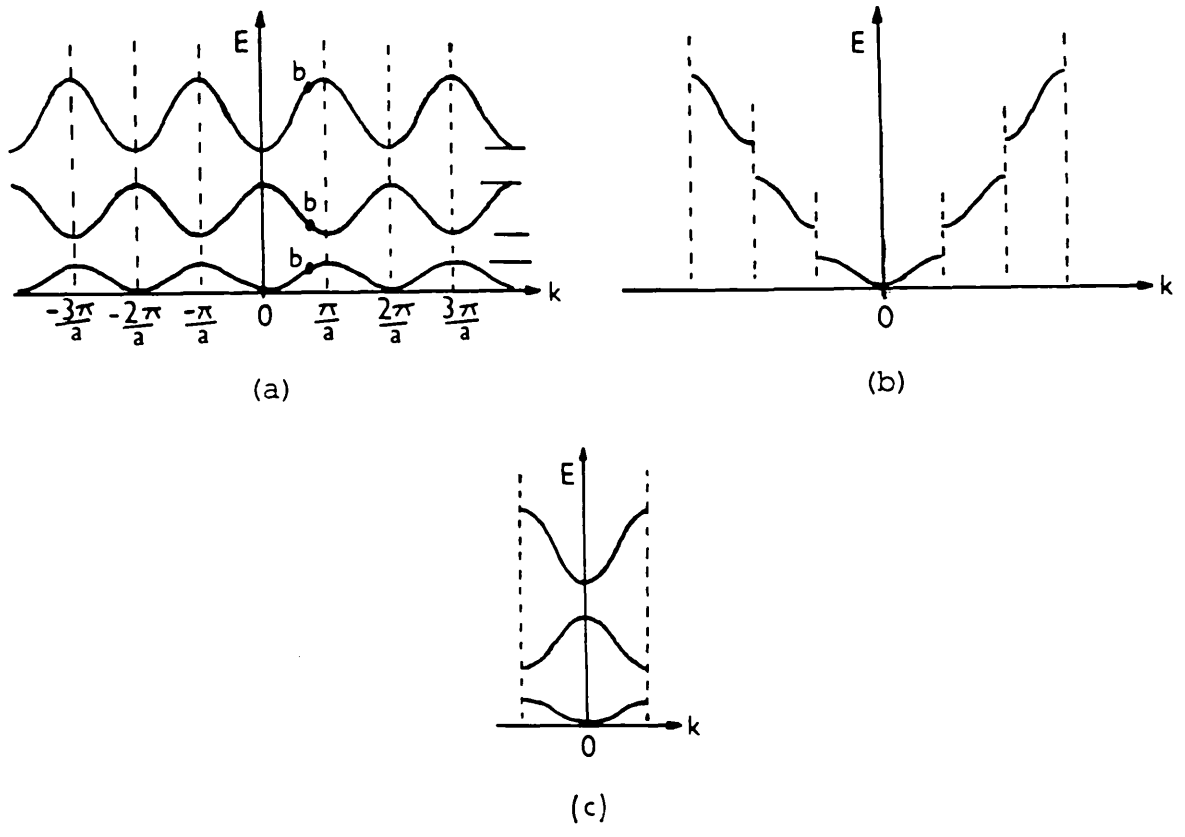


Figure 1.03: Energy curves for the simple band theory in one dimension. All the curves may be translated into the extended zone scheme, (b) and the reduced zone scheme, (c).

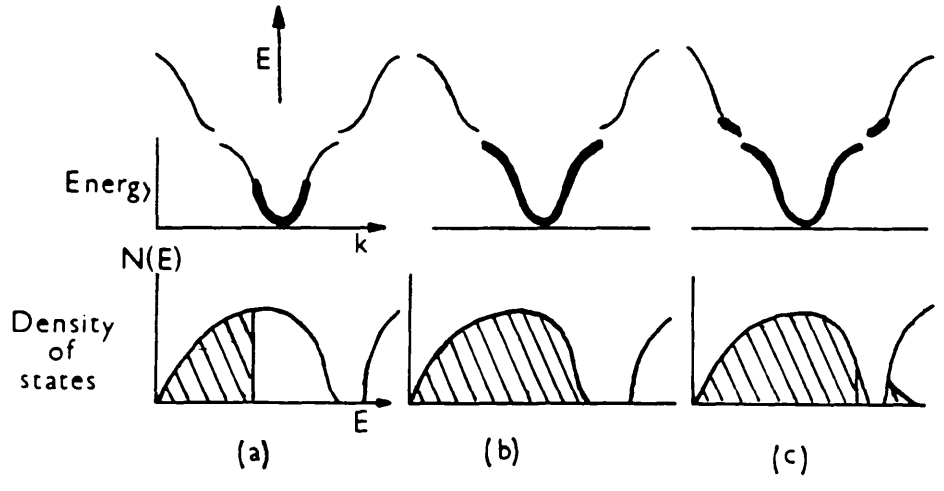


Figure 1.04: Energy curves and density of states curves for (a) a conductor, (b) an insulator, (c) a semiconductor.

One way of exciting electrons from the valence band into the conduction band is with a quantum of light. A photon of frequency ω has an energy of $\hbar\omega$ and two sorts of transitions can occur.

In Figure 1.05 (a) the conduction band edge occurs at the same wave-vector as the valence band edge and the threshold of absorption occurs when a direct transition is made at a threshold energy of $\hbar\omega_g = E_g$, the energy gap. Conservation of momentum requires that the electron must take up the photon's momentum and move along the K axis; however, due to the large value of the velocity of light, the photon wave-vector is small enough to be ignored and a vertical transition is assumed. In Figure 1.05 (b) the minima of the conduction band do not occur at the same wave-vector value as the valence band edge; the threshold for absorption is obtained due to an interaction which produces a phonon of wave-vector large enough to give the electron the opposite momentum, taking it to a minimum in the conduction band. Since even a large wave-vector phonon does not have much energy, the onset of indirect optical transition at $E_g + \hbar\Omega$ is below that of vertical transitions. At higher temperatures with phonons already present, a valence band electron may absorb a phonon together with a photon to make initial indirect transitions at the lower photon energy of $E_g - \hbar\Omega$. The magnitude of the band gap can therefore be deduced by optical experiments at low temperature, a sharp absorption threshold will generally denote a direct transition.

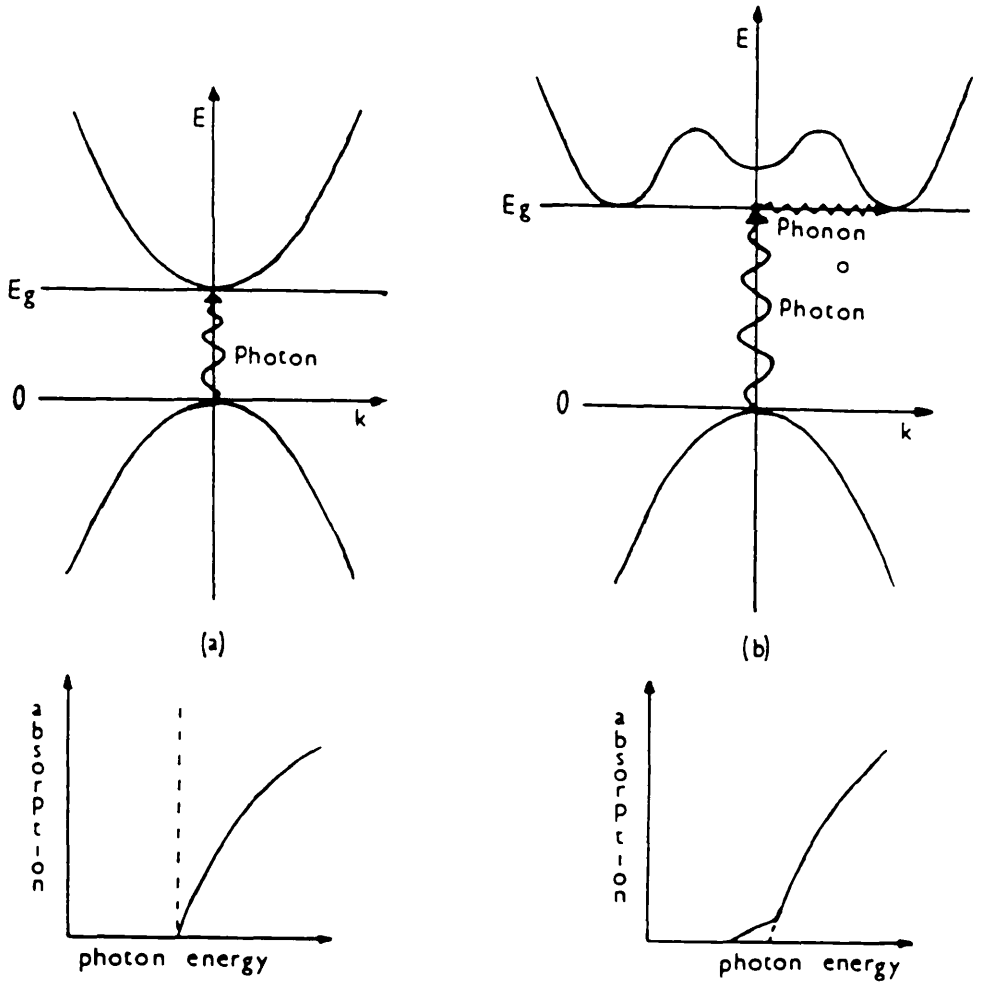


Figure 1.05: Excitation of valence electrons (a) Direct transition (b) Indirect transition.

Electrons can be thermally excited into the conduction band, the concentration at temperature T being largely controlled by the parameter E_g / K_BT for intrinsic semiconductors. Even at room temperature, there is a sizeable proportion of electrons in the conduction band; they and the holes that are created upon excitation are called carriers and both contribute to the conductivity. The band gap may be determined from temperature dependence of the conductivity or the carrier concentration, as measured by the Hall Effect.

The optical properties of insulators often show some fine structure just below the absorption edge. This is due to electron excitation into bound states that lie within the gap, just under the conduction band, called excitons. Excitons are created when, although not enough energy is input to excite an electron across the gap, an electron can still be excited to leave a hole with which it then forms a "hydrogen like" bound state. Although electrically neutral, this state can transport excitation energy through the crystal.

At first sight, it would appear that experiments determining the absorption characteristics of materials, would not be of too much value in trying to deduce anything in detail about the E - K curve or the density of states This is because absorption curves represent a sum of all possible transitions that can occur for a particular photon energy. However, much information can be retrieved by using modulation spectroscopy, which utilises important relations

concerning the derivatives of the reflectance with respect to wavelength, temperature, pressure etc. Band gap information, from optical experiments, enable better parameters to be fitted into theoretical models, thus producing a better and more complete picture.

CHAPTER TWO

EXPERIMENTAL DETAILS

Experimental Measurement of n and k

The measurement of refractive index, n, and extinction coefficient, k, for a medium is complicated by the experimentally measurable properties being functions of both parameters. For an absorbing medium where k is low enough to allow some measurable transmission we can study the refraction at the boundary of the absorber. Snell's law involves the complex refractive index, however by measuring the real angle between the normal to the boundary and the refracted ray it can be shown (Moss, 1959) that for $k^2 << n^2$:-

$$\text{Sin } \phi = n \left[1 + \frac{k^2}{2n^4} \right] \text{Sin } \Psi \qquad 2.01$$

where ϕ is the angle of incidence.

Experimentally, we can only measure the light refracted at the rear surface of a prism if sufficient light is transmitted through the sample ie. for values of $k < 10^{-3}$. Therefore the error in n from measuring the index as for a non absorbing material is $k^2/2n^4$,this is of the order 10^{-7} and is quite acceptable.

The measurement of the extinction coefficient, k can be made in a separate experiment by measuring the light intensity transmitted through a thin sample layer.

The Refractometer

The measurement of refractive index as a function of wavelength, would prove very tedious if done manually for varying sample temperatures. A computer automated refractometer, which measures the refractive index of a prism shaped sample, was designed and constructed (Figure 2.01) by A. Donaldson (1983) and is now briefly described.

A stabilized quartz halogen light source is focused onto the entrance slit of a blazed grating monochromator. Light emerging from the monochromator is chopped, to enable phase sensitive detection, filtered and collimated. The front face of a prism shaped sample is aligned normally to the collimated monochromatic beam so that the index may be calculated from the single refraction at the rear sample surface. The refracted beam is detected by a focusing lens and a germanium photodiode, which are mounted on a rotating arm. The arm is fixed to a motorised rotary table that allows the detector to be stepped through the beam profile.

The parallel user port of a C.B.M. microcomputer is interfaced with three stepping motors to control the detector arm, the filter wheel and the monochromator output wavelength. The port is also used to operate reed switches

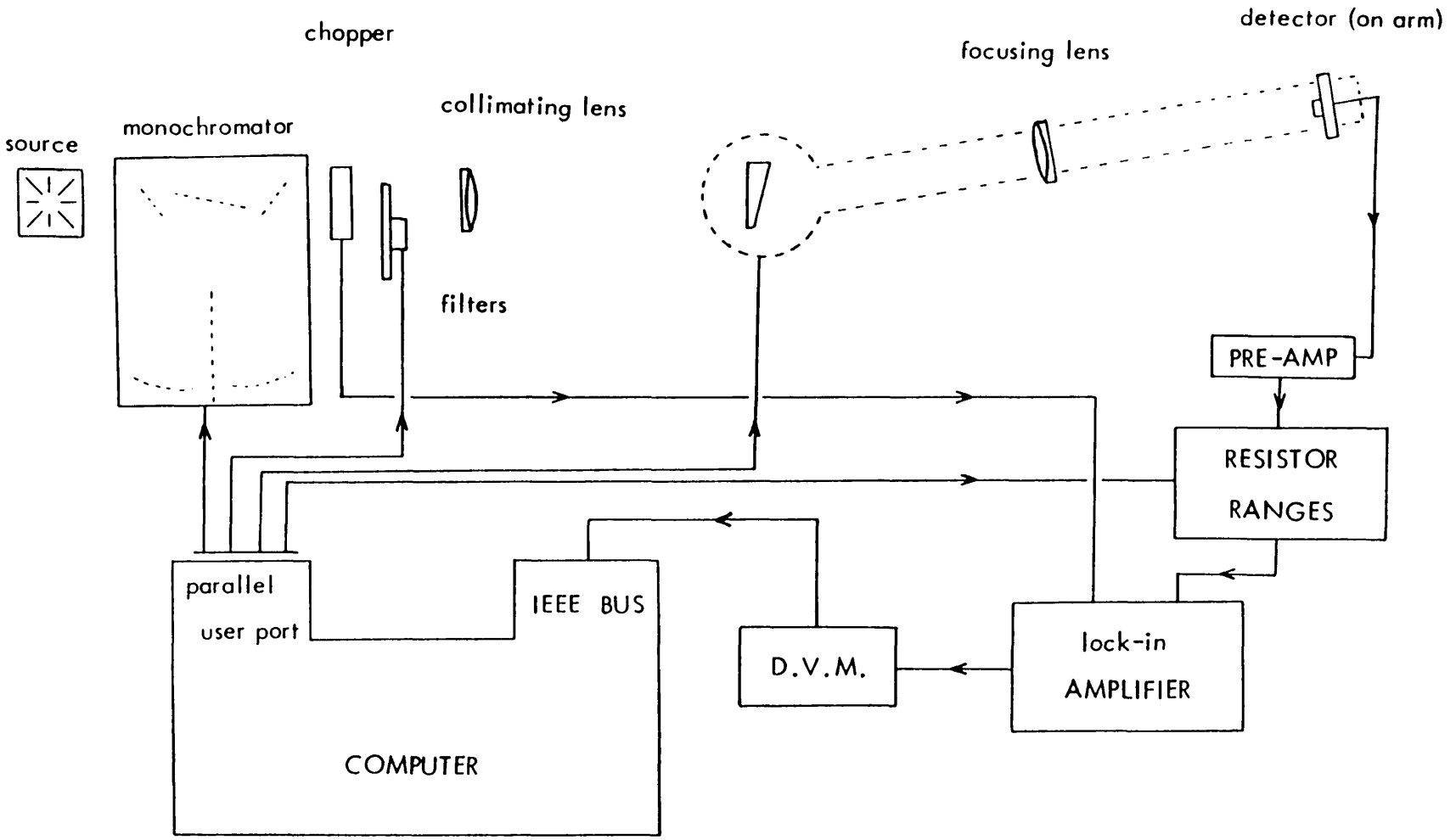


Figure 2.01: Schematic diagram of the refractometer.

in the "resistor range box" which is a four resistored ladder enabling the sensitivity of the detecting system to be adjusted automatically. The detected signal is correlated with the chopping frequency, amplified and displayed on a Digital Voltmeter. This D.V.M. also performs the analogue to digital conversion needed for input to the computer. The operating program is written in BASIC with machine code routines to speed up the frequent moving of the stepping motors.

Operation Program Index

The index measuring program consists of a main program sequence, which accesses numerous subroutines to perform each of the many mechanical and analytical actions. A schematic flow diagram of the program is shown in Figure 2.02 and a brief explanation now follows:-

Initialisation: In setting up the program the starting wavelength, wavelength increment, prism angle, present detector step position and any required time delay are input from the keyboard. The floppy discs used for data recording are initialised and two machine language routines are loaded into the computer memory. These two routines are used to speed up the frequent stepping of the monochromator and the detector arm.

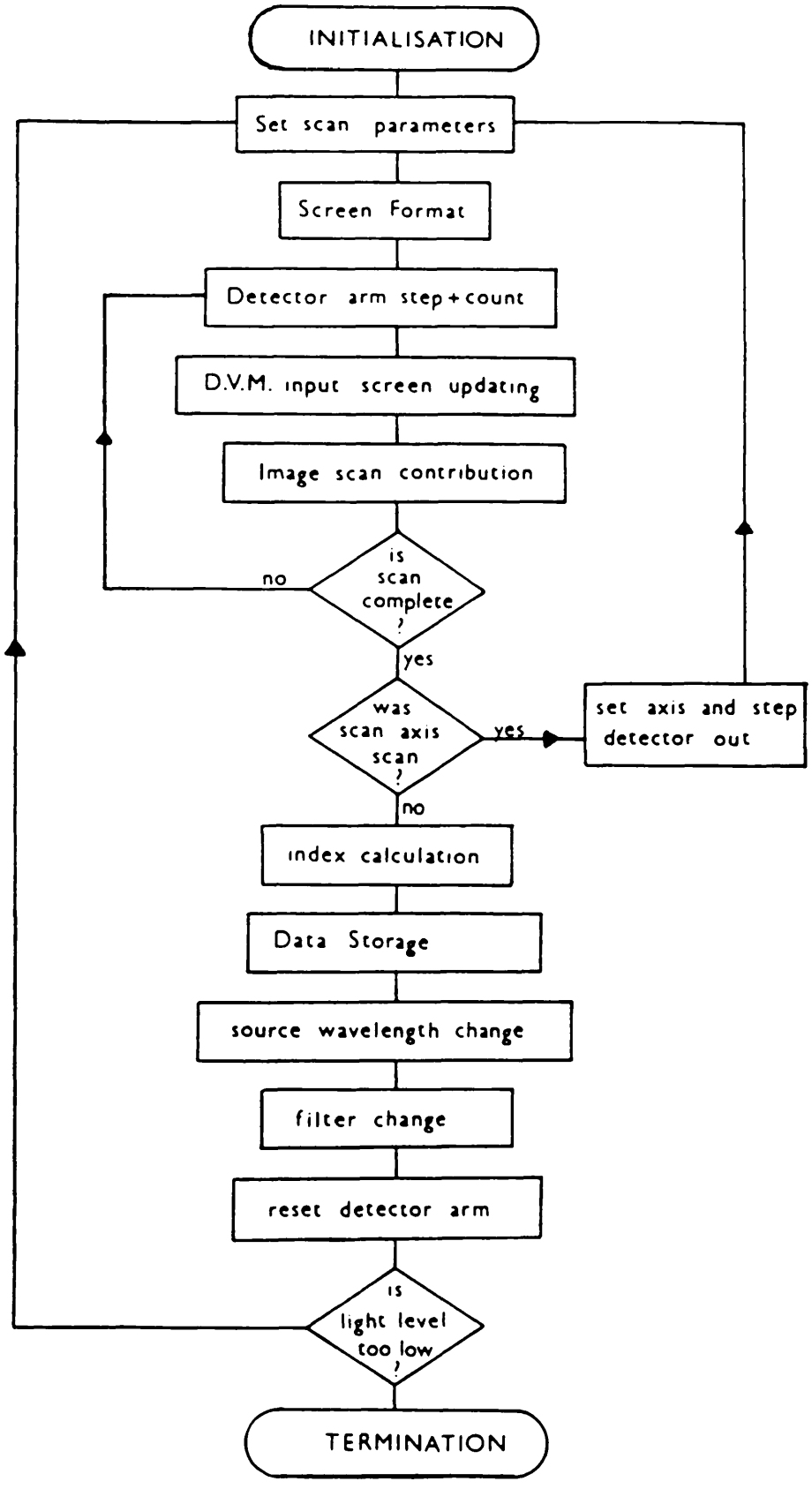


Figure 2.02: Index measuring program.

Set Scan Parameters: The threshold value and other scan parameters pertain to an individual scan of the image intensity profile and are therefore reset for each index measurement.

Screen Formatting: This clears and re-formats the screen's information display for each scan.

Detector Arm Step and Count: This uses the machine code routine to step the detector arm away from the axis and then increments the step number variable.

DVM Input and Screen Updating: The detected intensity is read into the computer from the IEEE interfaced DVM. To exclude the possibility of recording voltage spikes, two readings are compared with an acceptable noise level.

Image Scan Contribution: For detected intensities greater than the threshold value the image intensity profile is mapped out. When the signal falls back below the threshold the scan is complete, and the centroid is calculated. If this scan was a measurement of the axis position prior to the melting of the sample, then the program sets the axis position and moves the detector out to the region of the refracted beam. Otherwise the program proceeds with a calculation of the index.

Index Calculation: From the recorded axis and the measured refracted beam position the sample's index is calculated.

Data Storage: Each index result is stored on the end of a floppy disc sequential data file. During initialisation this data file has the starting wavelength and the wavelength step recorded as its first two values, and the file is terminated by writing the value -1 onto the end.

Source Wavelength Change: The 2nd machine language routine is used to step the monochromator grating to give the next wavelength.

Filter Change: A check is made to see if the right filter is inserted for the new monochromator wavelength. When required a new filter is stepped into the beam.

Reset Detector Arm: As the detector is stepped back through the beam profile, a quick study is made at this new wavelength. This enables any required adjustment of the sensitivity to be made using the computer controlled resistor ranges, and a new threshold value is then set. As the reset routine takes the detected signal below this new threshold the computer exits to the next scan.

Check Light Level: If the light level becomes too low, the experiment is terminated and the detector arm returned to a specific reference point.

OPTICAL CELL

The components of the optical cell have essentially remained unchanged and a detailed description of their preparation is again given by A. Donaldson (1983).

A sealed prism shaped cell with optical windows is formed by sandwiching two polished pyrex discs around a hollowed wedge, (Figure 2.03a), using thin Grafoil washers to form the seal. Cavities bored into each disc (Figure 2.03b) provide internal reservoirs for the solid sample, which is either crushed or melted into them, so that on heating the sample will melt and run down into the hollow prism (Figure 2.03c). A second prism is used to "square up" the cell and allow compression within the cylindrical heating block (Figure 2.03d). This second prism also has a hole bored in it through which the collimated beam can illuminate the optical cell. Experimentally, it was found that annealing the two prisms after boring and grinding, helped to prevent them cracking when compressed.

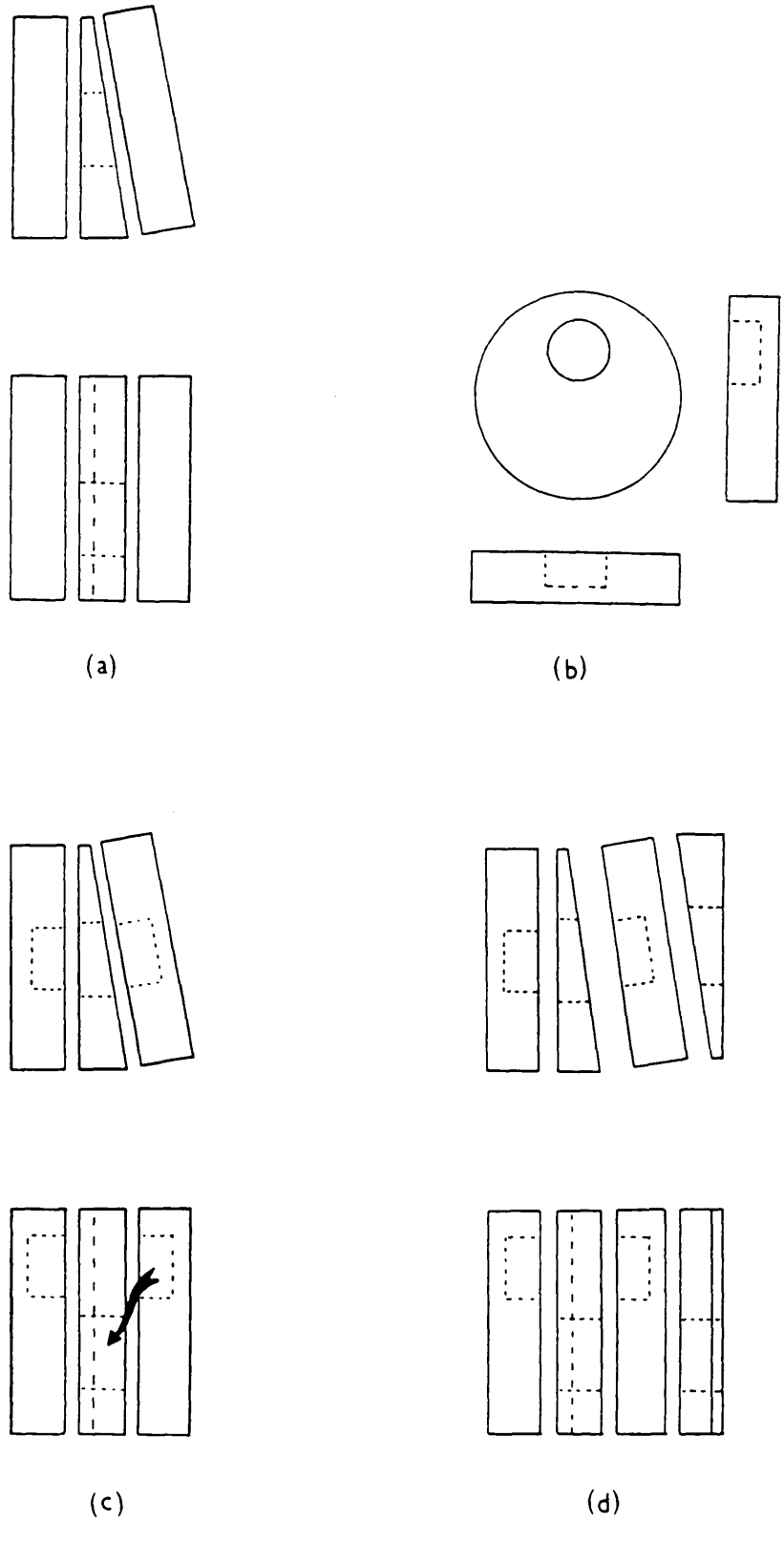


Figure 2.03: Optical cell components and assembly.

Heater Design

The original brass heating block, with four 50 watt resistors attached to it, had proved sufficient for measuring the properties of molten sulphur. However its maximum working temperature of 230 deg. C. was a fundamental limit to the range of sample being studied.

The initial heater design was a simple brass cylinder and piston, the cell's resistance coil was wound around the cylinder on asbestos paper and electrically insulated in alumina cement. Thermal insulation was provided by packing the strip form of Titron Kaowool Ceramic Fibre around the block.

At the higher temperatures reached by this block, high sample vapour pressure and differential expansion between the brass and the pyrex cell caused problems with slow sample leakage:-

(1) Often the loss would cause the sample level to fall below the light beam height and terminate the experiment.

(2) The lost sample would contaminate the electrical and thermal insulation.

(3) Escaping samples may oxidise giving off toxic fumes.

Several methods of sealing the Grafoil gaskets were tried unsuccessfully, and eventually a more sophisticated heating block was designed to overcome these problems.

Stainless steel was chosen for the block, as it has a lower coefficient of expansion and can be easily cleaned if contaminated. To maintain a good compression on the cell, Inconel high temperature spring washers are used on the tightening screws, and the piston incorporates an aluminium sleeve which expands within the stainless steel, compensating for most of the differential expansion (Figure 2.04).

The heating cable, supplied by ARi Industries Inc, consists of a nickel chrome iron wire and compacted magnesia insulation sealed in an Inconel sheath. The sheath enables the cable to be manipulated to the required diameter coil and is then simply secured with glass fibre tape. Leads for the heating coil are made from nickel wire and are insulated using a woven thermocouple sheath.

Thermal Insulation is provided by semicircular insulating shells which fit around the heating block. These are made from two layers of Kaowool ceramic fibre separated by aluminium foil and sandwiched between supporting stainless steel shells (Figure 2.05). Using a 200 watt power supply the block will heat to over 500 deg. C. in less than two hours (Figure 2.06). The required working temperature is adjusted using a thermostat and the cell temperature monitored by a digital thermometer.

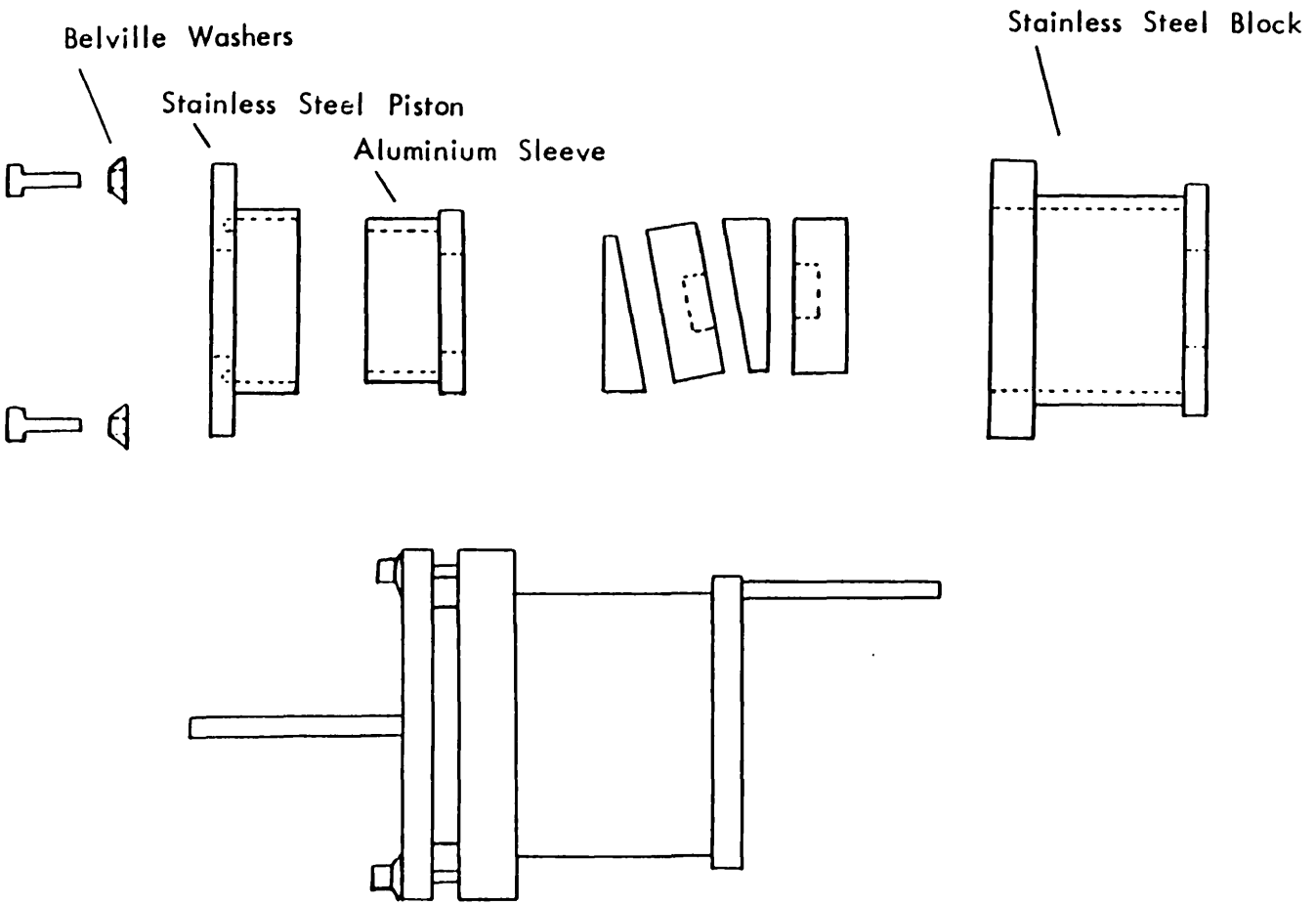


Figure 2.04: Heating block assembly.

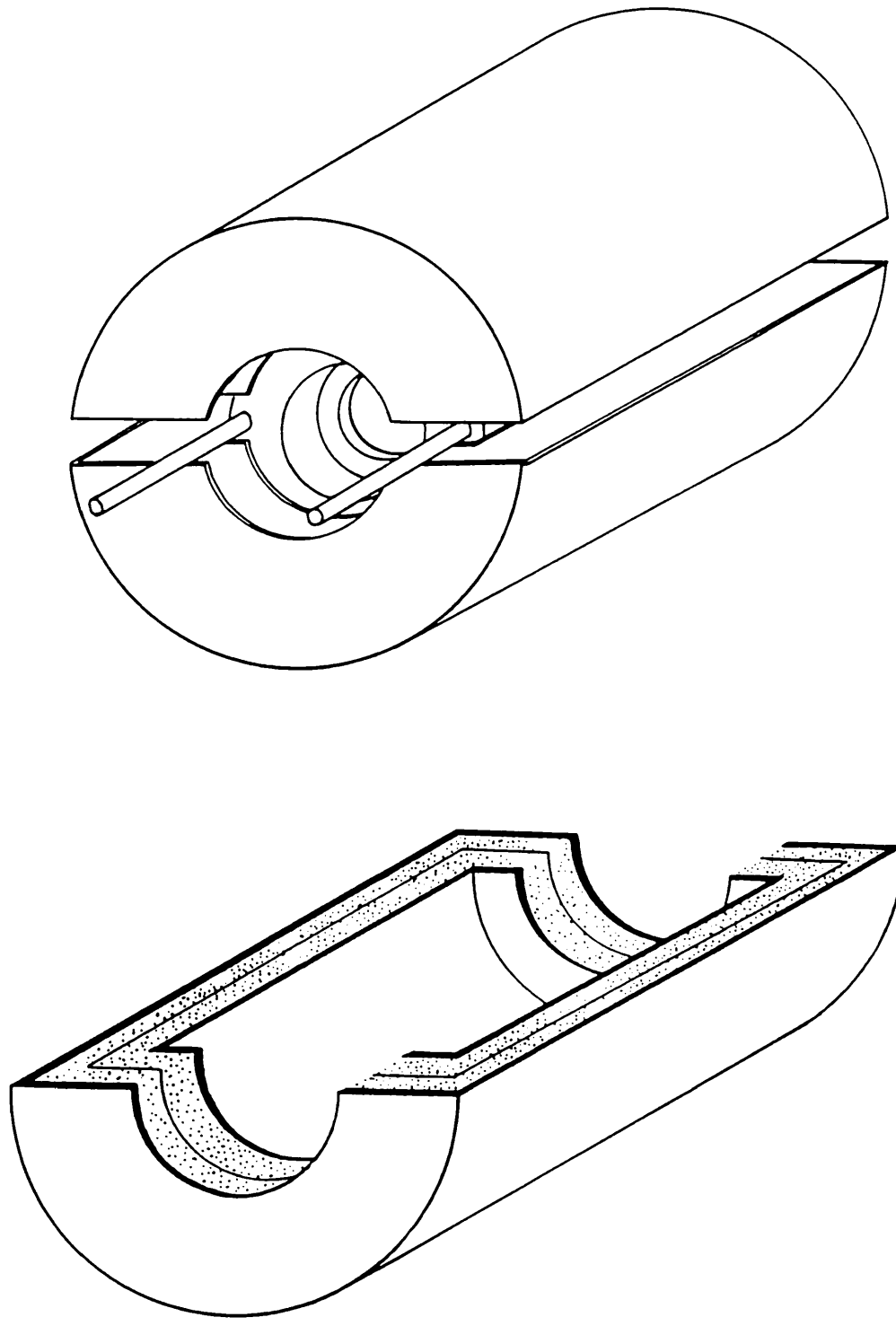


Figure 2.05: Thermal insulation.

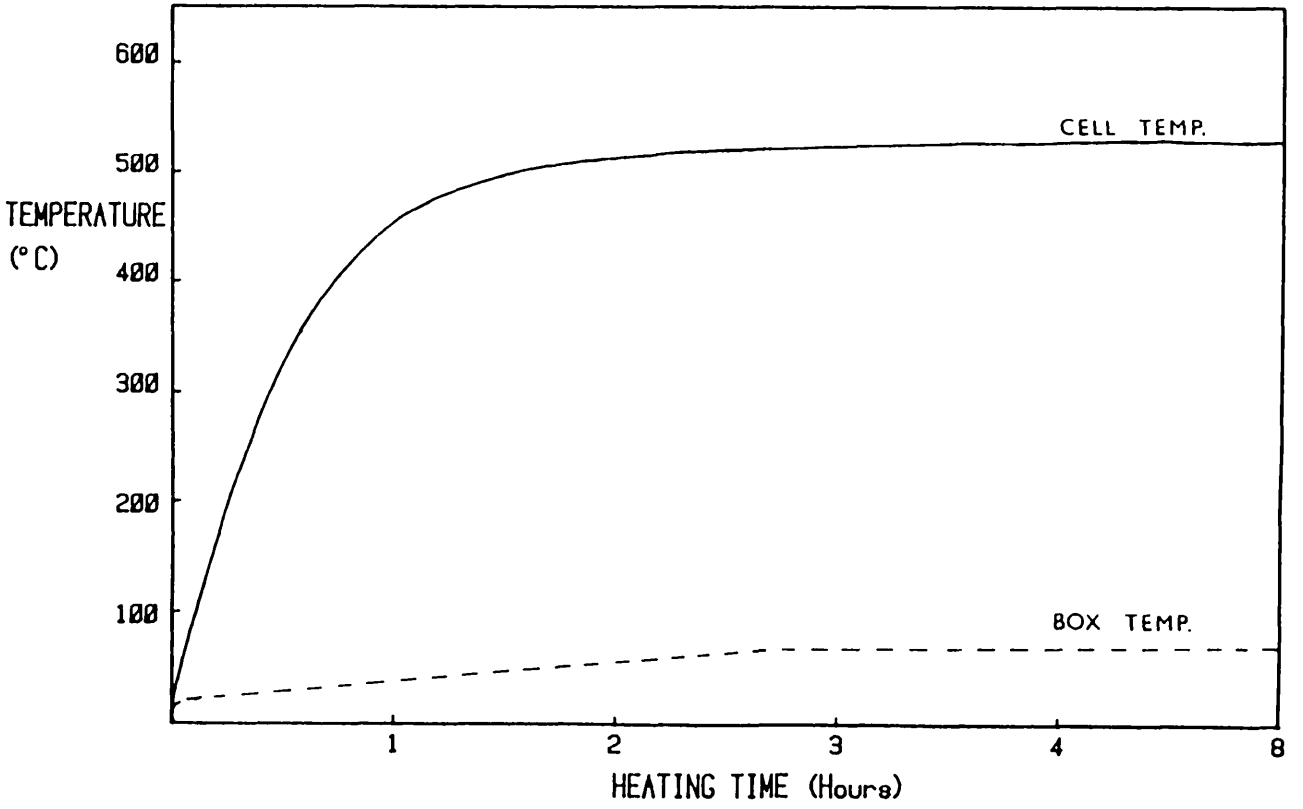


Figure 2.06: Maximum heating rate for cell and enclosing box.

Enclosing Box

Despite the improved heating block, precautions were still required to guard against sample leakages hence the need to enclose the cell in an hermetically sealed box.

An aluminium box with optical windows, to allow the light beam through, was made in which the cell, heating block and insulation could be mounted (Figure 2.07). Balzer's High Vacuum fittings were adapted to make electrical feed throughs for the heating coil power supply and the detecting thermocouples. To maintain an inert atmosphere within the box an OFN gas cylinder was used to supply a purging gas. An automatic flow control valve ensures a constant flow of gas, despite any fluctuations in the cylinder regulator pressure. The exhaust gases from the box are filtered to remove any toxic dust particles, and bubbled through water. The nitrogen flow system is fitted to the box via quick seal vacuum valves which, in the event of serious leakage, allow the box to be sealed, disconnected and removed to a fume cupboard. The box and its fittings are hermetically sealed using Viton O-rings. These O-rings have a maximum working temperature of 200 deg. C., and their suitability was checked by monitoring the box temperature whilst the cell was being heated continually at full power (Figure 2.05).

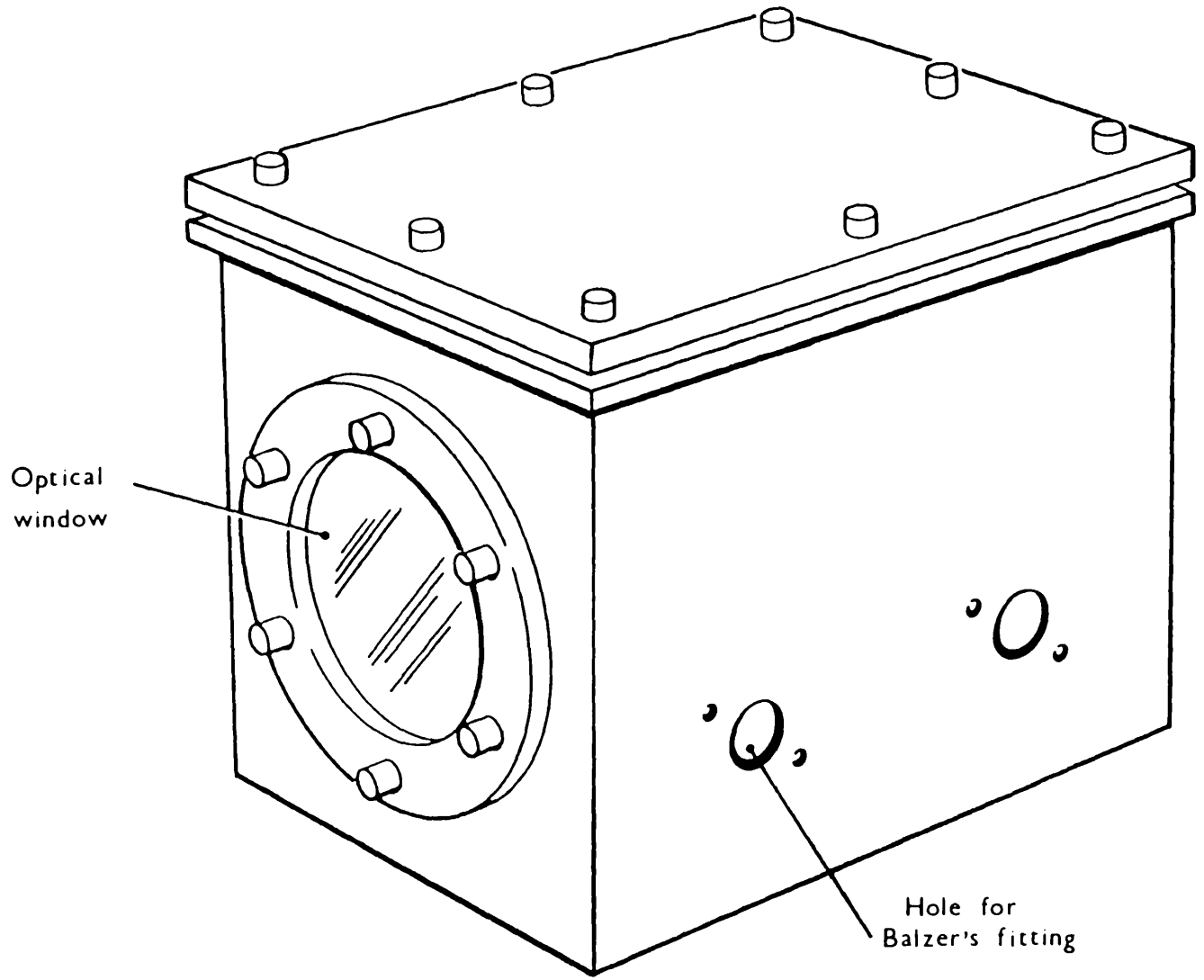


Figure 2.07: Enclosing box.

Adaption for Absorption

The stabilised power supply of the light source maintains a constant intensity which only varies by 1% over periods of several hours. This enables the optical absorption to be measured by the two stage experiment illustrated in Figure 2.08.

1st Stage: The rotary stage and detector arm are dispensed with and a lens is positioned to focus all the image intensity onto a large area silicon photodiode. The lamp intensity at each wavelength, with no cell present, is then measured.

2nd Stage: A thin sample layer is aligned in the beam and the transmitted intensity, at each wavelength, is measured.

A thin sample layer is formed by sandwiching a single grafoil ring between two optical flats. Only one sample cavity is required and on melting the sample runs down to fill the cell. This cell and an aluminium spacer ring are loaded into the heating block and mounted in the enclosing box.

The computer program, which performs both stages of the experiment, averages five intensities read from the D.V.M. and records this value on magnetic disc. The wavelength is then changed and the next measurement taken. Knowing the thickness of each glass component and the absorption

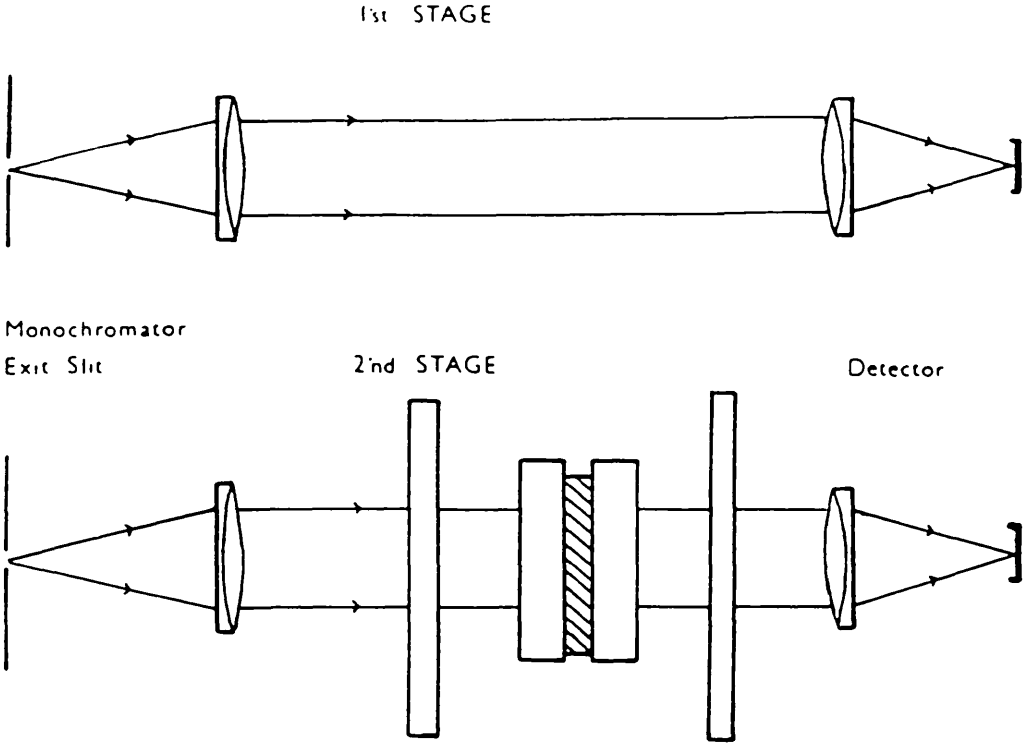


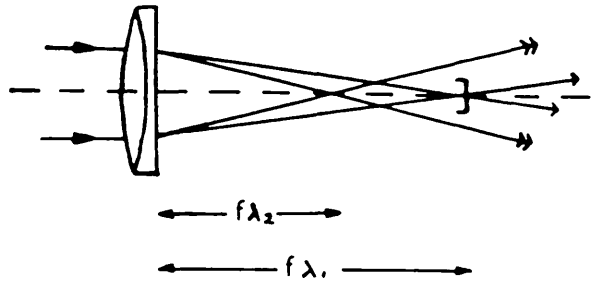
Figure 2.08: Two stage measurement of optical absorption.

coefficients of pyrex, corrections can be made for the reflections and absorption of each cell component, thus enabling the absorption coefficients of the sample to be calculated.

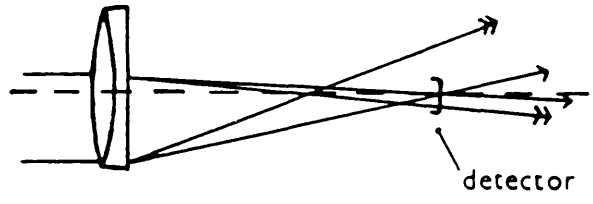
Experimental Errors in Index Calculation

Wavelength Dependence: The only detectable wavelength dependent property of the system should be the angle of deviation of the incident beam. The optical axis can be aligned quite accurately by laser reflections off the lens surfaces so that even if the focal length of the acromat lens changes with wavelength (Figure 2.09a) the cone of light at the detector remains symmetrical. If the collimated beam is not centred on axis as shown in Figure 2.09b, the detector sees an asymmetrical cone of rays, which for a short focal length lens moves the intensity centroid above the optical axis. By using a long focal length lens the ray asymmetry will not affect the centroid position. The image shift is now insensitive to lateral displacement of the collimated beam, therefore the positioning of the prism along the optical axis is not crucial Figure 2.09c.

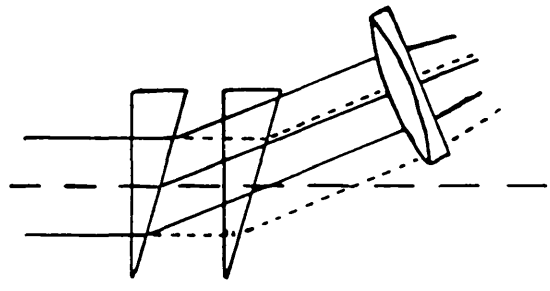
The wavelength dependence of the system was tested by measuring the position of the axis beam and the dispersion of a glass prism at different positions along the beam. The variation in the measured beam axis was less than two motor steps over the entire wavelength range, each step being an



(a)



(b)



(c)

Figure 2.09: Optical axis and effects of prism positioning.

angular change of the detector arm of 0.25 arc minutes. No significant change in the dispersion curves were detected even for prism positions ~15mm apart.

Measurement of Prism Angle: The refractive index of a sample is calculated from the single refraction at the rear surface of a prism, as shown below in Figure 2.10.

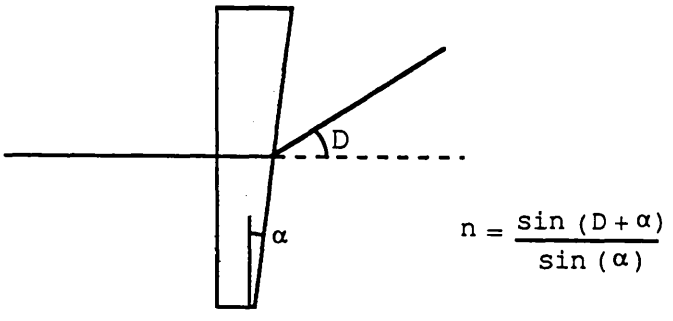


Figure 2.10 Single Refraction Calculation

Typically the prism angle is ~4 degrees and the error in the refractive index Δn, due to an error $\Delta\alpha$ in the measured cell angle, is illustrated in Figure 2.11. To measure the cell angle we mount the heating block on a spectrometer table, using a HeNe laser to align each surface in turn, we can work out the cell angle from the spectrometer's vernier calibration. With care the cell angle can be measured to ± 0.01 degrees enabling the index to be calculated with $\Delta n < 0.004$. Obviously any change in the cell angle as it is heated would directly affect the measured index; therefore, during an experiment, laser reflections are used to monitor the cell angle.

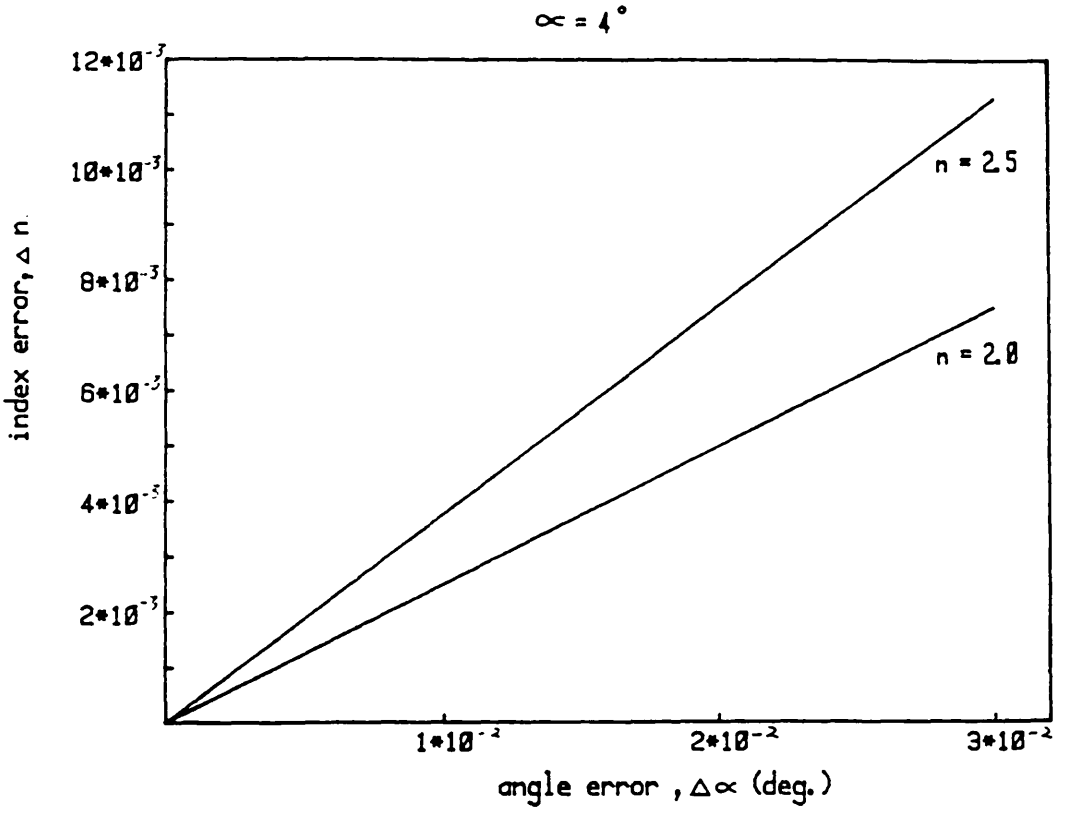


Figure 2.11: Error resulting from measured cell angle.

Cell Alignment: To calculate a samples index from a single refraction requires that the front prism surface be aligned perpendicular to the incident beam. An error e_1 in this alignment is illustrated in Figure 2.12.

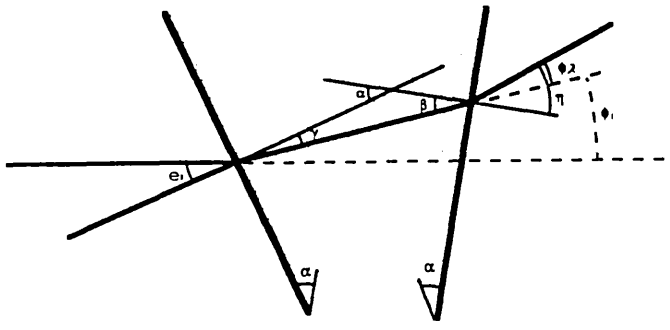


Figure 2.12 Error in Cell Alignment, e_1

$$B = \alpha - \gamma : \theta_1 = e_1 - \gamma : \theta_2 = \eta - B \qquad 2.02$$

at respective boundaries:-

$$\text{Sin } e_1 = n \text{ Sin } \gamma : n \text{ Sin } B = \text{Sin } \eta \qquad 2.03$$

Total Deviation, $D = \theta_1 + \theta_2$ and substituting gives

$$D = \theta_1 + \theta_2 = e_1 - \gamma + \eta - B \qquad 2.04$$

$$D = e_1 + \eta - \alpha = e_1 + \text{Sin}^{-1}(n \text{ Sin } B) - \alpha \qquad 2.05$$

$$D = e_1 + \text{Sin}^{-1}(n \text{ Sin } (\alpha - \gamma)) - \alpha \qquad 2.06$$

$$D = e_1 + \text{Sin}^{-1}\{ n \text{ Sin } [\alpha - \text{Sin}^{-1}((\text{Sin } e_1)/n)]\} - \alpha \qquad 2.07$$

The difference between the index when e_1 is taken into account and that due to using the simple one refraction formula is shown in Figure 2.13.

Two other errors can arise due to the misalignment of the cell. A tilt of the prism from its vertical plane increases the effective prism angle whilst any rotation of the prism will reduce the angle. With reasonable alignment of the cell A. Donaldson (1983) has shown that these errors can be safely ignored.

Errors and Corrections in Absorption Experiments

In order to measure high absorption coefficients our experiment only uses small sample thicknesses. To obtain accurate values from the initial and absorbed intensities, corrections must be made for the losses due to reflections from and absorption within the glass windows. We can approximate the series of reflection and transmission terms at each boundary to just one reflection and transmission, with absorption in between. This situation is shown in Figure 2.14; allowing the calculation of the sample's absorption coefficient from the experimentally measured transmittance, T.

$$\alpha_s = \frac{1}{Z} \ln \frac{T_1^2 T_2^2 e^{-2\alpha_g \omega}}{T} \qquad 2.08$$

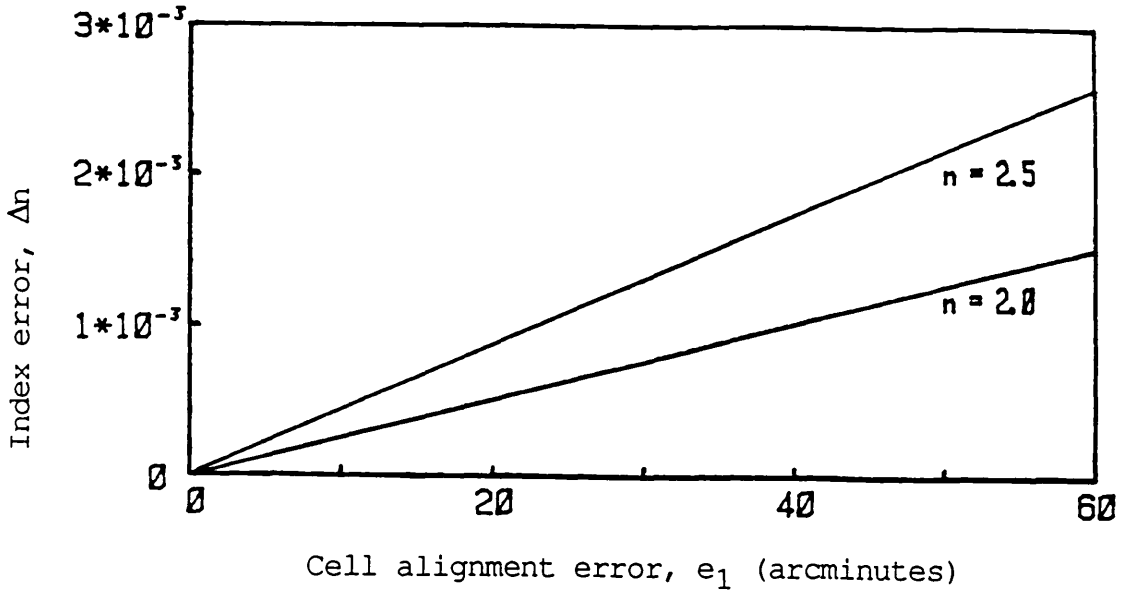
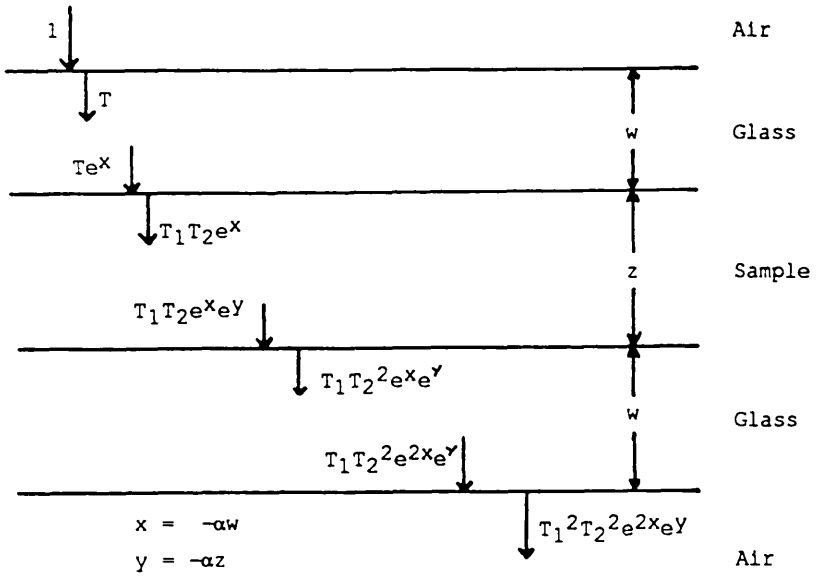


Figure 2.13: Index error resulting from e_1.



$$T_1 = \frac{4n_g}{(n_g + 1)} \qquad T_2 = \frac{4n_g n_s}{(n_g + n_s)}$$

Figure 2.14: Approximation for absorption cell transmission.

The error incurred by using this approximation, as opposed to an exact calculation, is illustrated in Figure 2.15. The dependance on α_g is due to the importance of successive reflections within the glass.

So far we have neglected the optical windows of the enclosing box through which the incident and transmitted beams must travel, however further corrections for reflection and absorption at these windows can easily be made using the same approximations.

Measurement of Sample Thickness: The optical absorption coefficient is defined by $\alpha = -1/Z \ln\{I/I_0\}$, where I and I_0 are the transmitted and incident intensities, respectively. To calculate α from these measured intensities we need to know the sample thickness, Z. Figure 2.16 shows the resultant error due to an error in the measured sample thickness, and illustrates that for high absorption coefficients an accurate measurement of Z is essential.

Before loading the cell, the thickness of the two pyrex flats is measured using a micrometer. The cell can then be assembled and tightened within the heating block. To measure the final cell thickness two micrometers were fixed to a purpose made G clamp as shown in Figure 2.17. The resulting error in the sample thickness is $\sim \pm 0.005$ cm; this value is illustrated in Figure 2.16 and can be used to estimate the resulting experimental error as a function of absorption coefficient, Figure 2.18. For absorption coefficients less than 10 cm^{-1}, the correction and sample thickness errors are

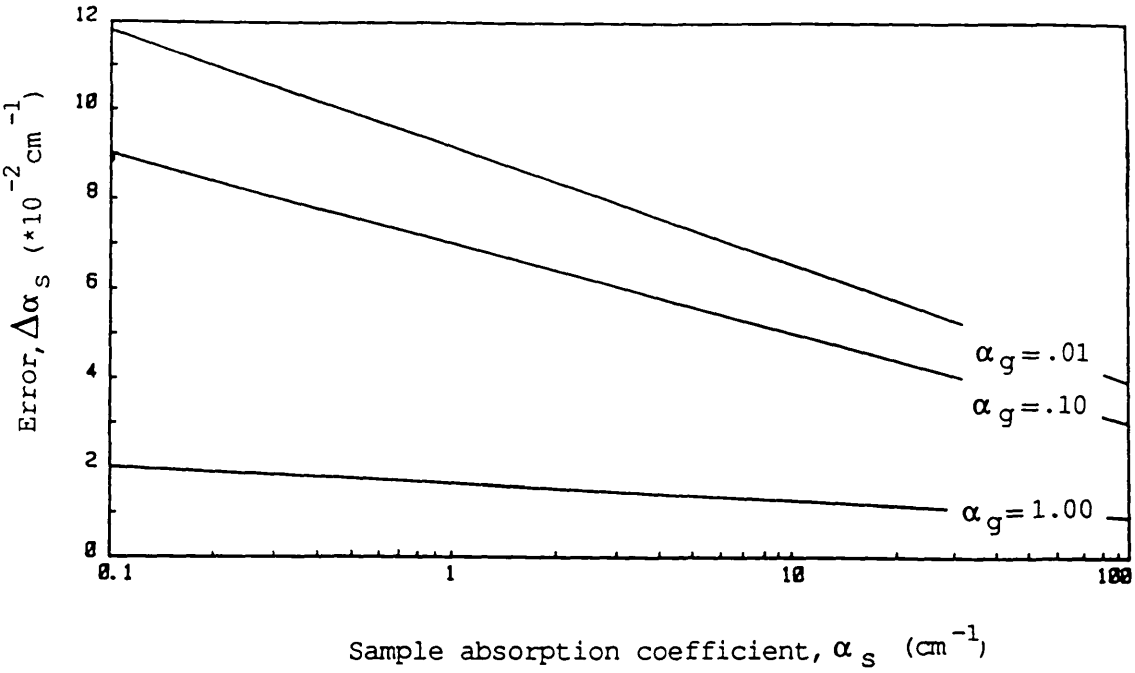


Figure 2.15: Error due to absorption approximation.

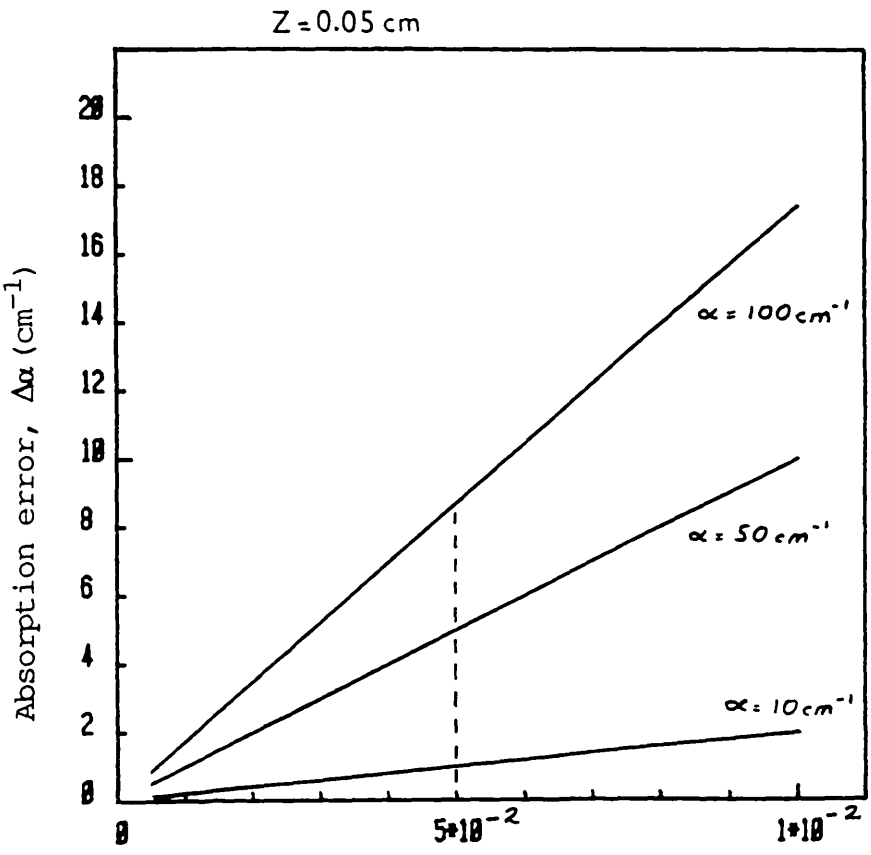


Figure 2.16: Error in the measured sample thickness.

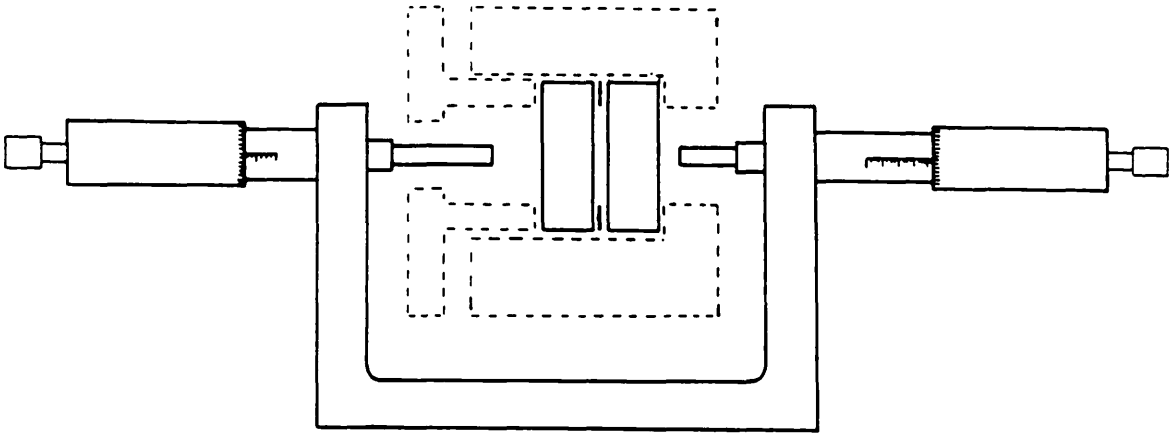


Figure 2.17: Cell thickness gauge.

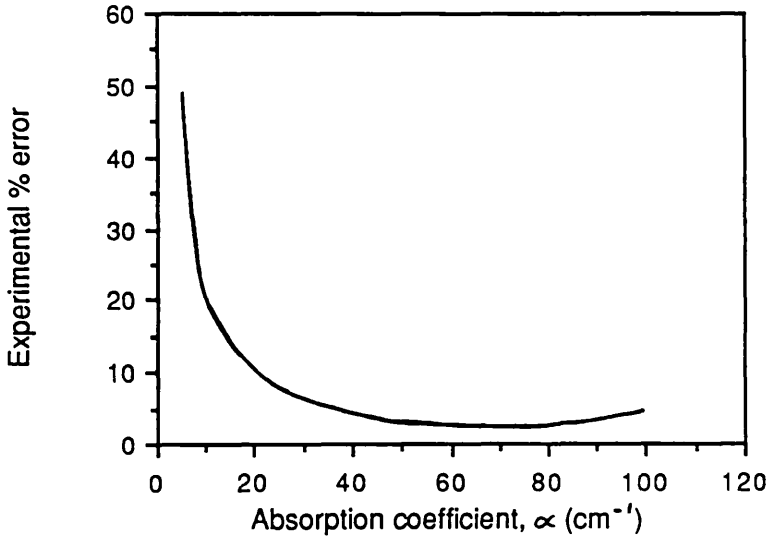


Figure 2.18: Error in absorption coefficients.

both small. These low absorption results are, however, dominated by noise fluctuations in the lamp intensity, giving a resultant estimated accuracy of $\pm 3cm^{-1}$.

CHAPTER THREE

OPTICAL PROPERTIES OF PHOSPHORUS SESQUISULPHIDE

PHOSPHORUS SESQUISULPHIDE, P_4S_3

(also called Phosphorus Tetritatrisulphide or Tetraphosphorus Trisulphide)

Phosphorus Sesquisulphide is made up of a strained basal ring of three phosphorus atoms, with each of these atoms bonded through a separate sulphur atom to a fourth phosphorus atom. These molecules form pale yellow brick-shaped crystals which melt at 173 deg. C., and boil at 407 deg. C. P_4S_3 is not spontaneously flammable, however with an auto-ignition temperature of 100 deg. C. it can be easily ignited in air by friction, static electrical discharge and heating. It is this ability to easily ignite by friction that has made P_4S_3 the essential ingredient of friction (strike anywhere) matches, replacing the use of white phosphorus which had always been a source of serious injury.

Because of its use in the manufacture of matches, P_4S_3 is made on a commercial scale. This is done by pouring molten phosphorus into a stirred cast iron container of molten sulphur. The rate of adding the phosphorus is controlled to maintain a reaction temperature in the range 320 - 380 deg. C. and the completed batch is then maintained at this temperature, by external heating, for several hours.

The molecular structure of P_4S_3 in the solid state was determined by X-ray diffraction (Y. C.Leung et al, 1955) and is shown in Figure 3.01. Electron diffraction studies on the gas phase (P. A.Akishen et al, 1960) are consistent with the same structure, as are the Nuclear Magnetic Resonance studies on P_4S_3 in Carbon Disulphide solution (R.A.Dwek et al, 1969). Vibrational spectroscopy is the only technique for structure investigation which is readily applicable to solids, solutions, liquids and gases, and the Raman spectra conclusively shows that P_4S_3 retains its cage structure in the liquid and gaseous states (M.Gardner, 1973).

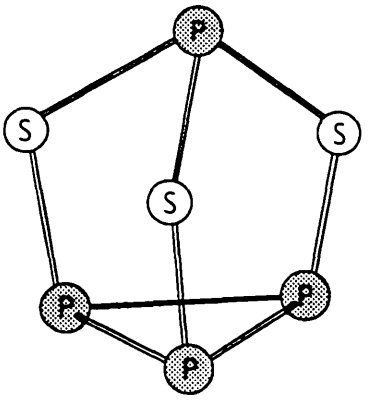


Figure 3.01 Structure of P_4S_3

The crystal structure of P_4S_3 was also determined by Leung (1955) and is illustrated in Figure 3.02. There are eight molecules in the unit cell which are packed approximately in a hexagonal close-packed arrangement. At 41 deg. C.. P_4S_3 undergoes a crystalline to plastic phase transition (Chattopadhyay (1983)) which is due to orientational disordering of the molecules whilst still

occupying the lattice sites. Weak intermolecular Van der Waals' interactions allow rotational freedom of the molecules, while the small molecular dipole moment stabilises the structure.

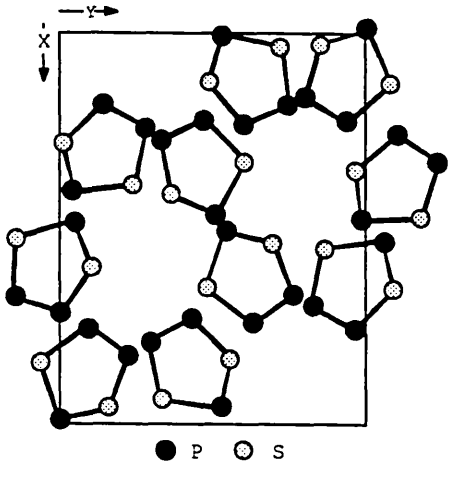


Figure 3.02 Projection of the Structure of P_4S_3 Crystal Along the 100 Direction

The high resolution nuclear magnetic resonance, n.m.r, spectra of solids are usually dominated by nuclear interaction and chemical shift anisotropy, which obscure the available structural information. These interactions are effectively removed from the spectra of fluids by rapid molecular reorientation and diffusion. The large entropy of the first order phase transition at 41 deg. C. indicates substantial motion of the molecules in the solid, and it is believed that this was the first spectrum of its kind to be resolved in a solid, without the aid of artificial line narrowing techniques. In the low temperature form the

phosphorus n.m.r. spectrum is found to be bell shaped and structureless at all temperatures. Above the phase transition the spectrum is strongly narrowed by the rotational freedom of the molecules, and two lines with relative intensities 3:1 can be resolved. With increasing temperature the lines are gradually narrowed until at 150 deg. C., still well below the melting point, the two lines can be resolved into a doublet and a quartet as shown in Figure 3.03 (C. F. Callis et al, 1957). The doublet is assigned to the three phosphorus atoms in the basal plane, whilst the weaker quartet with relative intensities 1:3:3:1 corresponds to the apex phosphorus atom.

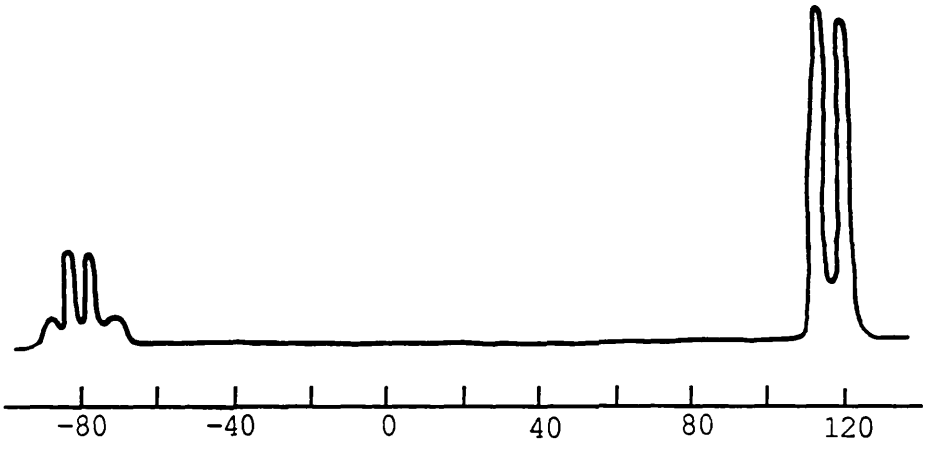


Figure 3.03: ^{31}P NMR Srectrum in solid P_4S_3 at 150 deg.C. (Shift from peak for 85% H_3PO_4, measured in p.p.m. of magnetic field).

The molecule has four types of average bond angle

S - P - S	99.4 deg	P - S - P	103 deg
S - P - P	103.1 deg	P - P - P	60 deg

The small bond angles of the three membered basal ring has caused much argument in the past, as to which bonding orbitals, the phosphorus atom uses. White phosphorus, P_4, is similar to P_4S_3, each atom being bonded to the others by three 60 deg P - P - P bond angles. To explain the 60 deg bond angle Arnold, (1946) suggested that the phosphorus atom uses pd^2 bond orbitals, since these orbitals exhibit a normal bond angle of 66 deg 26' and would require little strain to distort them to 60 deg.

Moffitt (1948) pointed out that the promotion of two 3p electrons to 3d orbitals is not plausible on energetic grounds. Also the P - P separations of both P and P S correspond to Sigma bond distances, where as the 3d radius of phosphorus would be larger. Moffit assumed the bonds to be formed using pure 3p orbitals and calculated the resulting strain energy; however as pointed out by Pauling (1952) this value did not compare well with the experimental strain energy. Pauling considered the use of spd hybrid bond orbitals and selected the hybridization parameters so as to minimise the energy of the molecule. These hybrid bond orbitals show good agreement with experiment and are largely p in character, the contributions of 3s and 3d orbitals amounting to 0.4% and 2.2% respectively.

Sample Preparation and Experimental Characteristics

A free sample of Phosphorus Sesquisulphide was supplied by Albright and Wilson Ltd. and was purified as follows:-

1. Boil in water for two hours to hydrolyse the sulphide impurities.
2. Dry sample.
3. Dissolve in Carbon Disulphide.
4. Filter solution.
5. Distil off Carbon Disulphide.

The presence of oxygen during recrystallisation forms small amounts of oxysulphides which intensify the yellow colour of the crystals. To eliminate these impurities the sample is left to recrystallise whilst in a glove box purged by dry nitrogen.

Molten phosphorus sesquisulphide, with its low auto-ignition temperature and high vapour pressure, presented many technical difficulties, however it was ideal for developing and testing the apparatus. The prepared sample was crushed into the cavities and, to prevent any oxidation, assembly of the optical cell was again done in the nitrogen glove box. The Enclosing Box, described in Chapter 2, ensures this nitrogen atmosphere is maintained throughout an experiment. Initial problems with sample leakage from the cell were successfully reduced by compensating for the

differential thermal expansion of the pyrex cell and its metal heating block; although some leakage through the grafoil gaskets was still experienced.

The results presented in this chapter are made up from three independently prepared samples, all of which were pale yellow crystals and melted to form a clear yellow liquid.

Measurements on Molten Phosphorus Sesquisulphide

The Refractive Index of molten samples of P_4S_3 was measured at varying temperatures, over the wavelength range 1.8 μm to 0.6 μm , using the apparatus and methods described in Chapter 2. The temperature range of 180 deg. C. to 380 deg. C. being limited by the sample's melting and boiling points. The wavelength dependence of the refractive index is shown in Figure 3.04 for seven sample temperatures, the subscripts A, B and C indicating the three independent sample batches. Figure 3.05 illustrates that at any given wavelength the index decreases with increasing temperature, this is primarily due to the decreasing density and, with this, the diminution of local field effects.

The optical absorption coefficients of molten phosphorus sesquisulphide were measured using the two stage method described in Chapter 2. A thin sample layer ~ 0.5mm thick was formed using a single grafoil gasket ring between two optical pyrex flats. This sample thickness limits the

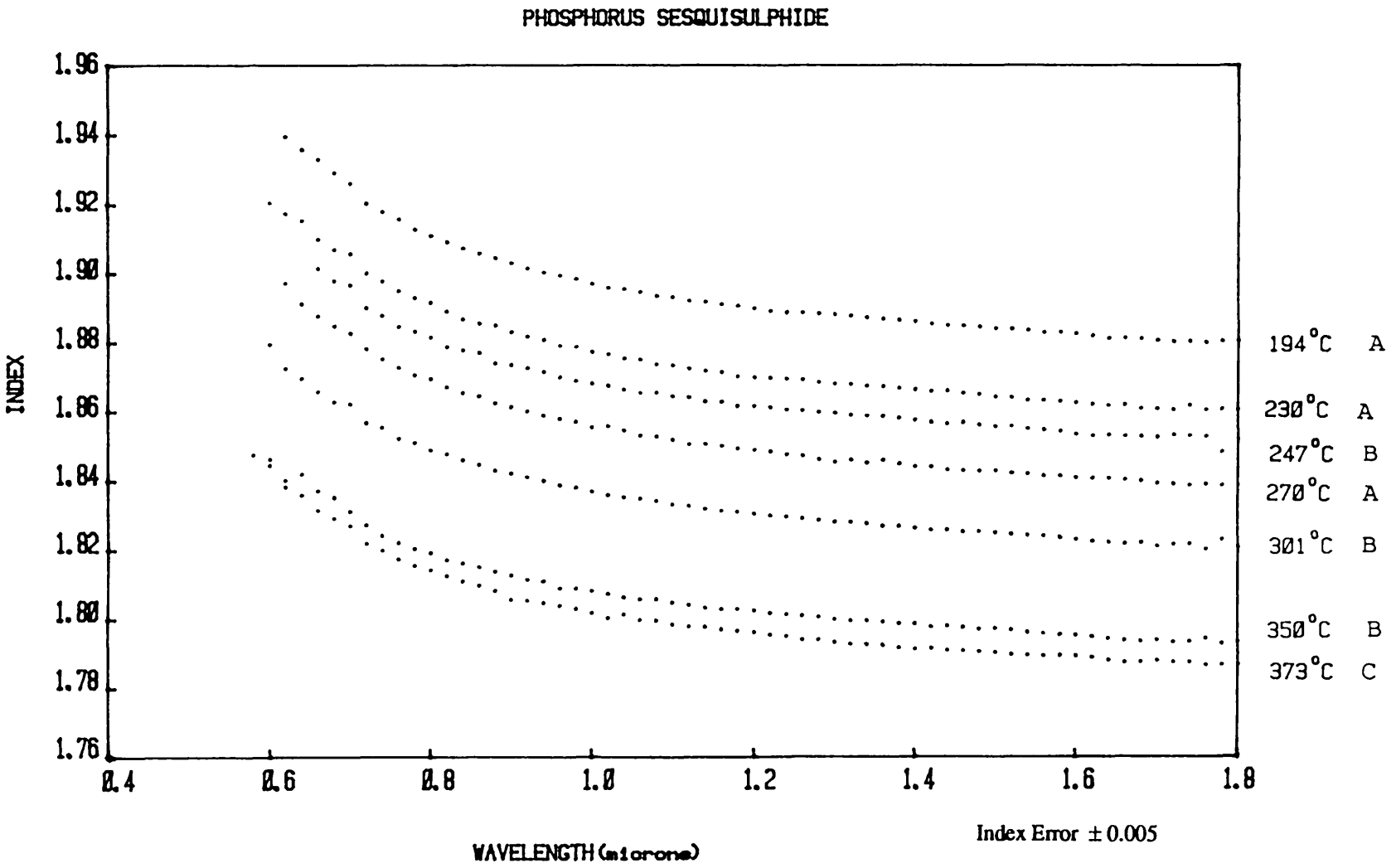


Figure 3.04: Wavelength dependence of the refractive index for seven different sample temperatures.

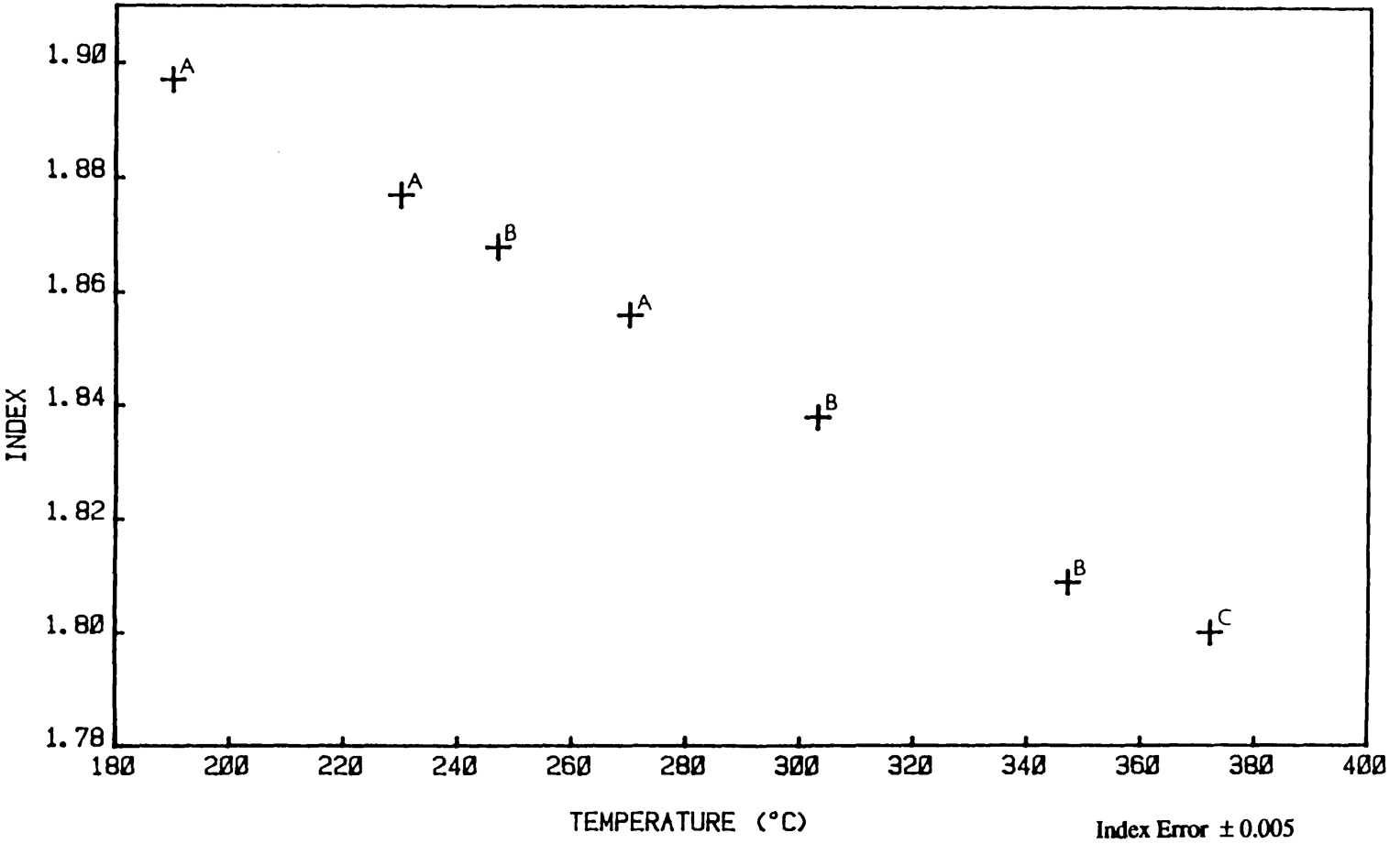


Figure 3.05: Refractive Index (at 1μm) as a function of temperature.

short wavelength measurements to coefficients of less than 70 cm^{-1} ; whilst the long wavelength range is restricted to 1.2 μm by the sensitivity of the large area silicon photodiode detector. Once again the sample melted to form a pale yellow liquid which reversibly darkens to a brown colour as the temperature is raised. The measured optical absorption coefficients at three different temperatures are shown in Figure 3.06, and the visual colour observation can be seen to correspond to a steady shift of the absorption edge as the sample temperature increases.

Discussion of Results

The refractive index measurements presented in Figure 3.04 are taken from three independently prepared samples. This was required since, prior to redesigning the cell heating block, sample leakage would cause the surface meniscus to fall below the incident light beam. Samples A, B and C were all observed to form clear yellow liquids and Figure 3.05 shows a consistent variation of index with temperature. Some other sample batches that were prepared formed pale yellow crystals, but on melting they became cloudy brown/yellow liquids. Such samples also showed an increase in index of ~8% and these properties were attributed to some sort of impurity contamination.

Recall from Chapter 1 that below the onset of absorption the refractive index can be fitted to the single oscillator dispersion equation, 1.31. As the frequency ω approaches the resonance frequency ω_j, then $(\omega_j^2 - \omega^2)$ decreases and the refractive index, $n(\omega)$ will gradually increase. This normal dispersion characteristic is observed at all temperatures in figure 3.04.

The measured data can be fitted to the single oscillator expression of Wemple and DiDomenico:-

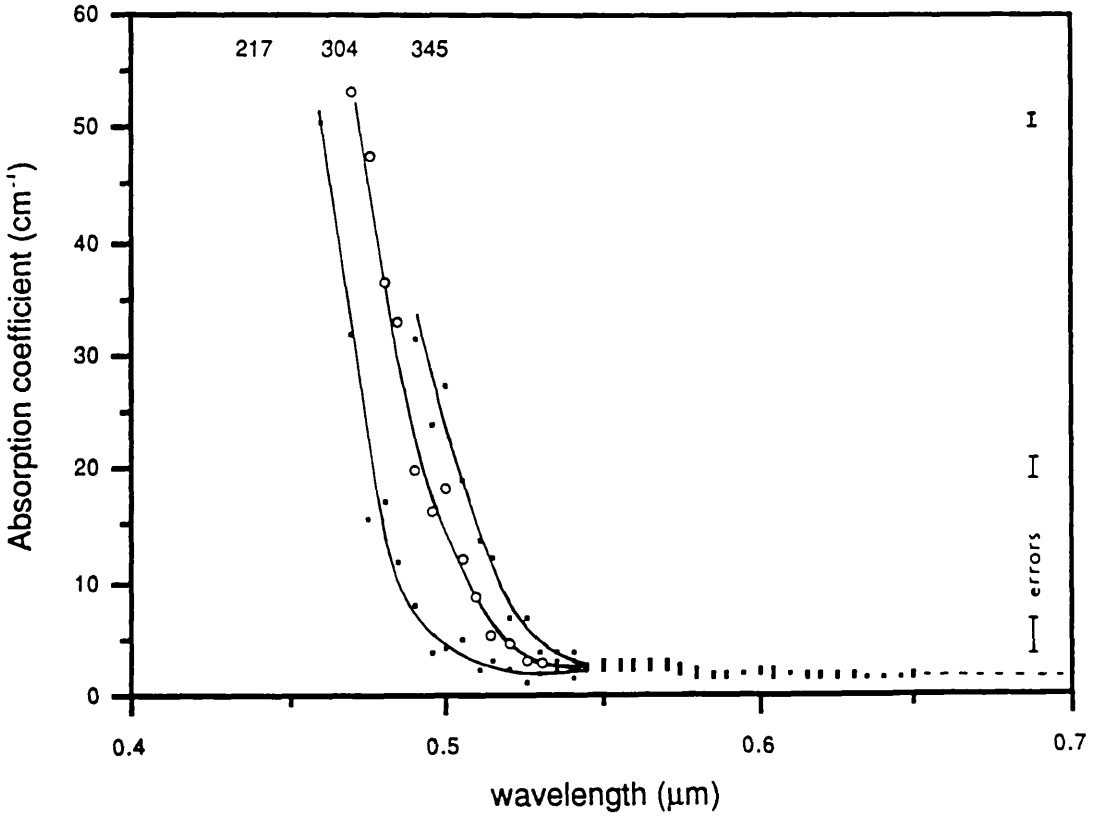


Figure 3.06: Wavelength dependence of the absorption coefficient at different temperatures.

$$(n^2(E) - 1)^{-1} = \frac{-E^2}{E_d E_0} + \frac{E_0}{E_d} \qquad 3.01$$

Hence by plotting $(n^2-1)^{-1}$ against the square of the energy, for the seven sample temperatures the results are seen to follow the dispersion equation very well, Figure 3.07. The slight departure from linearity at low energies is probably due to near infrared absorption bands which would cause the index to fall as we approach the region of anomalous dispersion. Studies of the infrared absorption spectrum have been made by Chattopdhyay et al (1981). Strong absorption bands were observed between 20μm and 50 μm, however no measurements were made below 18 μm.

By extrapolating the straight line data of Figure 3.07 we can obtain the zero frequency refractive index, n* (o), at each temperature. Figure 3.08 shows the squared zero frequency refractive index; the temperature dependence of which is again due to the samples decreasing density.

The two energy parameters E_d and E_o can be calculated from the gradients and intercepts of Figure 3.07. Figure 3.09 (a) shows the values of E_d for the seven sample temperatures. By considering the two independent samples, A and B (Figure 3.09 (b)), E_d is seen to be temperature dependent. The calculated average energy gaps E_o are shown on Figure 3.10 and once again the different sample batches are clearly illustrated.

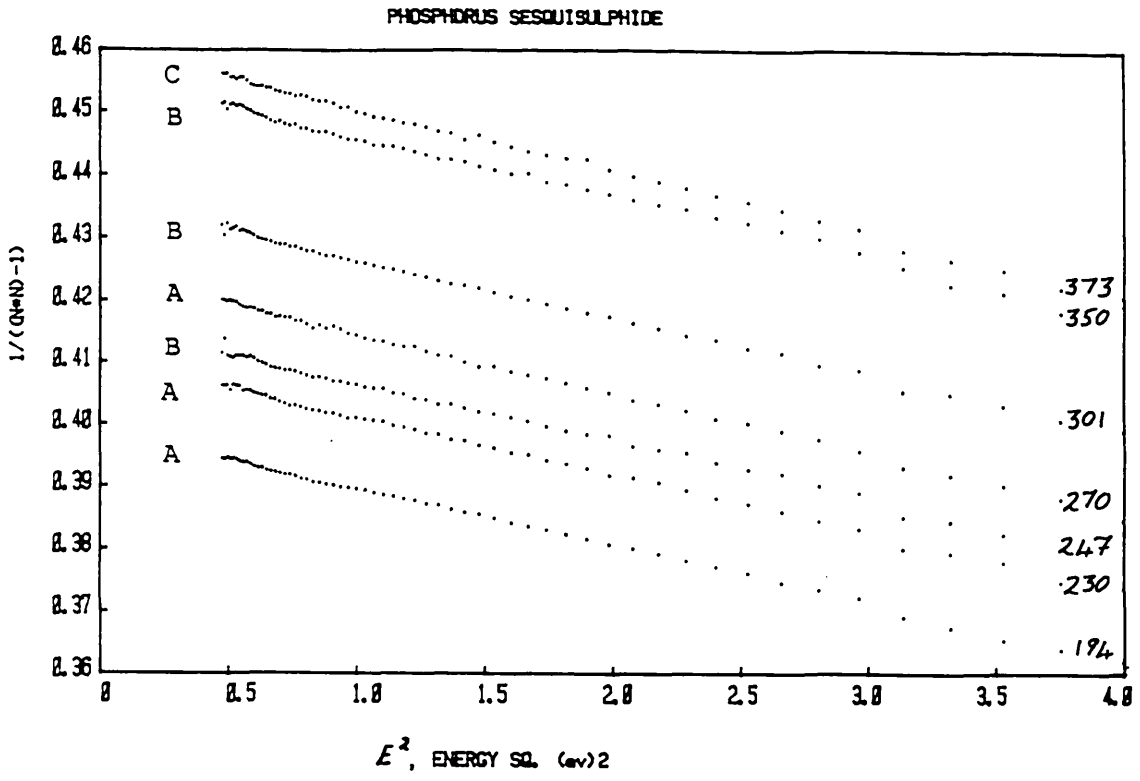


Figure 3.07: Dispersion of the refractive index.

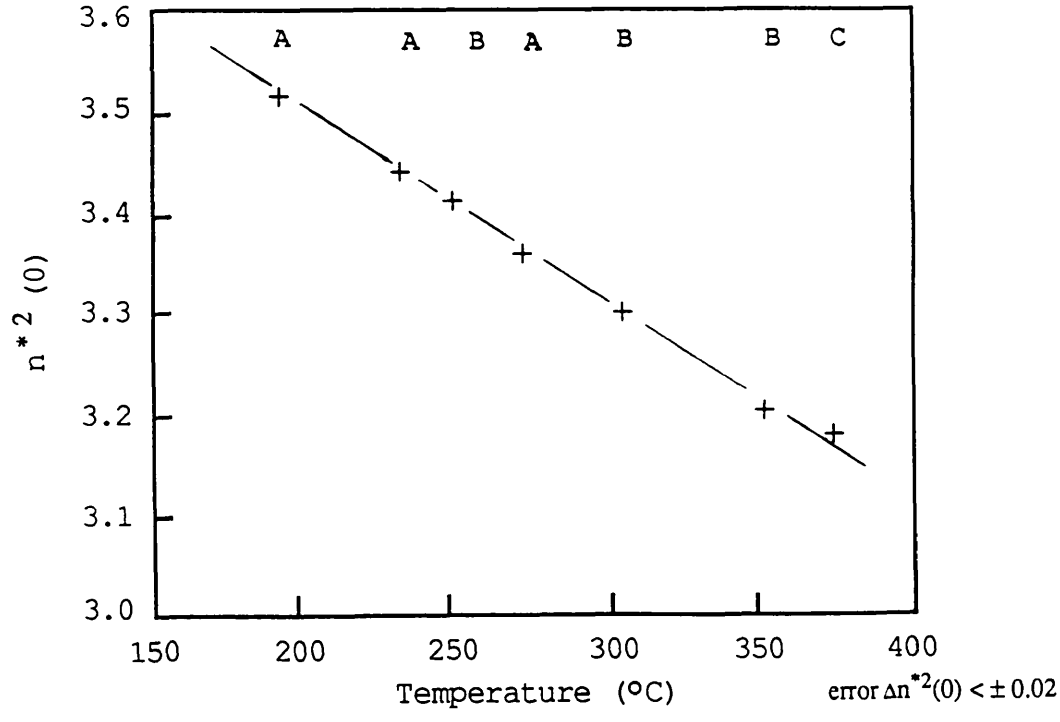


Figure 3.08: Squared zero frequency refractive index for P_4S_3

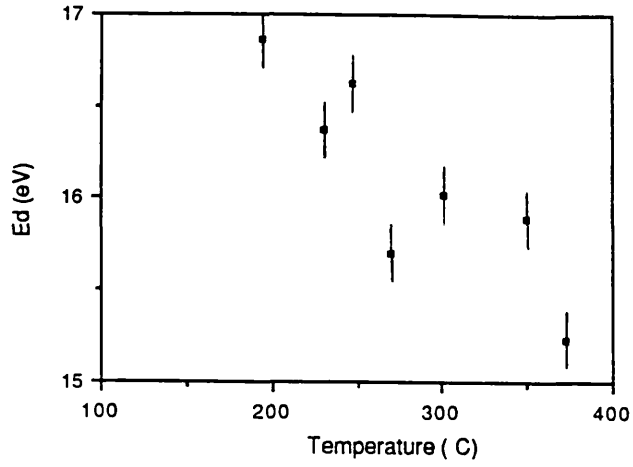


Figure 3.09(a): Transition strength dispersion parameter E_d.

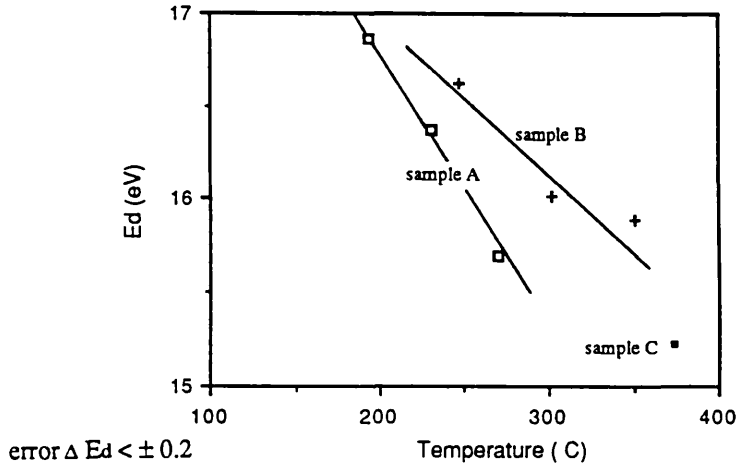


Figure 3.09(b): Temperature dependence of E_d for samples A, B and C.

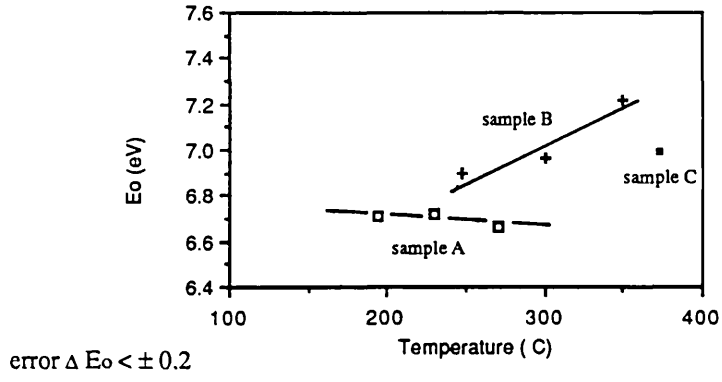


Figure 3.10: Average energy gap dispersion parameter, E_0.

The measured absorption coefficients for P_4S_3 were illustrated in figure 3.06. Figure 3.11 shows the absorption edge of P_4S_3 plotted to illustrate the exponential dependence on photon energy; a rule discovered by Urbach (1953). With the low wavelength absorption edge of this sample, both the monochromator output and detector sensitivity are low, in the region of the absorption. These factors contribute to the errors and limit the maximum detectable absorption to $50\ cm^{-1}$. For the thin sample layer used in this experiment, the errors in the low absorption measurements are quite large ($\sim \pm 3\ cm^{-1}$) , hence the measurements only indicate an absence of other absorption bands.

Electronic Polarisability of P_4S_3

At optical frequencies the contribution of orientational and atomic polarisation mechanisms are insignificant. We can therefore write the frequency dependent electronic polarisation $P_e(\omega)$ as:-

$$P_e(\omega) = (\varepsilon(\omega) - 1)\,\varepsilon_o E = \sum_j N_j \alpha_{e_j}(\omega)\, E_{loc} \qquad 3.02$$

where α_{e_j} = electronic polarisability of j'th species

N_j = number of j'th type molecules per unit volume

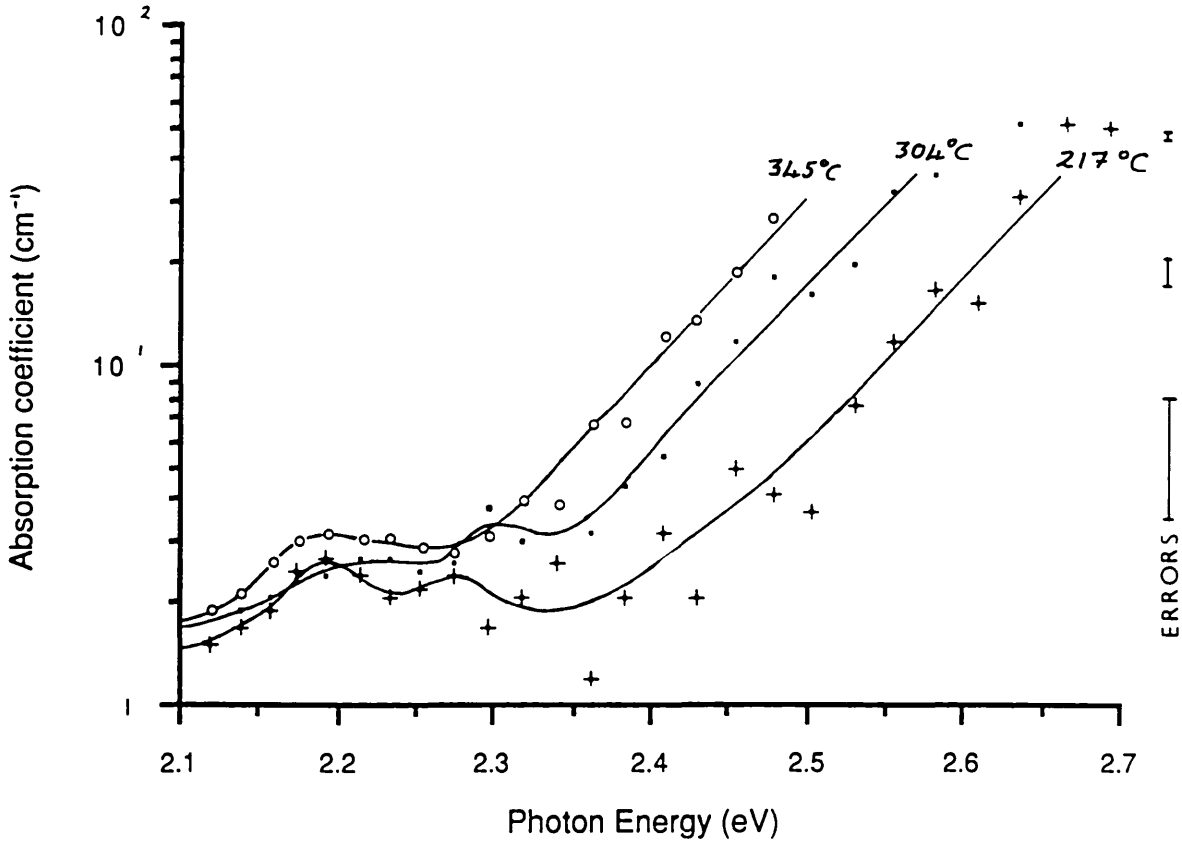


Figure 3.11: Exponential dependence of the absorption edge.

For liquids the Lorentz field is a commonly used approximation for the internal field, so that below the onset of absorption we obtain the Molar Refraction relation for one species of molecule:-

$$Rm = \frac{M}{\rho} \frac{n^{*2}(0) - 1}{n^{*2}(0) + 2} = \frac{N \alpha_e}{3 \varepsilon_o} \qquad 3.03$$

To calculate the electronic polarisability from equation 3.03, requires that the substance density, at temperature T, be known. The density of molten P_4S_3 , as a function of temperature, has never been studied. This is not surprising since the low autoignition temperature would make such measurements technically difficult and very hazardous. One measurement, made at the melting point, is given by Mellor (1956) as 1.7935 g/cm^3 (172 deg. C.). From Figure 3.08 we can interpolate for $n^{*2}(0)$ at 172 deg. C. and thus calculate the molar refraction, Rm as 56 ± 2 (cm^3) . This value is consistent with the results of Rogers and Gross (1952), who measured the index of P_4S_3 in Benzene solutions, and give Rm as $57.8 cm^3$. Returning to equation 3.03 and calculating the electronic polarisability at 172 deg C., we obtain $\alpha_e = 2.5 \pm 0.1 \times 10^{-39}$ Fm^{-2} . Once again there is an absence of data with which to compare this calculation but the value does seem reasonable.

CHAPTER 4

Chalcogenide Glasses

The chemical analogues of oxygen in the Periodic Table, namely sulphur, selenium and tellurium, are termed Chalcogens and their compounds with elements of groups IV and V are called chalcogenides.

The major difference between chalcogenide glasses and the oxide (and halide) glasses may be illustrated by comparing the compounds As_2O_3 and As_2S_3 . Both are glass formers and they have similar structures. Because oxygen is a gas at room temperature the only melt which can be made at normal pressures in the system arsenic-oxygen is that having the composition of the trioxide (As_2O_5 decomposes on heating). In the arsenic-sulphur system, melts can be made from all compositions from pure arsenic to pure sulphur. Thus in the latter system glass formation can occur over a range of compositions and is not confined to the trisulphide melt.

Since the early 1960's chalcogenide glasses have been actively researched in order to determine their suitability as passive bulk optical component materials for infrared applications and as active electronic device components in photocopying and electronic switching applications.

In general the normal oxide based optical glasses do not transmit beyond 3-5 μm, this is because of the strong absorption of chemical bonds formed with the light chalcogen element, oxygen. The arsenic containing glasses were the

first to be studied and As_2S_3 glass was originally described in 1870 by Schultz-Sellack (1870). The first attempt to extend the wavelength range of glasses was carried out by Frericks (1953). In his studies on As - S glasses, Frericks prepared the As_2S_3 glass by distilling technical grade arsenic sulphide in a stream of hydrogen sulphide. The condensed liquid was found to have a good transmission in the infrared up to 12 μm and its chemical stability was reported to be good compared with that of many other infrared transmitting materials.

The need for Infrared Optical Materials

The transmission requirements of infrared transmitting materials are set primarily by atmospheric absorption and secondly by the operating wavelength range of the sources and detectors.

The gases present in greatest abundance in the earth's atmosphere are nitrogen, oxygen, carbon dioxide, methane, nitrous oxide, carbon monoxide and ozone. Fortunately the two gases present at the highest concentrations, N_2 and O_2, are homopolar. They therefore possess neither a permanent nor an induced dipole moment, and hence do not exhibit molecular vibrations which would result in the absorption of infrared radiation. At low altitudes, water vapour and carbon dioxide are by far the most important absorbing molecules; contributing to form three main windows in the

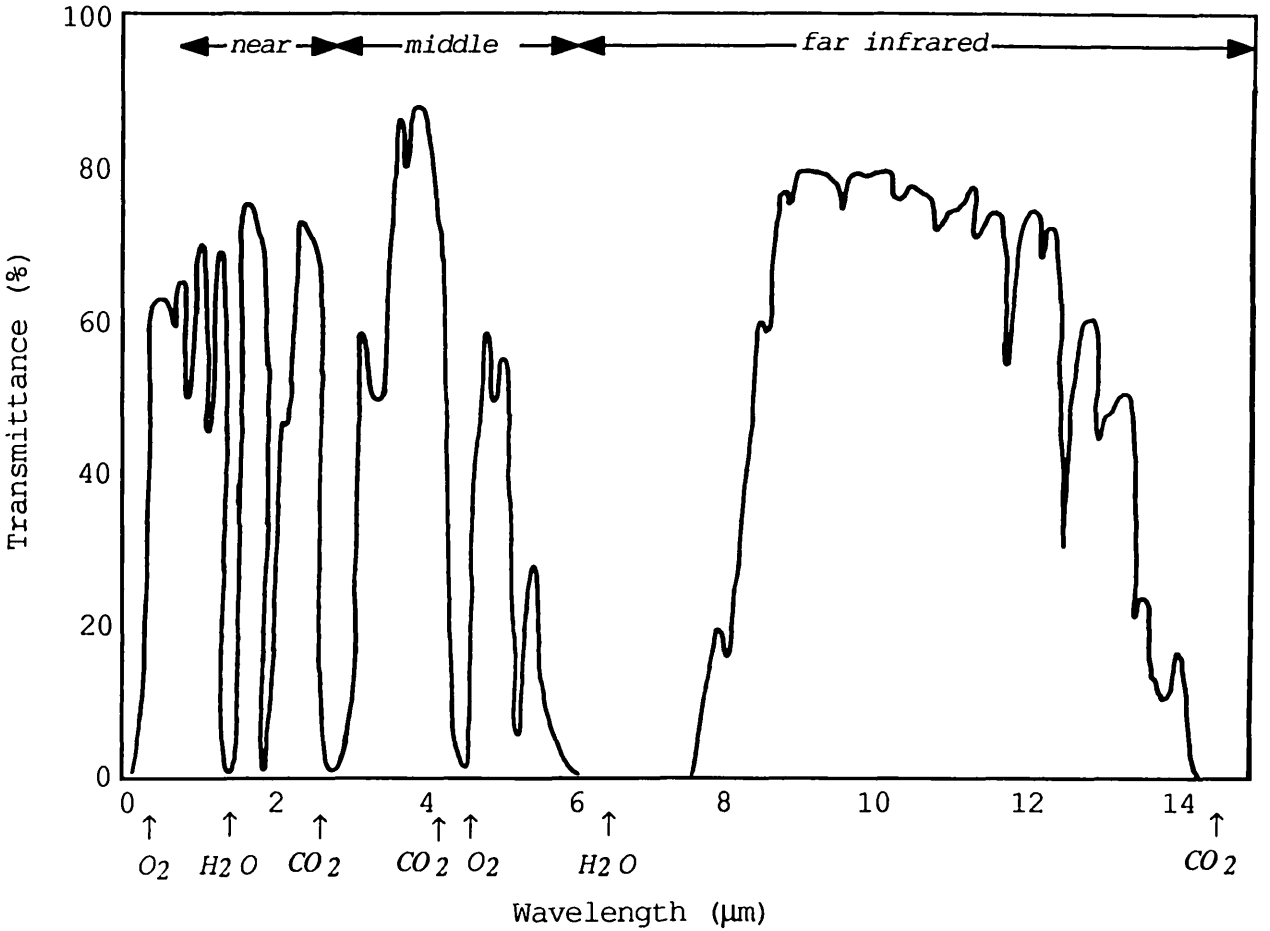


Figure 4.01: Atmospheric molecular absorption spectrum (transmittance over 6000 ft at sea level).

atmospheric molecular absorption spectrum, Figure 4.01. The first window ranges from 0.75 μm to 2.5 μm (near I.R.), the next from 3.0 to 5.0 μm (middle I.R.) and the third from 7.5 to 14 μm (far I.R.).

Properties of Chalcogenide Glasses

COMPOSITION: Glasses with high softening temperatures have been made from combinations of the elements Si, Ge, P, As and Sb with S, Se or Te, and some of the simple ternary systems in which glass formation is possible are shown in Figure 4.02. Glasses with low softening temperatures have been melted from combinations of As, Sb, Bi, Tl, Br and I with S, Se or Te. Several of these low melting point ternary systems are shown in Figure 4.03. Little blending of these three component systems has yet been attempted but such complex systems would allow a wider variation of physical properties.

CHEMICAL DURABILITY: The softening temperature provides an estimate of the temperature at which a glass will deform under its own weight. Several different methods have been used to make this measurement so that the values for any given composition can vary by up to 10 per cent. The reported softening temperatures vary widely as a function of composition, ranging from below room temperature to over 500 deg. C.

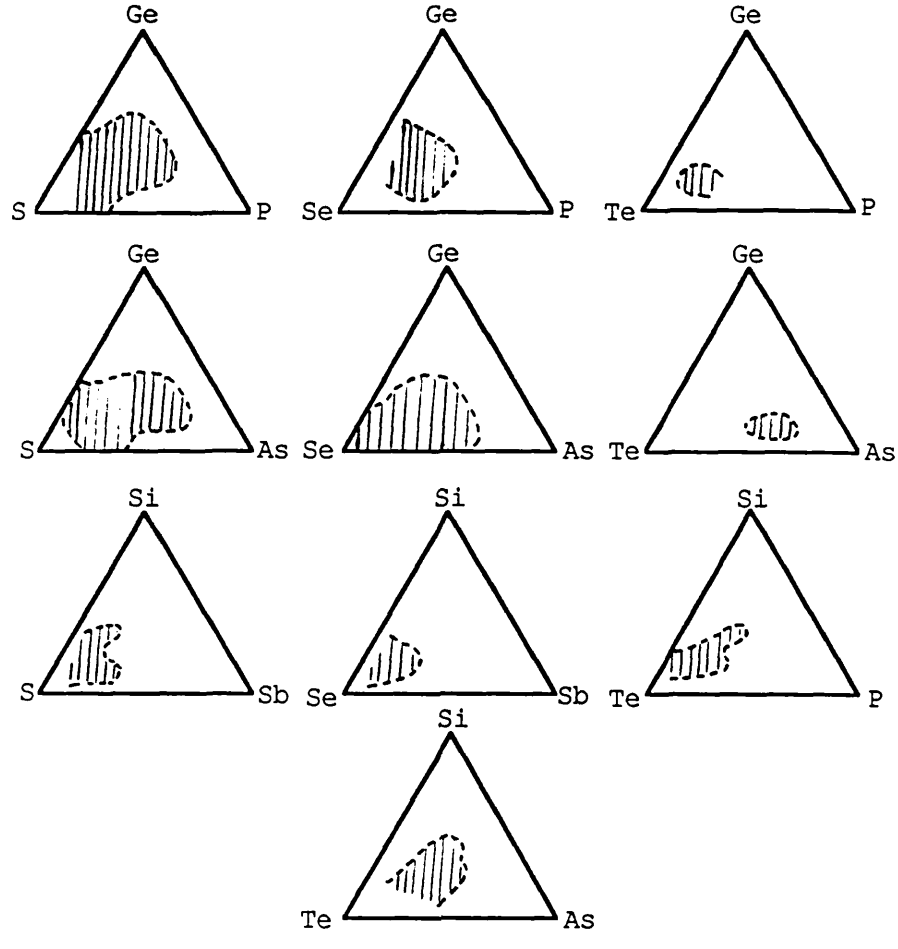


Figure 4.02: High softening temperature ternary glass forming system (ref. Savage & Nielson, 1965).

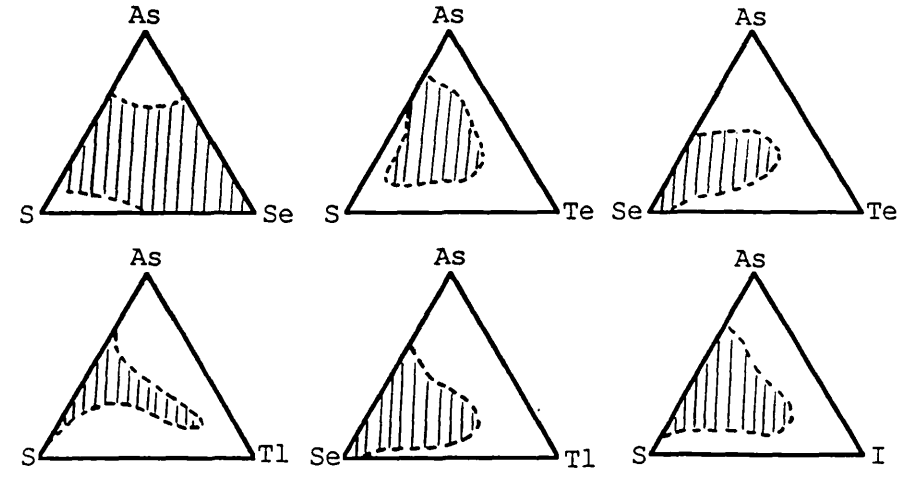


Figure 4.03: Low softening temperature ternary glass forming systems (ref. Savage & Nielson).

To a great extent the physical properties that determine the practicability of a particular glass composition are all interrelated. This is illustrated in Figure 4.04 where the measured hardness of over 100 different glass compositions is plotted against the measured softening point of the same glass. A similar plot for the softening point and thermal coefficient of expansion is given in Figure 4.05. High softening point glasses have low coefficients of expansion, therefore in order to have a hard glass (300 knoop) with low thermal coefficients of expansion then softening points of 700 deg. C. must be obtained.

Examples from high temperature systems are Ge-As-S glasses with softening temperatures up to 500 deg C, Ge-As-Se glasses 450 deg. C. and Si-As-Te glasses 460 deg. C. The effect on the softening temperature of increasing the Ge or As composition of sulphide and selenide glasses is illustrated in Figure 4.06, where it can be seen that Ge is much more effective than As in increasing the softening temperatures.

Sulphur and Selenium glasses consist of an arrangement of rings and chains with covalent bonds inside the chains and Van der Waals bonds between them. To increase the softening temperature, it is necessary to replace the Van der Waals bands by stronger covalent bonds, thereby crosslinking the chains. Because As and especially Ge form strong covalent bonds with S and Se, the softening temperature of glasses containing these elements are increased. A decrease in softening temperature is produced

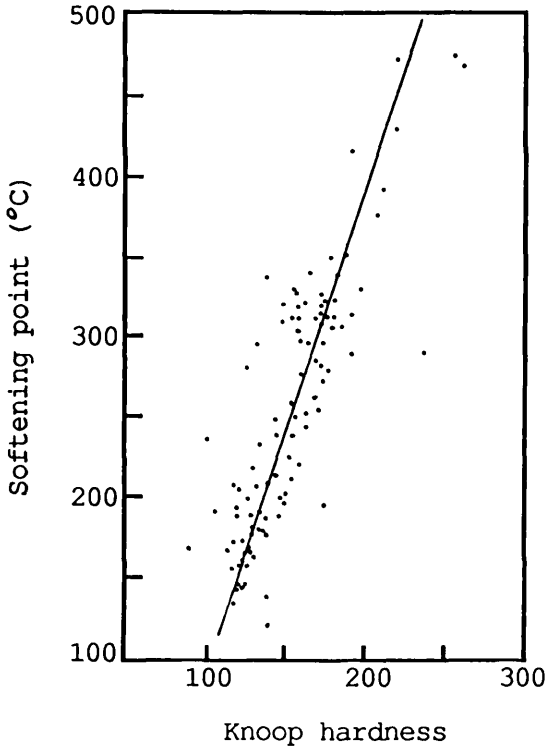


Figure 4.04: Inter-relation of softening temperature and hardness.

Ref. Hilton (1966)

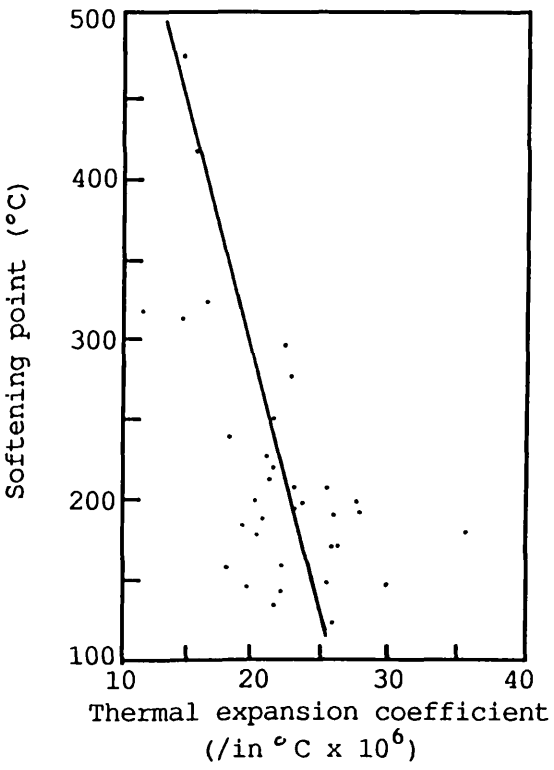


Figure 4.05: Inter-relation of softening temperature and thermal expansion.

Ref. Hilton (1966)

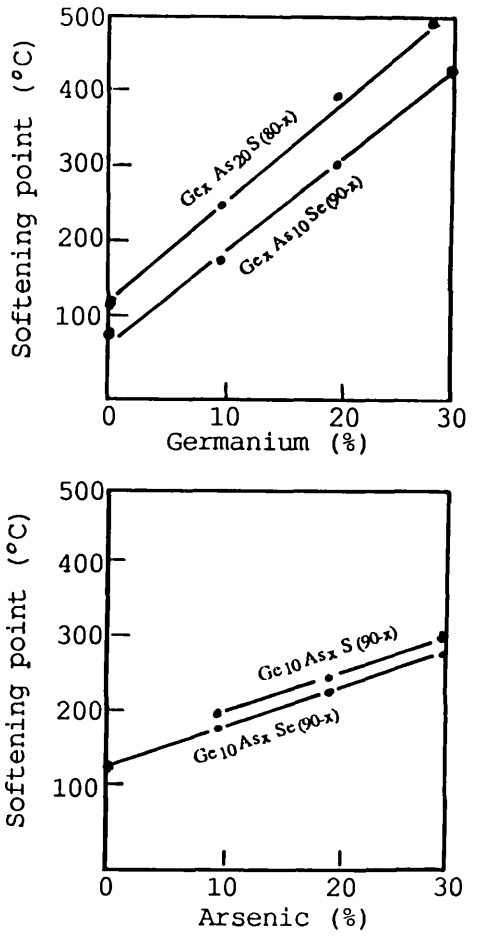


Figure 4.06: Dependence of softening temperature on Ge and AS composition.

Ref. Hilton (1966)

by the addition of a halogen, such as iodine, which does not form strong chemical bonds with S or Se and acts as a chain terminator.

Optical Properties

Metallic materials possess a high density of free electrons in their structure. These electrons are of such low inertial mass that they can freely respond to electromagnetic radiation over a wide frequency range and thus metals are opaque in significant thicknesses. Insulators and semiconductors with energy gaps greater than ~0.1 eV will exhibit some near, middle and far infrared transmission within their transparency range. The short wavelength cut-off frequency in these solids is determined by electronic transitions across the band gap, while the long wavelength cut-off results from lattice absorptions due to vibrational modes of the atoms, or ions, of the solids.

The mechanisms which give rise to bulk absorption may be classified as intrinsic or extrinsic. The intrinsic absorption mechanisms are those which result in electronic and vibrational structural absorptions. These intrinsic mechanisms define the region of transparency to electromagnetic radiation in a solid and gives the ultimate transmission achievable. Extrinsic loss mechanisms determine the fraction of the theoretical level of transparency which is achievable in the glass. These mechanisms are scatter and

absorption arising from the fabrication process employed and the chemistry of the glass in relation to certain specific impurities. For instance, OH, hydrocarbons and oxygen in chalcogenide glasses can give rise to unacceptable absorptions at specific wavelengths. Inadequately homogenised glass can give rise to unacceptable scatter in the high frequency regions of the near and middle infrared. These loss mechanisms are now illustrated by considering particular glasses.

The transmission of three purified sulphide glasses of composition $As_{20}S_{80}$, , $Ge_{30}As_{40}S_{30}$, and $As_{40}S_{60}$ are shown by the full curves of Figure 4.07 (a), (b) and (c) respectively. The bands in the curve of 4.07 (a) at 7.7, 10.15, 10.75 and 11.9 μm are S-S combination tones which are seen in sulphur rich glasses, while the strong band between 13 and 15 μm is attributed to As-S combination tones. Glasses rich in As and Ge, and low in S, do not exhibit the S-S fine structure seen in Figure 4.07 (a) but the transmission limiting As-S and Ge-S band between 13 and 15μm is still present, as in Figure 4.07 (b). Impurity bands which have been observed in sulphide glasses are shown by the dashed curve in Figure 4.07 (c) and the origins of these absorptions are also shown.

Selenide glasses containing the same two elements Ge and As transmit farther into the infrared. The impurity free transmissions of the selenide compositions $As_{40}Se_{60}$ and $Ge_{34}As_8Se_{58}$ are shown by the full curves of Figure 4.08.

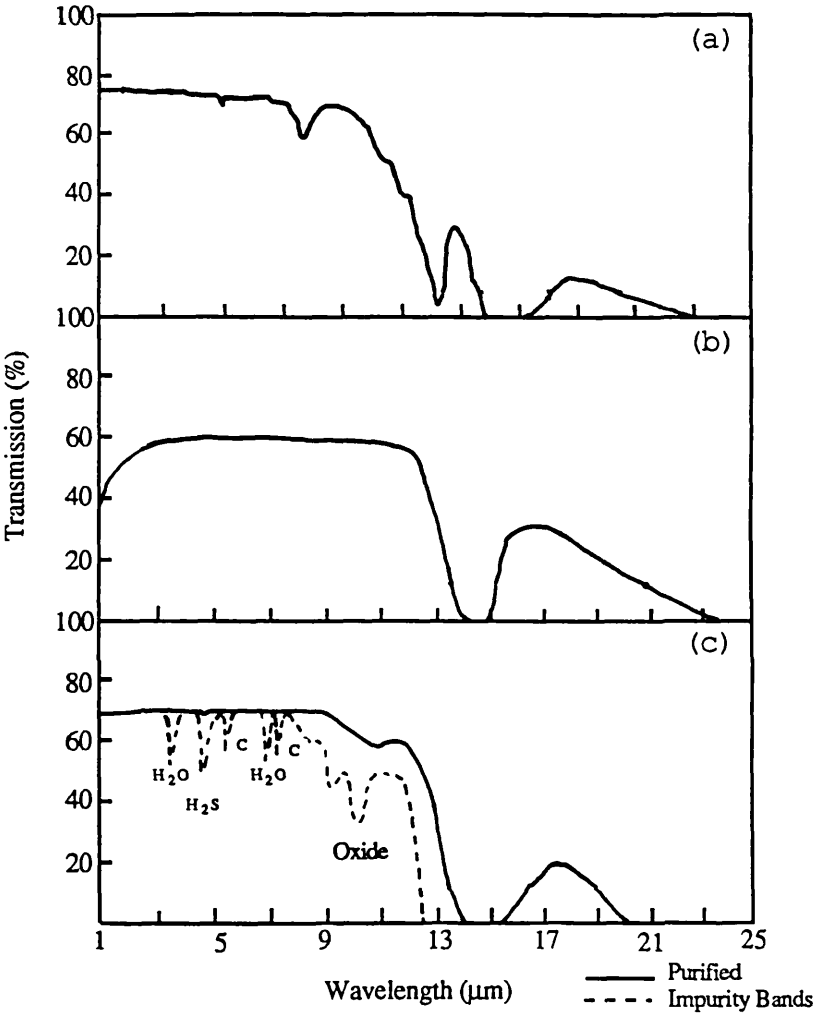


Figure 4.07: Infrared transmission of sulphide glasses
(a) As20 S80
(b) Ge30 As40 S30
(c) As40 S60

Ref. Savage & Nielson (1965)

There are absorption bands between 17 and 23 μm which are attributed to Ge-Se and As-Se combination tones and it is noticeable that these occur at longer wavelengths than the corresponding sulphide bands. Therefore purified selenide glasses are capable of transmitting in useful thicknesses from 1 to 15 μm. The dashed curves show the dramatic effect of small amounts (estimated ~0.05 atomic per cent) of oxide impurities on the transmissions of selenide glasses.

The field of glass formation in the Ge-As-Te system is limited to a small area in the low Ge (10%), high As (40-60%) region. The full curve of Figure 4.09 shows the transmission of an impurity free $Ge_{10}\,As_{50}\,Te_{40}$. Oxide impurity does not have a great effect on the transmission of Ge-As-Te glasses as seen by dashed curve, and it can be seen that such Telluride glasses have a useful transmission between 2 and 20 μm.

Most chalcogenide glasses are not transparent in the visible, so that it is not easy to detect inclusions, bubbles or other inhomogeneities which would affect absorption coefficient measurements. Impurities, which result in absorption bands, will also lead to erroneous results. Measurements show that values of the absorption can be as low as 0.05 cm^{-1} in the As-Se-Te system. Values of refractive index for some chalcogenide glasses are 2.48 (1 μm) for As_2S_3 , and 2.93 (1 μm) for As_2Se_3 .

The crystalline form of As_2S_3 and As_2Se_3 have monoclinic structures and possess three principal indices of refraction. The indices of As_2S_3 at 1μm are given by Palik

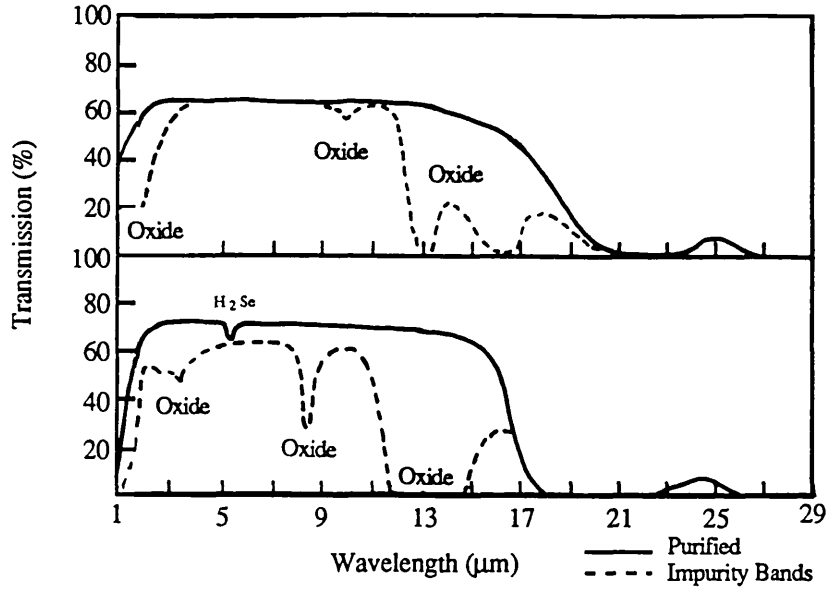


Figure 4.08: Infrared transmission of selenide glasses.
(a) AS40 Se60
(b) Ge34 As8 Se58

Ref. Savage & Nielson (1965)

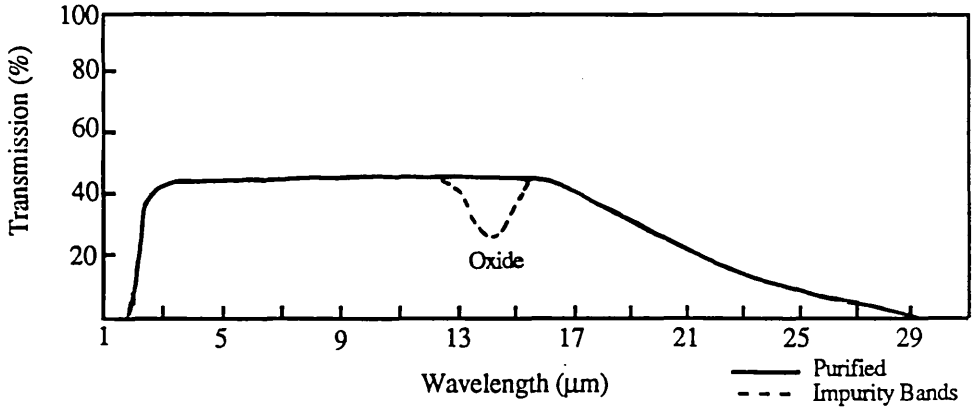


Figure 4.09: Infrared transmission of a telluride glass
Ge10 As50 Te40

Ref. Savage & Nielson (1965)

(1985) as $n_a = 2.98$ and $n_c = 2.64$; the value n_b not being given since micaceous cleavage in these crystals make it difficult to obtain optical data perpendicular to the layered structure.

Application of Chalcogenide Glasses

Chalcogenide glasses make good infrared optical materials for windows, lenses, telescopes etc and are used in thermal surveillance systems. The black body spectral emittance curve, Figure 4.10, shows that the 3-5 μm window is most suitable to detect relatively hot objects whilst the 7.5-14 μm window is suitable for room temperature objects. (The eye sensitivity curve is also drawn, showing that at higher temperatures a large part of the radiation contributes to visible light).

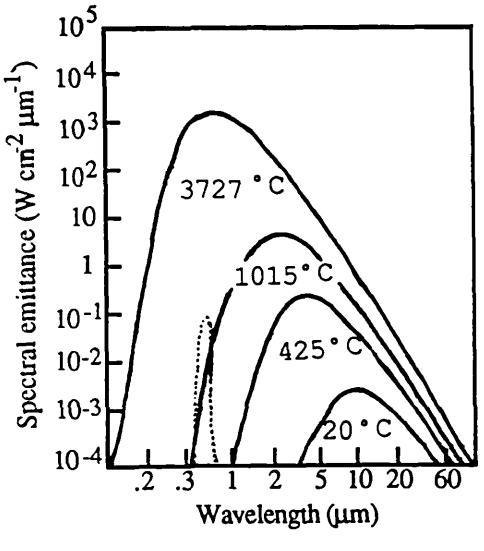


Figure 4.10 Black-body Spectral Emittance Curves

The mid-infrared wavelength of the CO_2 laser, 10.6 μm, is strongly absorbed by many materials permitting clean localized cutting, welding and heat treatment. Many uses of the laser has been restricted by the lack of good quality optical fibres at this wavelength. However the preparation of low toxic chalcogenide fibres has been investigated for uses in CO_2 laser endoscopy.

Photo induced effects in chalcogenide glasses have applications in optical-imaging, holographic recording and optical mass memories. Some of the effects can be stimulated by X-ray and electron beams, giving potentially very high resolution photo-resists with uses in fabricating intergrated circuits.

Experiments on chalcogenide glasses are of great interest to theorists since these glasses are close to structural equilibrium. The behaviour of these glasses are quite reproducible from sample to sample, and success in understanding their properties may help in understanding other materials such as amorphous silicon.

CHAPTER 5

OPTICAL PROPERTIES OF CHALCOGENIDE IODIDES OF ARSENIC

Introduction

With the addition of iodine to Arsenic Sulphides and Arsenic Selenides there is a considerable reduction in viscosity, and some of the resulting materials are quite fluid even at room temperature. Both these ternary systems have an extensive range of glass forming compositions which are illustrated on their ternary phase diagrams, Figures 5.01 and 5.02 below.

The low melting points and good transmission of these materials enabled us to study their optical properties using the methods and safety precautions developed for Phosphorus Sesquisulphide.

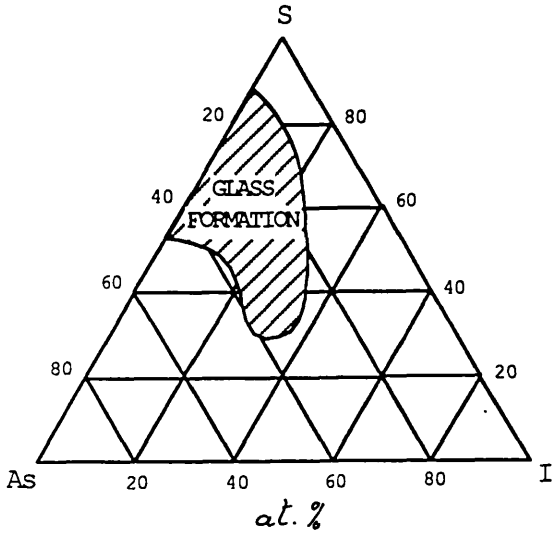


Figure 5.01: Glass formation in the AS-S-I system.

Ref. Flaschen et al (1960a)

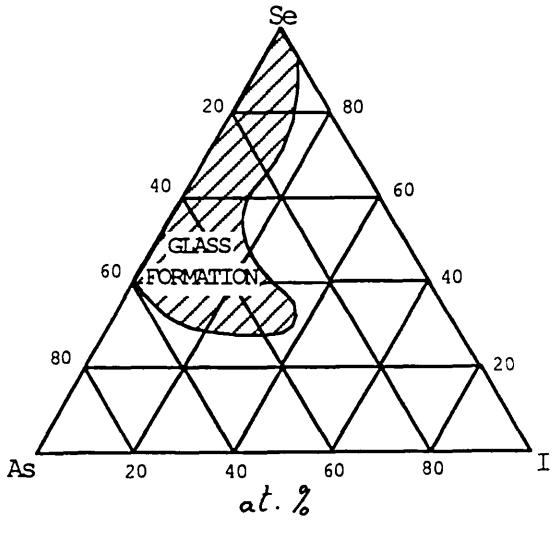


Figure 5.02: Glass formation in the As-Se-I system.

Ref. Khiminets et al (1978)

SECTION 1: ARSENIC-SULPHUR-IODINE SYSTEM

Structure and Properties of As-S-I

The ternary system of As-S-I glasses was first reported in 1959 by Flaschen et al (1960a), who showed it to have an extensive area of glass formation, limited at high sulphur concentrations by liquid immiscibility with sulphur compounds, and at low sulphur concentrations by crystalline phase formation, Figure 5.03. These glasses possess remarkably low melting points and the softening points measured by Flaschen et al are also presented on Figure 5.03.

The glasses are non flammable and are resistant to air oxidation to 330 deg. C. Their chemical durability was studied by Lin and Ho (1962) and can be summarized as follows:-

1. The As-S-I glasses are more resistant to acidic solutions than to basic solutions.

2. In general, increasing the iodine content decreases the chemical durability of the glass.

3. The rate of attack in alkaline solution increases linearly with increasing temperature.

4. Attack by acid or alkaline is initially very rapid but decreases with time due to a thickening layer of reaction product.

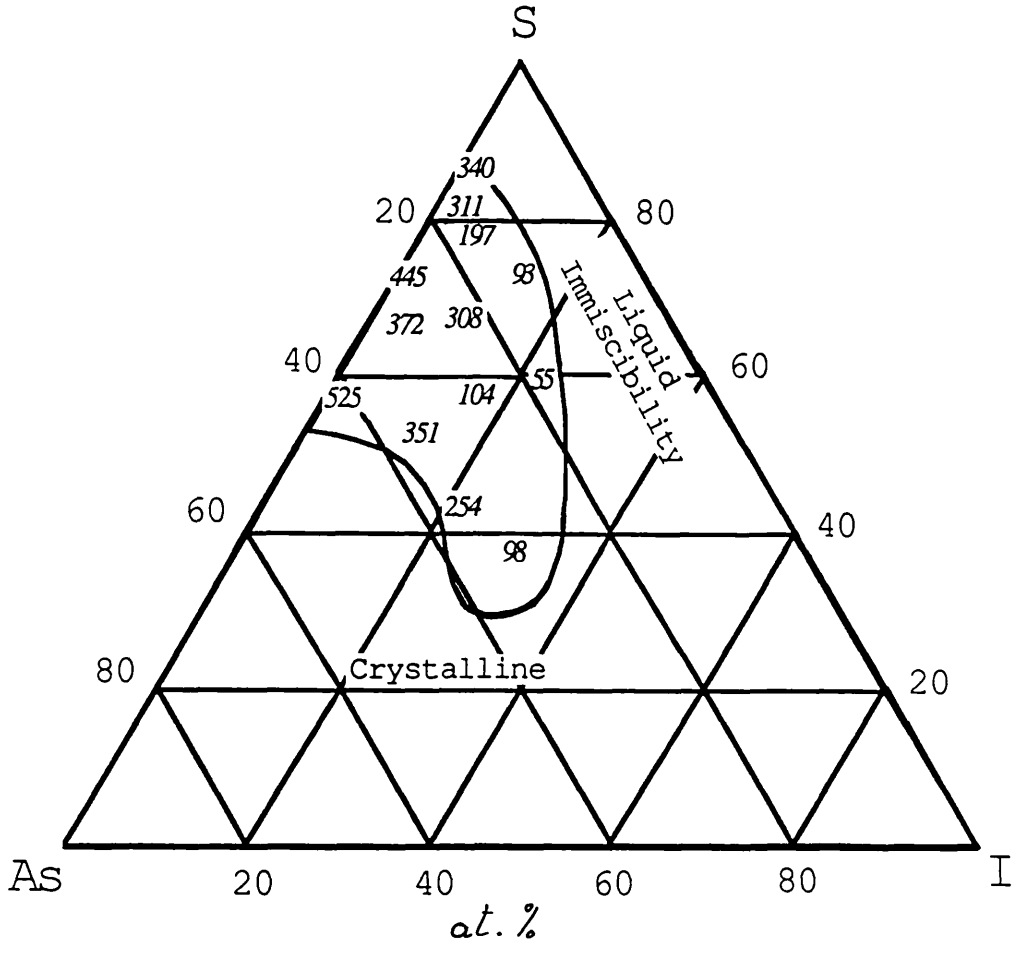


Figure 5.03: Glass formation and softening temperatures in the As-S-I system (Ref. Flaschen et al, 1960(a)).

Early structural studies in the vicinity of the equiatomic As S I composition were made, using X-ray diffraction, by Hopkins et al (1962) and later by Poltavtsev (1975). From the calculated radial distribution function, a glass structure was proposed consisting of twisted chains with structural units - S - As - S -

```
- S - As - S -
      |
      I
```

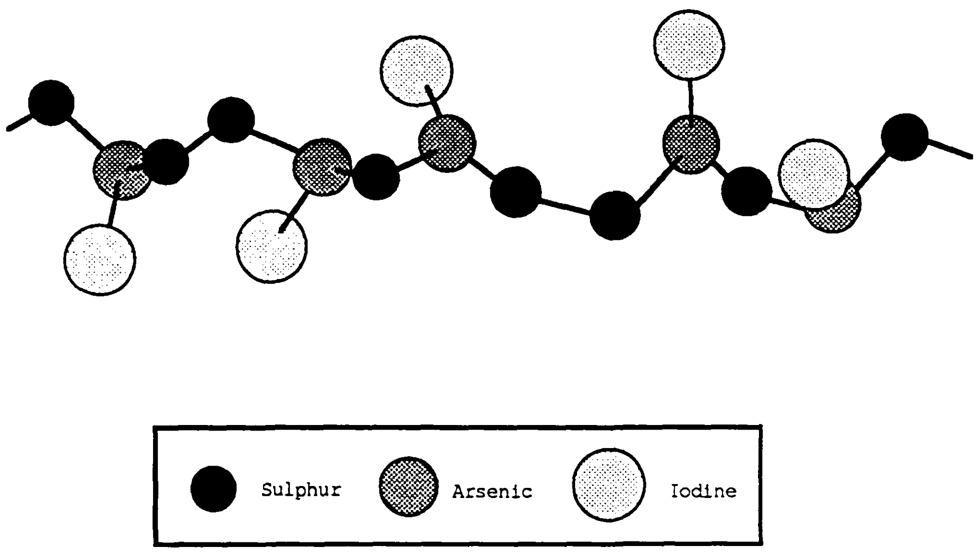


Figure 5.04 Twisted Chain Structure of As S I Glass

Complete studies of the structure of vitreous and glass-crystal materials in this system have been made by measuring the Raman Spectra (Koudelka and Pisarcik, 1983), and the Infrared Transmission spectra (Gerasimenko et al, 1977). From these studies the glass forming region was divided into four subregions in which the glasses have different structures, Figure 5.05.

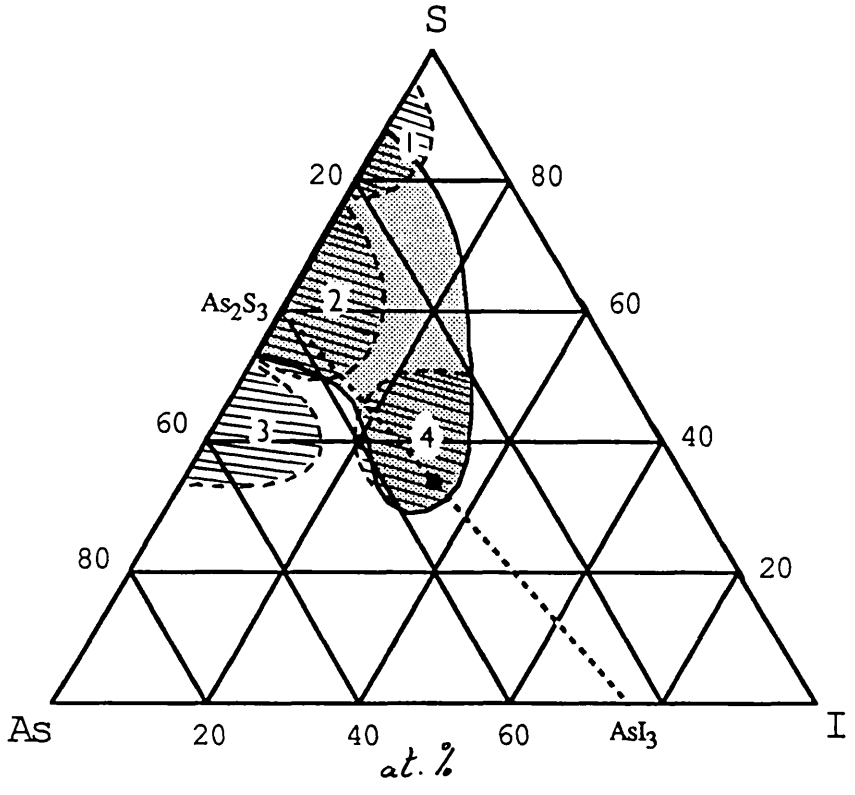


Figure 5.05: Subregions of glass formation with different structures.

Ref. Gerasimenko et al (1977)

REGION 1: This region consists of the structural network formed by AsS_3 pyramidal units interconnected via sulphur bridges. This structural network contains dissolved molecular species of AsI_3 and S_8; their content depending on the composition of the glass.

REGION 2: The structure of these glasses is formed by an As_2S_3 type disordered network and contains individual molecules of AsI_3. This structure extends up to 20 mole % AsI_3 and for slightly varying arsenic to sulphur ratios.

REGION 3: The Raman spectra of these arsenic rich samples were not distinguishable from those of region 2 because the excess of arsenic is relatively small. The infrared spectrum is analogous to that of glassy As_2S_2, except for additional absorption bands at 210 cm^{-1} which appear as a result of the formation of As-I bonds.

REGION 4: The spectra of samples in this region repeat the spectra of the equiatomic As S I composition, the structure is that of twisted chains illustrated in Figure 5.04.

This structural model agrees with the observations of Hopkins and Poltavtsev, and is also consistent with studies of glass formation in the binary As_2S_3 system. Region 3 lies outside the glass forming region of Figure 5.05, however Gerasimenko et al were able to prepare such samples, in the glassy state, by controlled quenching at a rate of 150 deg. per hour. These glasses were found to be highly unstable and

crystallise in a matter of minutes, therefore their absence on Figure 5.05 is justified.

The transition from the As_2S_3 disordered network of region 2 to the As S I chain structure of region 4 can be traced by studying the AsI_3 concentration dependence of various physicochemical parameters along the As_2S_3 - AsI_3 line. The viscosities of glasses along this section were studied by Chernov et al (1970), and structural information was obtained by analysing the viscous flow activation entropy, $S\eta$. Figure 5.06 illustrates the relationship between $S\eta$ and composition.

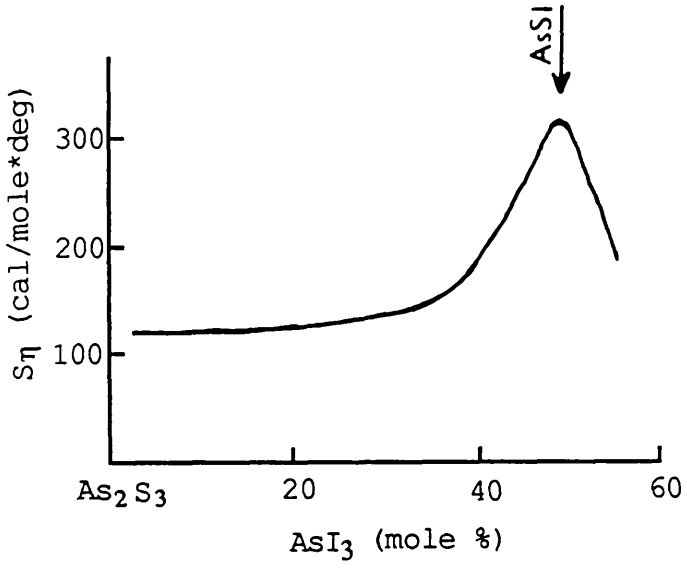


Figure 5.06 The Viscosity Flow Activation Entropy of As_2S_3 - AsI_3 Glasses
Ref. Chernov et al (1977)

As AsI_3 is added to As_2S_3 the value of $S\eta$ increases from a level characteristic of As_2S_3 up to values typical of the chain structure. A maximum occurs in the region corresponding to the equiatomic composition, after which the excess iodine provides chain terminators and causes $S\eta$ to fall.

Sample Preparation and Toxicity

To make a systematic study of the glass forming region seven different samples of varying composition were prepared, Figure 5.07 (a). These compositions where chosen as a convenient distribution of low melting point glasses in the weight percent phase diagram of Flashen et al, (1960a). In much of the later literature on these chalcogenide systems the compositions are presented in atomic percent and to avoid confusion we now adopt this system, Figure 5.07 (b).

To prepare a sample, appropriate amounts of each element were weighed out and sealed in evacuated pyrex reaction tube. These tubes had been shown to withstand pressures of up to 2000 lb/in (100 Bar), but because of the toxicity of the elements gradual heating was used to control the sample's vapour pressure. Initial heating up to 150 deg C melts the iodine and raises its vapour pressure to 500 mm Hg. As the iodine reacts with the arsenic, AsI_3 is formed and the vapour pressure is reduced. Subsequent heating up to 450 deg. C. forms the ternary compound, with the vapour pressure remaining relatively low. This temperature is maintained for ~12 hours. A few minutes agitation, before removing the tube from the furnace, ensures the homogeneity of the sample which is then allowed to air cool in the reaction tube.

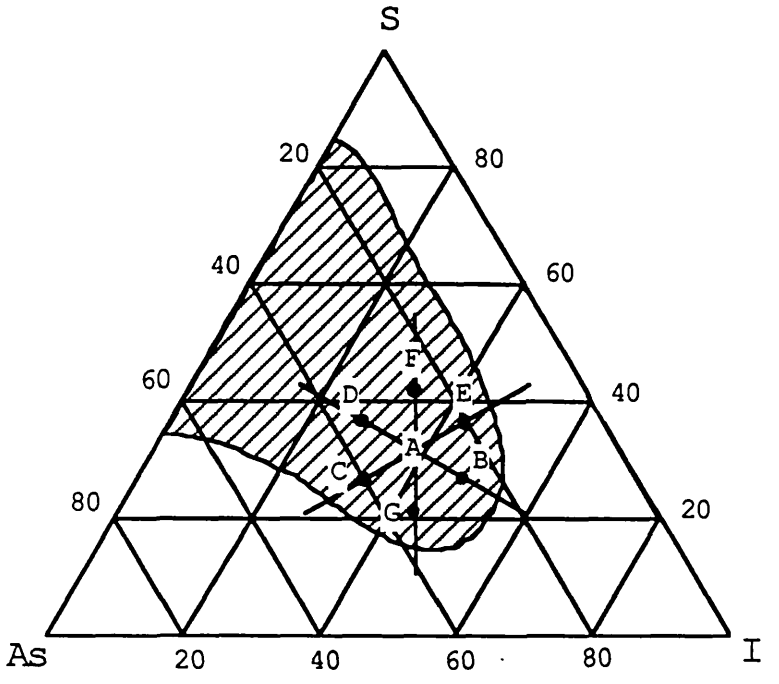


Figure 5.07(a): Seven As-S-I sample compositions covering the low melting point glass forming region of the wt.% ternary phase diagram.

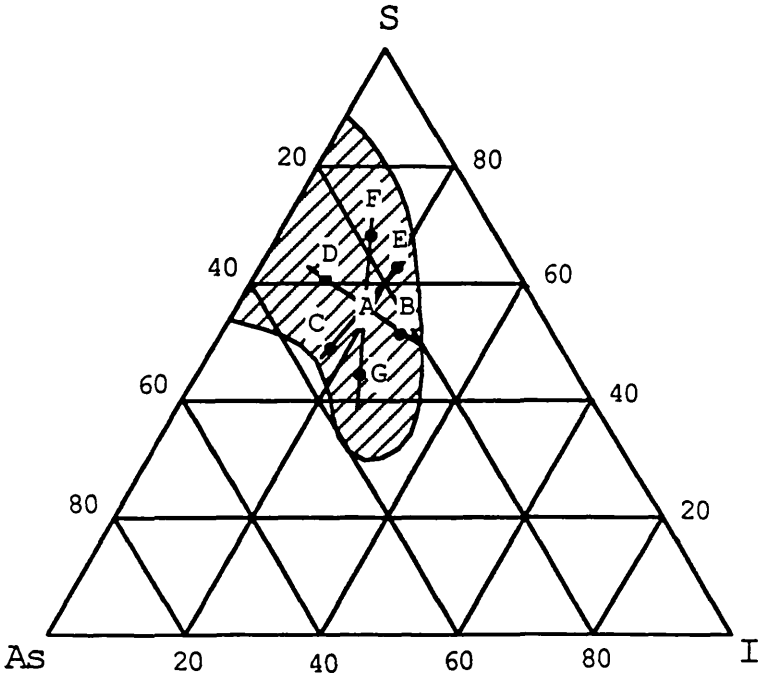


Figure 5.07(b): Distribution of As-S-I samples on the at.% ternary phase diagram.

Initially the prepared sample was poured from the opened reaction tube into the cell cavities by using a soldering iron heated brass block to melt the sample. This method proved difficult for the higher melting temperature samples so a neater alternative was devised: the sample was allowed to cool along the bottom of the horizontally laid reaction tube, which was then immersed in liquid nitrogen. Due to its greater thermal expansion coefficient, the sample pulls clean away from the pyrex tube and gentle tapping is sufficient to break up the column of sample. The reaction tube can then be scored and broken open leaving the loose sample retained in one end.

In preparing samples from the elements extreme care must be taken due to their toxicity. Arsenic compounds are very potent poisons and inhalation, ingestion or skin contact with subsequent absorption must be avoided. Iodine vapour, even at low concentrations, is extremely irritating to the respiratory tract, eyes and, to a lesser extent, the skin; whilst sulphur dust has harmful effects on the respiratory system and eyes.

When reacted, the resulting materials have good chemical durability and low vapour pressures, making them safer to handle.

The low melting points of these glasses make them ideal for study using our refractometer.

Refractive Indices of Molten and Glassy As-S-I Samples

The refractive index of each sample was measured at varying temperatures over the wavelength range 1.8 μm to 0.6 μm, using the apparatus and methods described in Chapters 2 and 3.

Samples were observed to have low softening points and, on heating, ran down into the cell at temperatures ranging from 150 to 21 deg. C. Composition E flowed at room temperature; luckily the rate at which it ran down was slow enough to still allow alignment of the light beam. Whenever possible, measurements were also made as the sample cooled down to room temperature, however in some samples a cut-off in transmission was observed as the sample cooled.

The wavelength dependence of the refractive index, for each of the seven sample compositions is shown in Figures 5.08 (a) to 5.14 (a).

The optical absorption, by a thin sample layer, was measured using the two stage method described in Chapter 2. The wavelength range is limited by the sensitivity of the detecting silicon photodiode to measurements below 1.2 μm. This was quite adequate to study the shift in absorption edge with temperature. The optical absorption coefficients for each sample, and their exponential energy dependence are illustrated in Figures 5.08 (b) to 5.14 (b).

SAMPLE A

At.% Composition 24% As
57% S
19% I

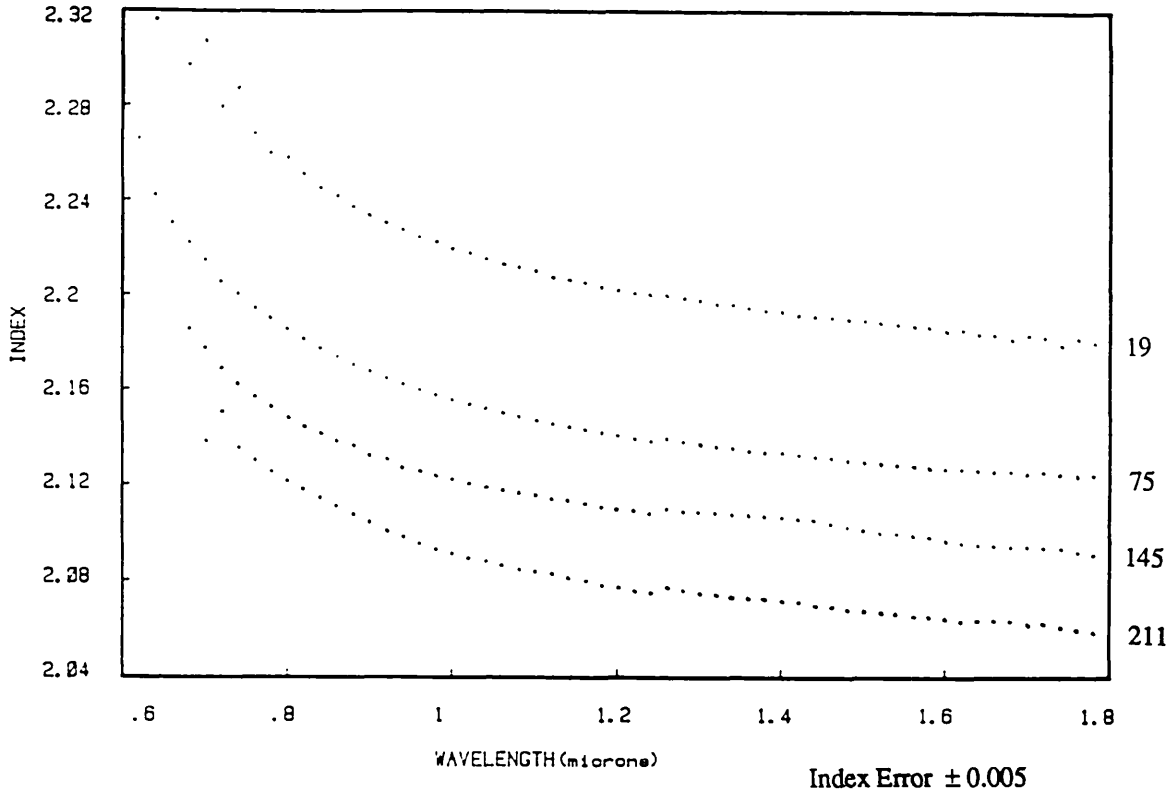


Figure 5.08(a): Refractive Index measurements.

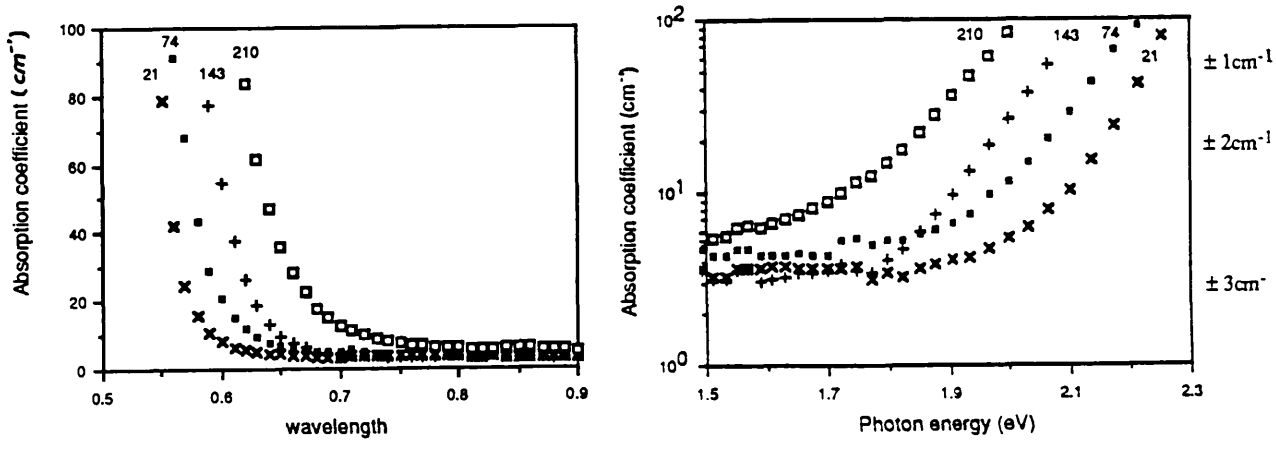


Figure 5.08(b): Optical absorption coefficients and their exponential energy dependence.

SAMPLE B

At.% Composition 22% As
52% S
24% I

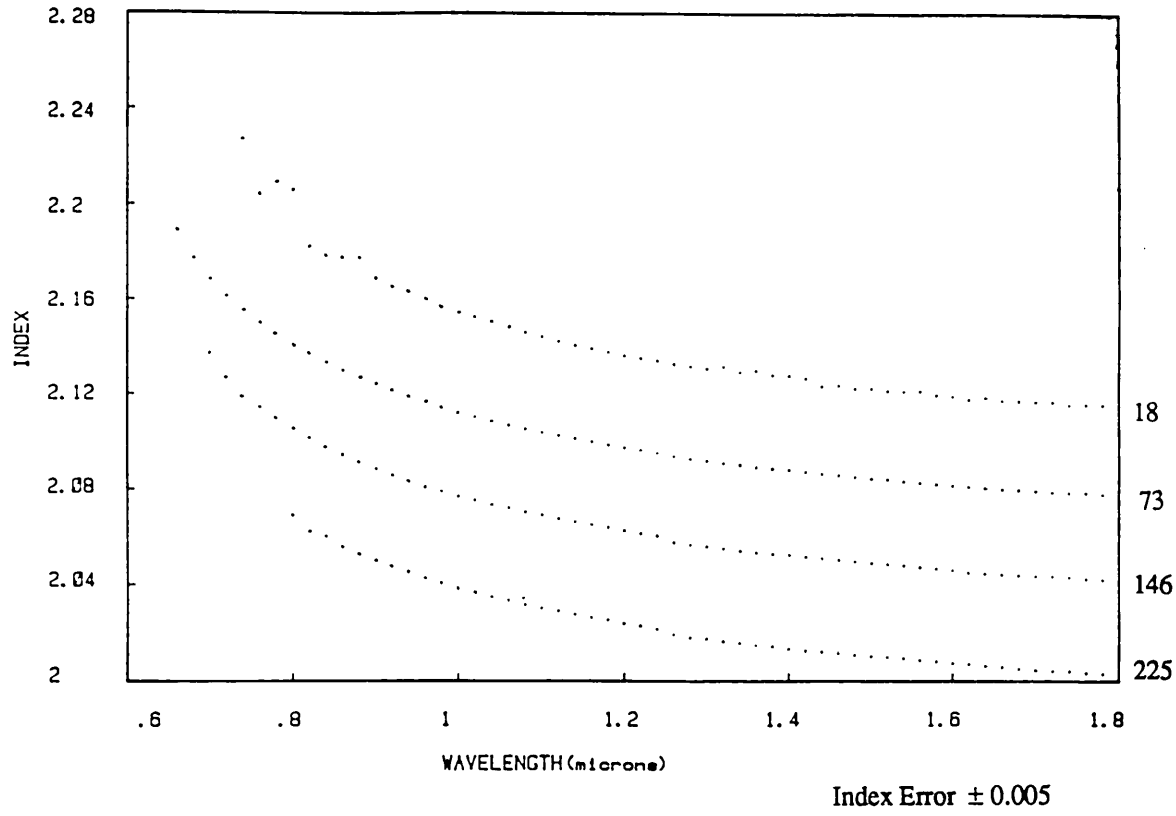


Figure 5.09(a): Refractive Index measurements.

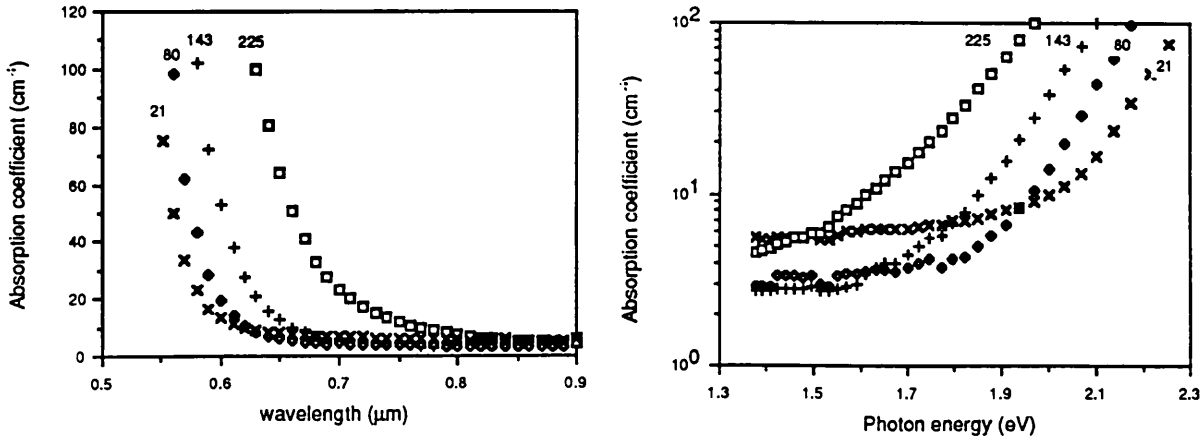


Figure 5.09(b): Optical absorption coefficients and their exponential energy dependence.

SAMPLE C

At.% Composition 33% As
50% S
17% I

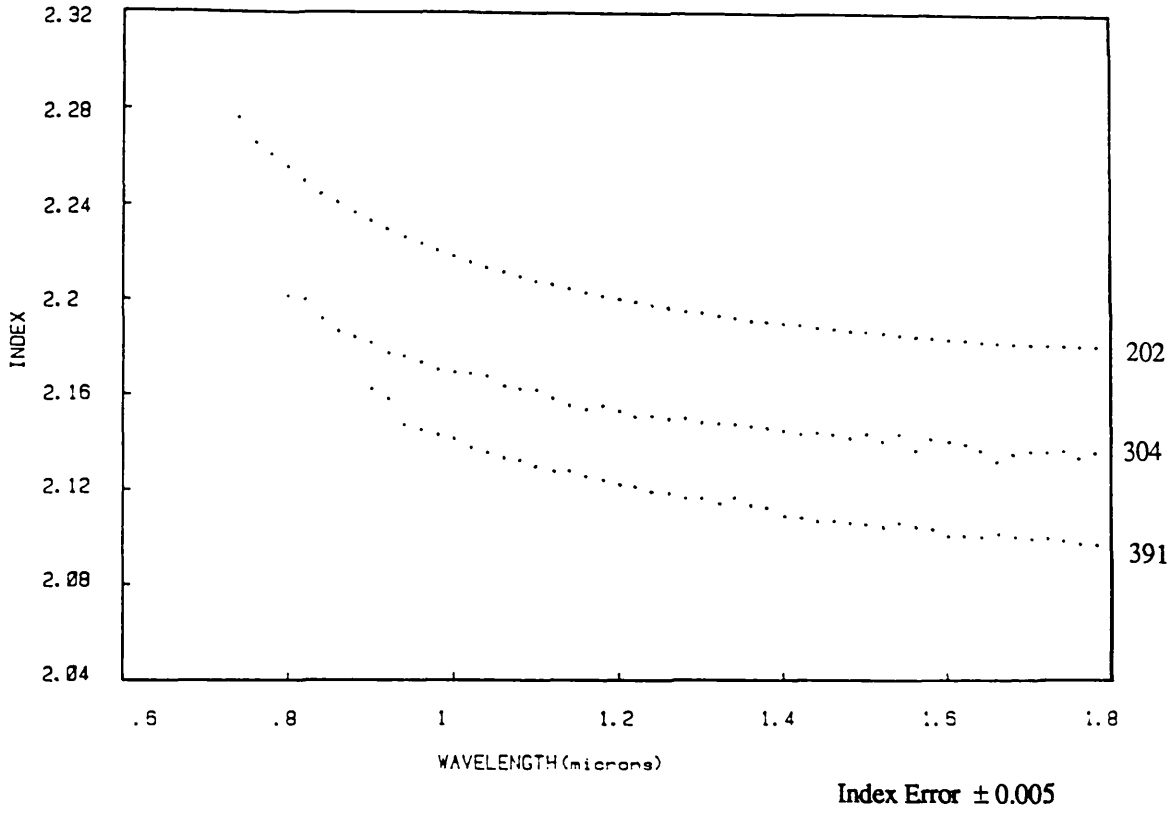


Figure 5.10(a): Refractive Index measurements.

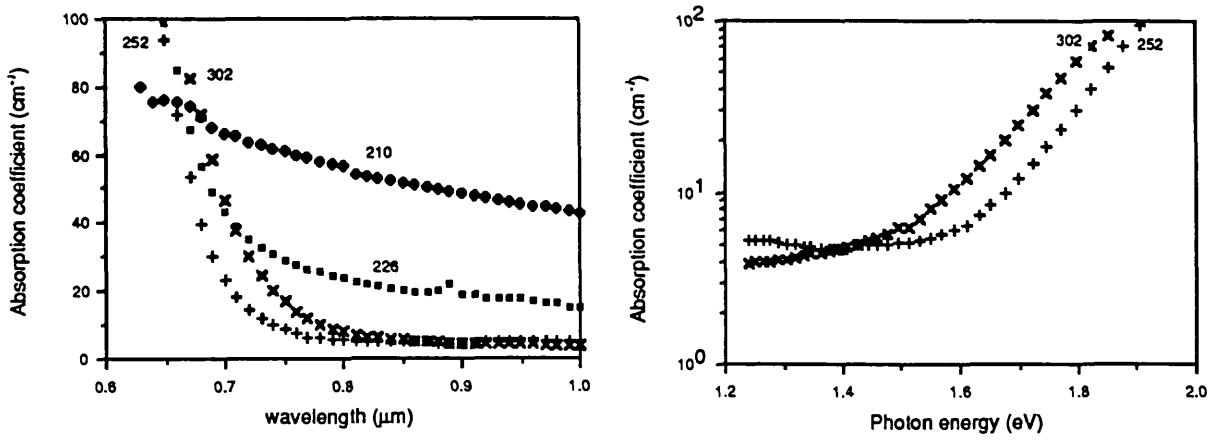


Figure 5.10(b): Optical absorption coefficients and their exponential energy dependence.

SAMPLE D

At.% Composition 26% As
61% S
13% I

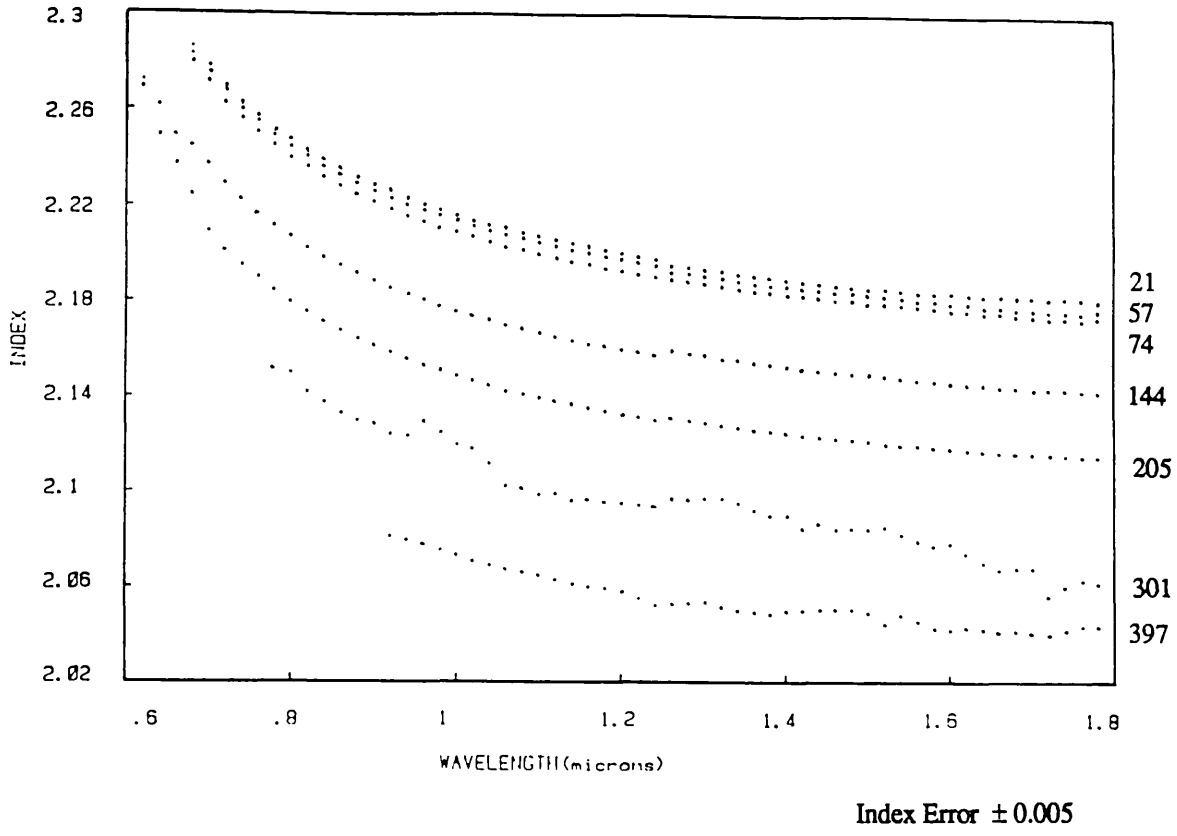


Figure 5.11(a): Refractive Index measurements.

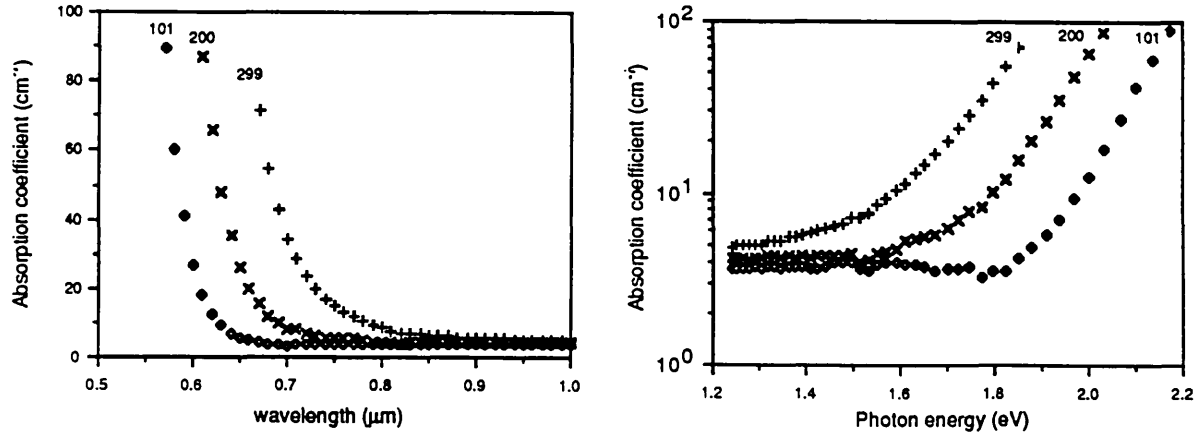


Figure 5.11(b): Optical absorption coefficients and their exponential energy dependence.

SAMPLE E

At.% Composition 16% As
63% S
21% I

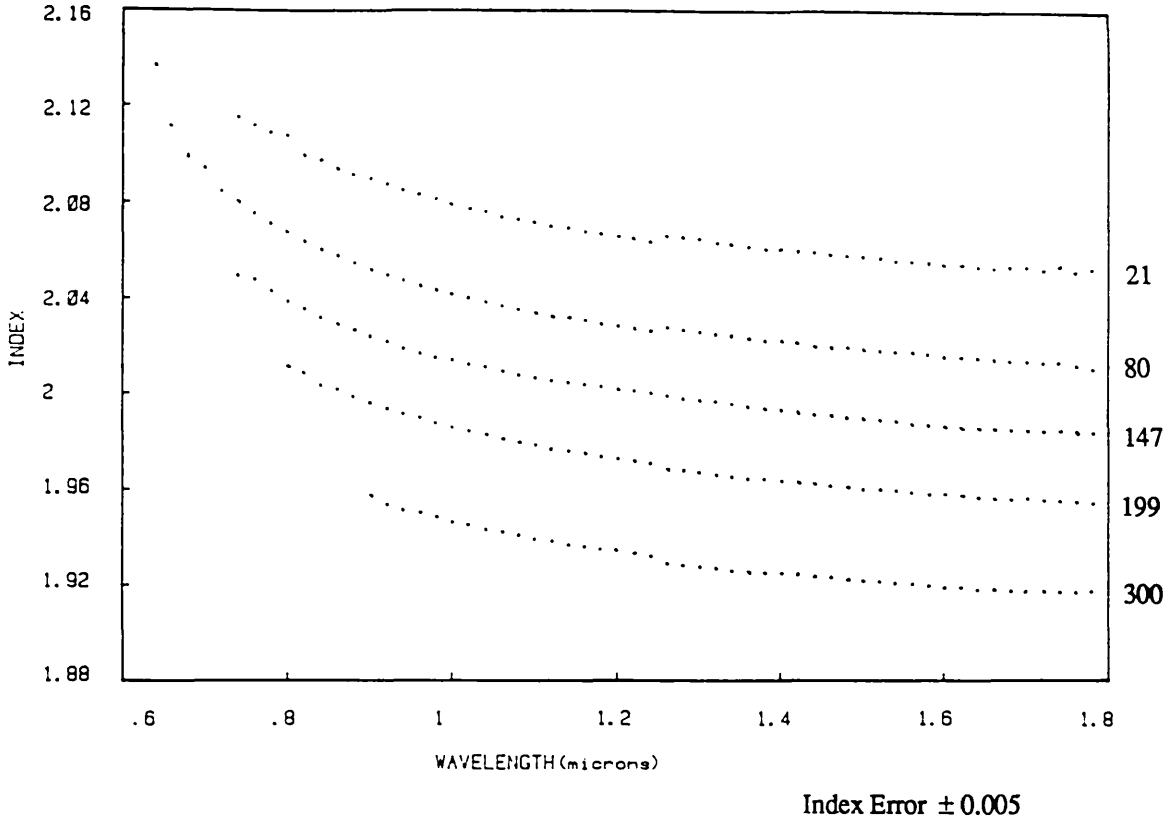


Figure 5.12(a): Refractive Index measurements.

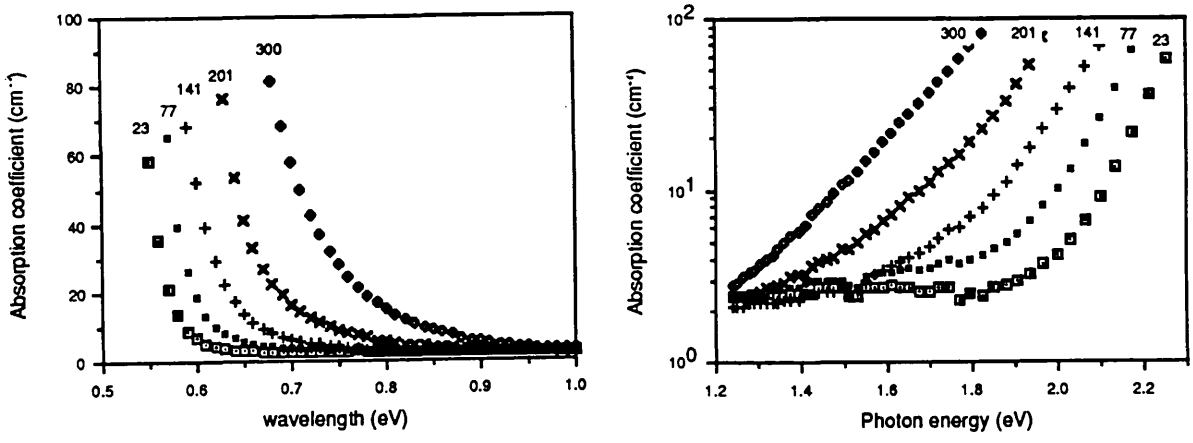


Figure 5.12(b): Optical absorption coefficients and their exponential energy dependence.

SAMPLE F

At.% Composition 18% As
67% S
15% I

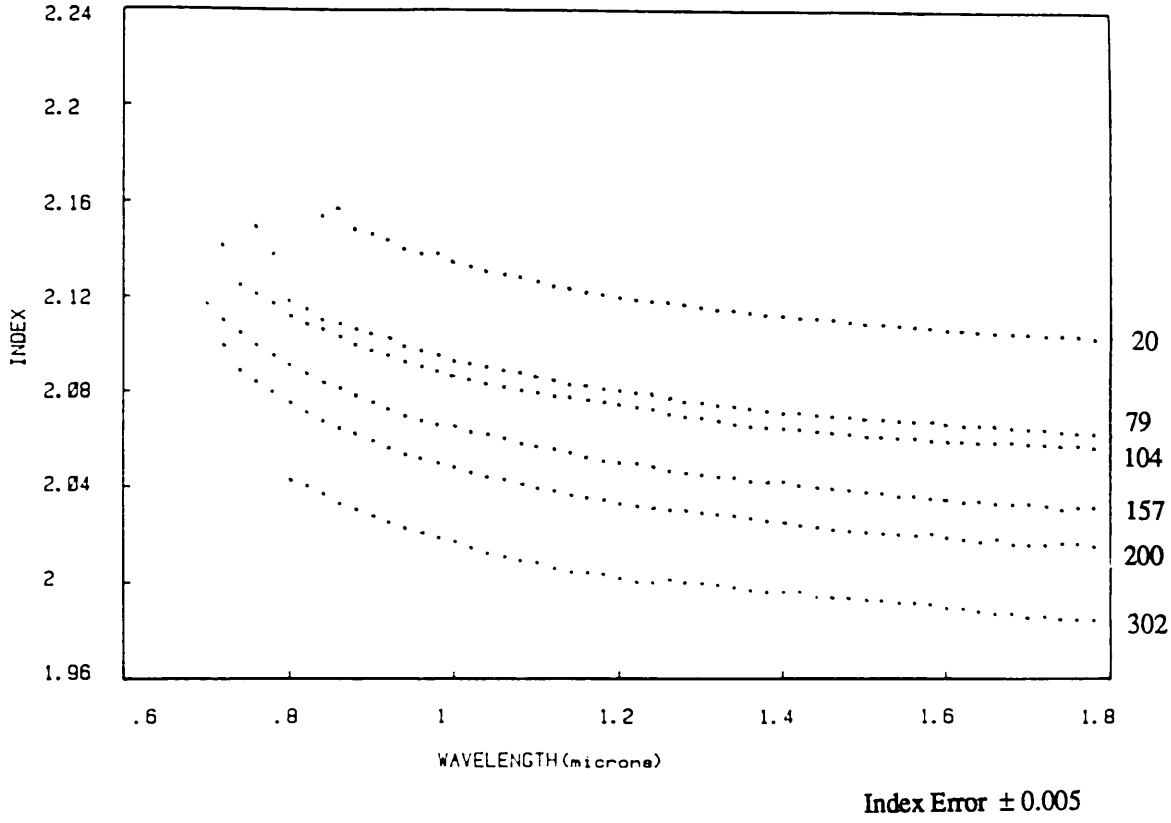


Figure 5.13(a): Refractive Index measurements.

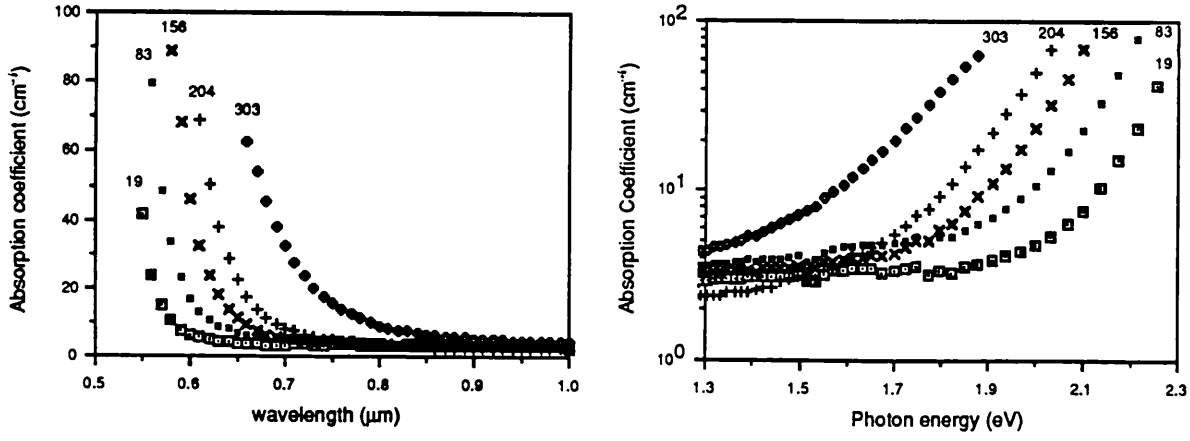


Figure 5.13(b): Optical absorption coefficients and their exponential energy dependence.

SAMPLE G

At.% Composition 32% As
43% S
25% I

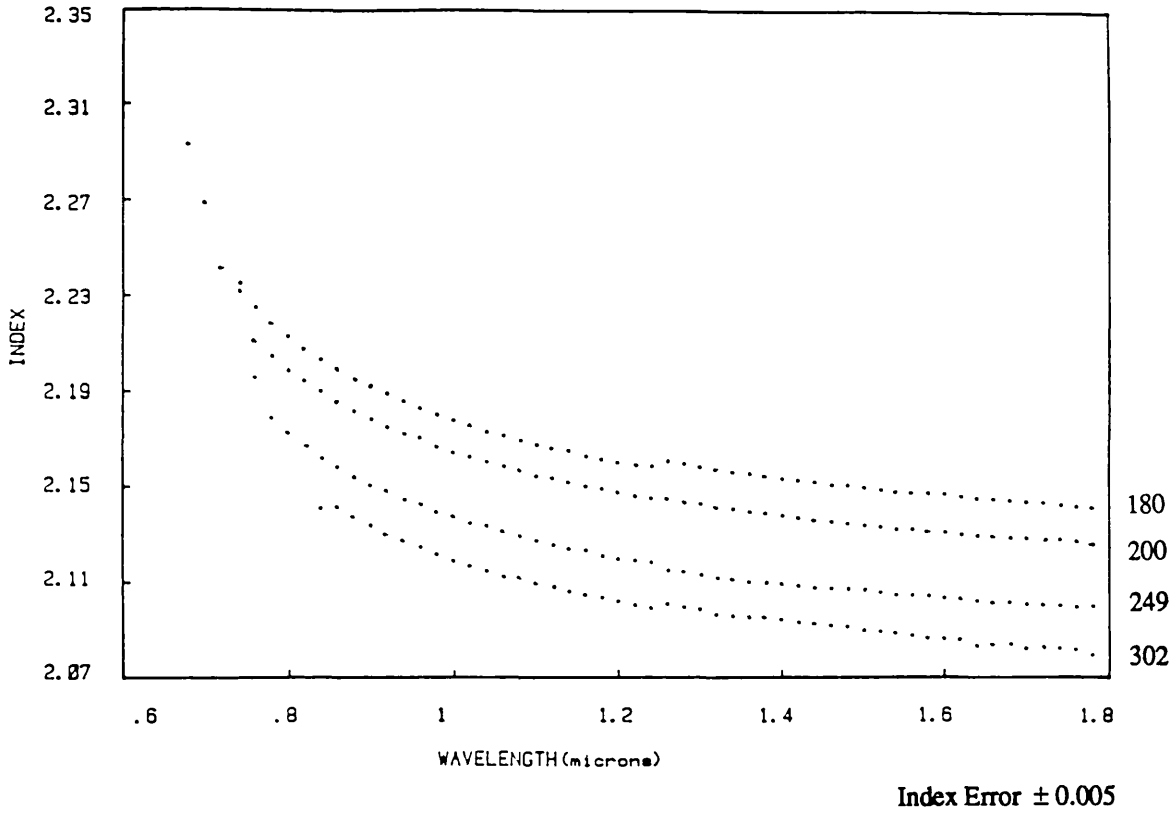


Figure 5.14(a): Refractive Index measurements.

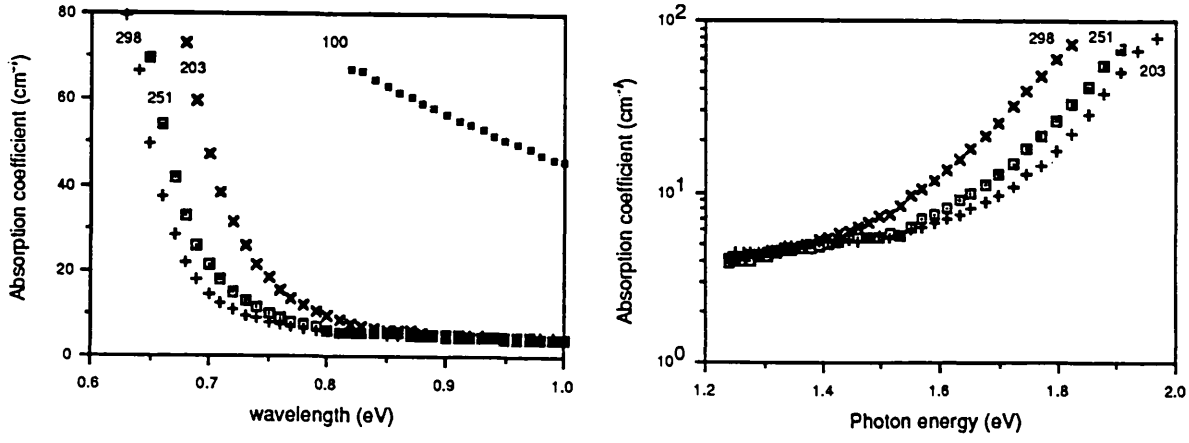


Figure 5.14(b): Optical absorption coefficients and their exponential energy dependence.

Discussion of Results

Table 1 presents the seven samples compositions labelled A to G in Figure 5.07, with their weight percent and equivalent atomic percent compositions. By comparing these compositions with the structural phase regions of Figure 5.05 we see that the sample distribution is in and around the chain structure region 4. No description of the structure in between regions was given by the studies of Gerasimenko et al (1977) and Koudelka et al (1983) but, along the As_2S_3 - AsI_3 section, viscosity measurements show a gradual transition from region 2 to region 4.

According to Mellor (1956) equiatomic As-S-I boils without evolution of iodine but with partial decomposition into arsenious triiodide and trisulphide. The fluctuations observed in the high temperature index measurements, of compositions C and D, may well be caused by such partial decomposition.

The temperature dependence of the seven sample compositions can be summarized by plotting the measured index at 1 μm against temperature, Figure 5.15. Each sample shows a linear change in index with temperature over most of its measured range. Below 70 deg. C. the data is less reliable due to thermal contraction causing the sample to pull away from the cell, which would effectively change the cell angle. From Figure 5.15 we can extract the refractive index of each sample at 200 deg. C. (measured at 1 μm). These indices may be plotted as a function of composition,

TABLE 1

Wt% to At% conversions for chosen samples

		As	S	I
SAMPLE A:	wt%	30	30	40
	at%	24	57	19
SAMPLE B:	wt%	25	25	50
	at%	22	52	26
SAMPLE C:	wt%	40	26	34
	at%	33	50	17
SAMPLE D:	wt%	35	35	30
	at%	26	61	13
SAMPLE E:	wt%	20	34	46
	at%	16	63	21
SAMPLE F:	wt%	26	40	34
	at%	18	67	15
SAMPLE G:	wt%	34	20	46
	at%	32	43	25

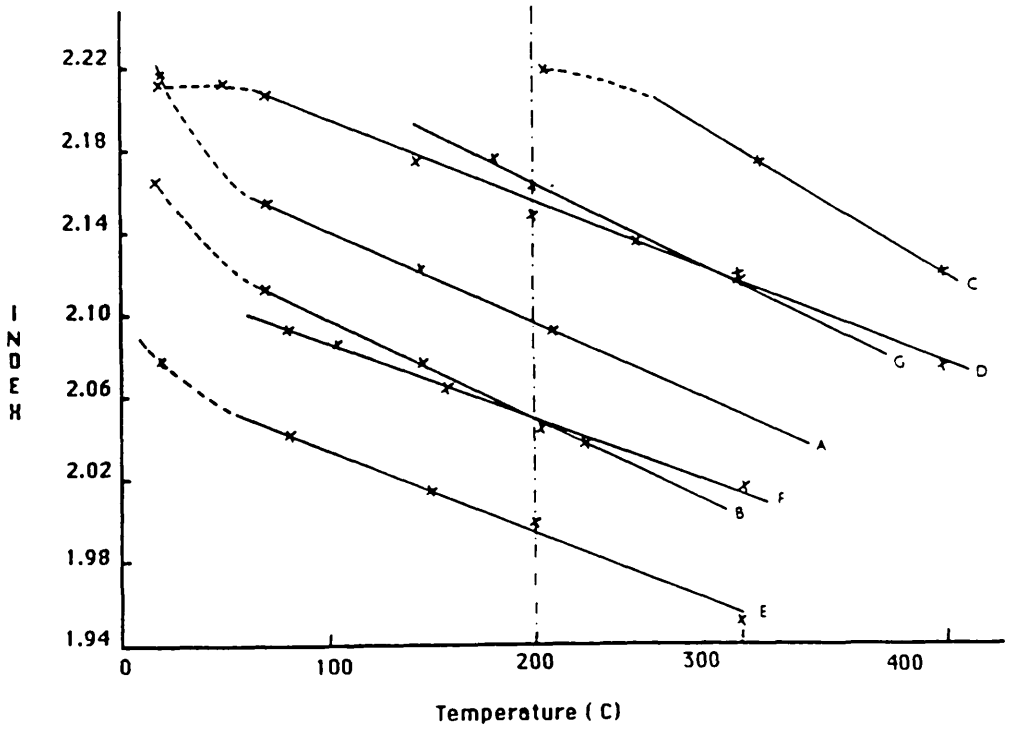


Figure 5.15: Summary of As-S-I results; refractive index at 1 μm plotted as a function of temperature.

(Index Error ±0.005)

Figure 5.16 to illustrate the change in index as we move around the glass forming region.

The cut-off in transmission detected in the refractive index measurements of samples C and G were again evident in their absorption measurements. The absorption measurements of sample C, Figure 5.10 (b), clearly shows that this cut-off is not due to a sudden shift in the absorption edge, but results from a rapid increase in absorption at all measured wavelengths. In the thin absorption cell these samples can also be observed to become opaque around 200 deg. C,, this cut-off is most likely due to a phase change and as such its temperature dependence will be subject to the sample's thermal history and its cooling rate. To investigate the dependence on cooling rate we varied the cooling rate of sample C. This was achieved by removing the thermal insulating shells from the heating block. Figure 5.16b shows the measured refractive index (at 1.4 μm) as sample C was cooled with and without thermal insulation. The cut-off temperature was *sup*pressed down to 70 deg. C., which implied that room temperature glasses could be obtained by quench cooling the melts.

Dispersion of As - S - I Glasses

Figures 5.17 to 5.23 show that the refractive index data for each sample composition may be fitted to the single oscillator dispersion equation of chapter 1 (equation 1.34).

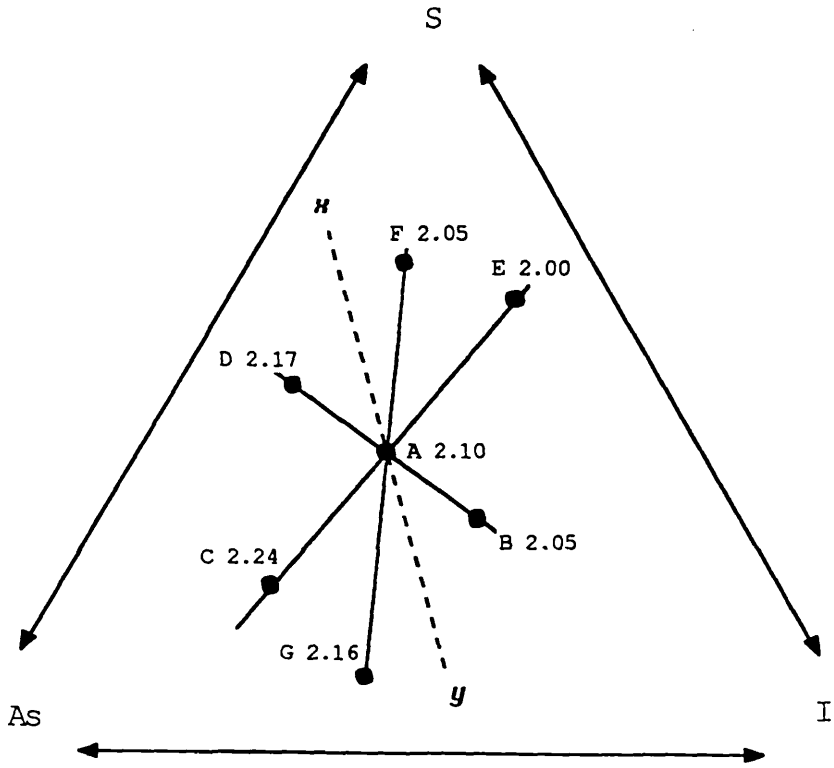


Figure 5.16: The measured index for 1μm at 200°C, plotted as a function of composition. The line 'xy' represents the direction of composition change for which the index is invariant.

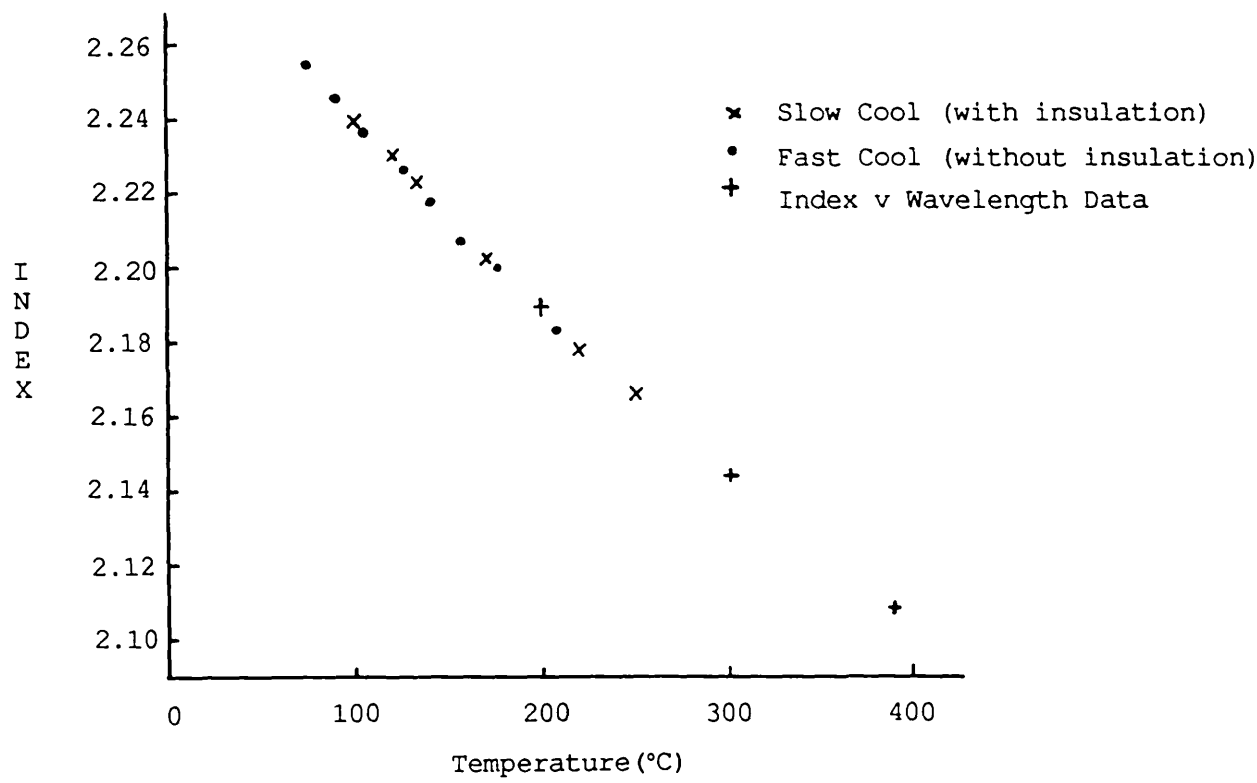
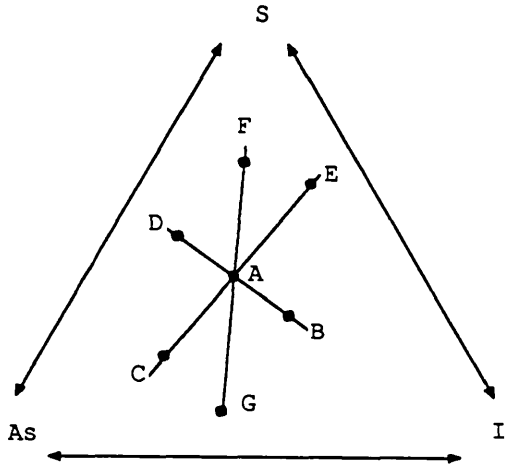


Figure 5.16(b): Measured refractive index as sample C is cooled with and without thermal insulation.



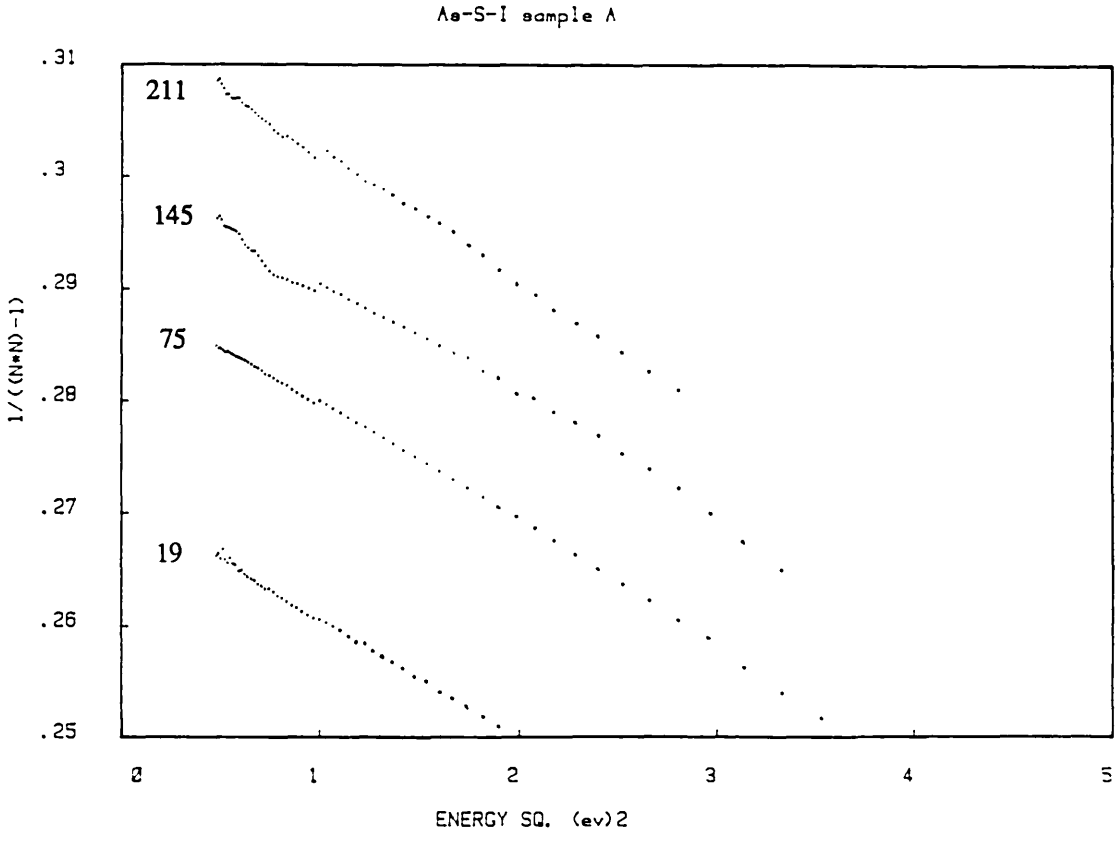


FIGURE 5.17: Dispersion of the refractive index for sample A.

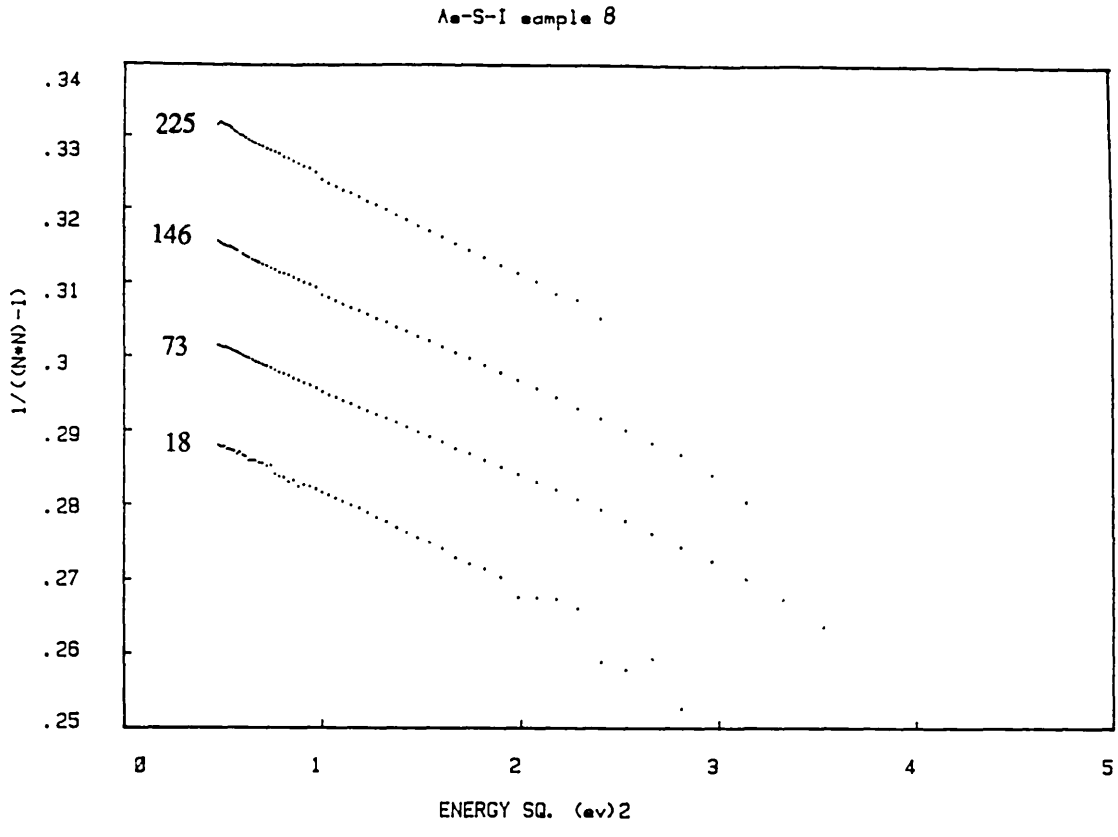


FIGURE 5.18: Dispersion of the refractive index for sample B.

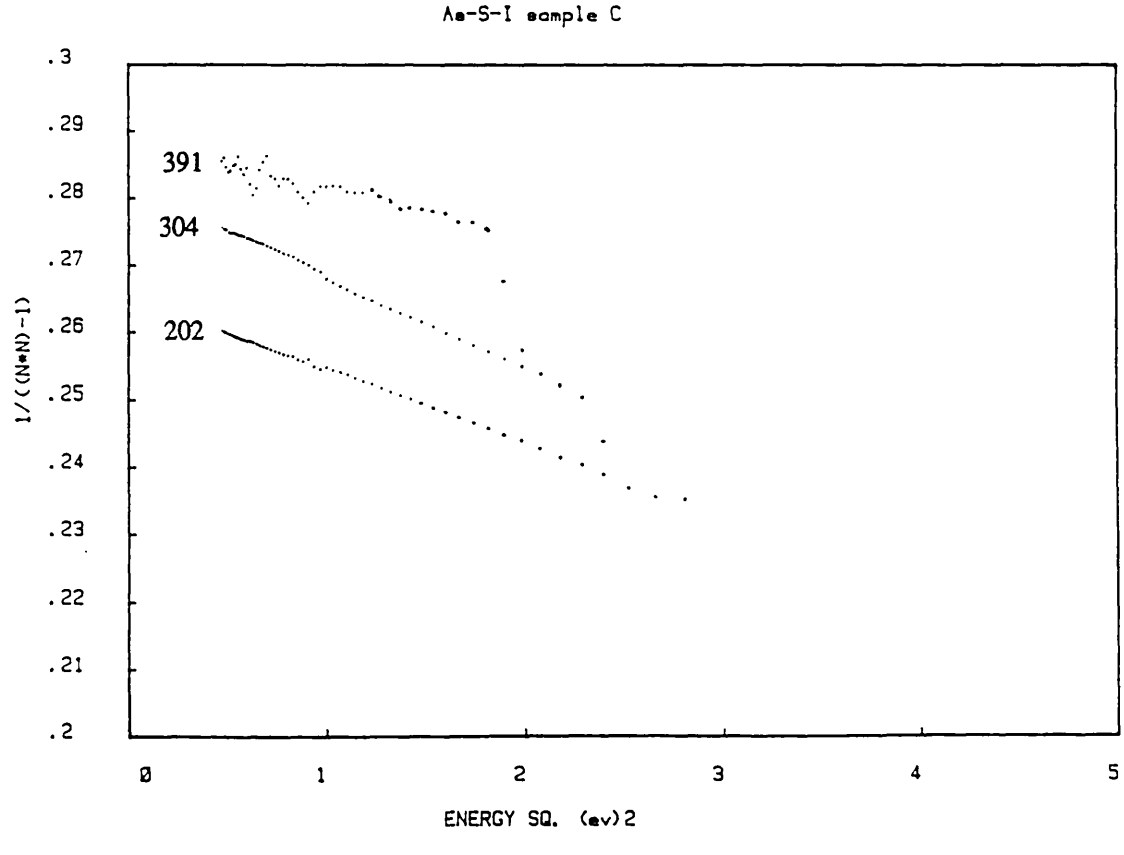


FIGURE 5.19: Dispersion of the refractive index for sample C.

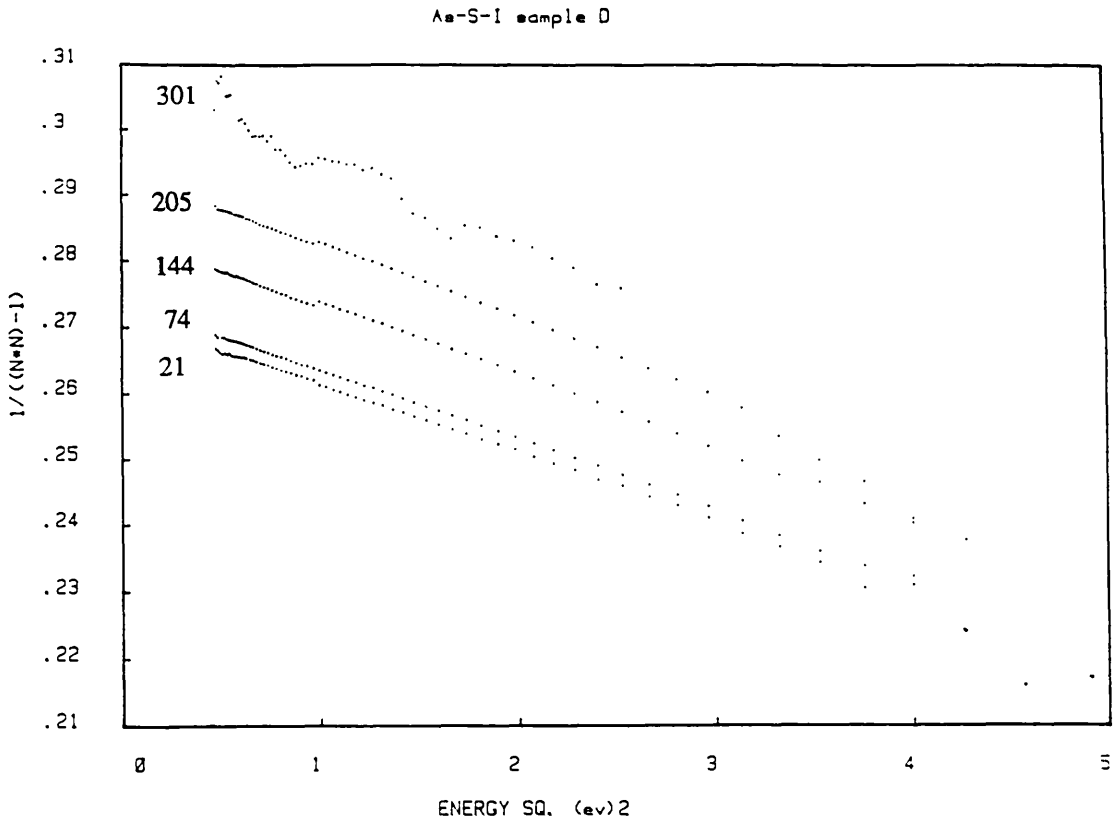


FIGURE 5.20: Dispersion of the refractive index for sample D.

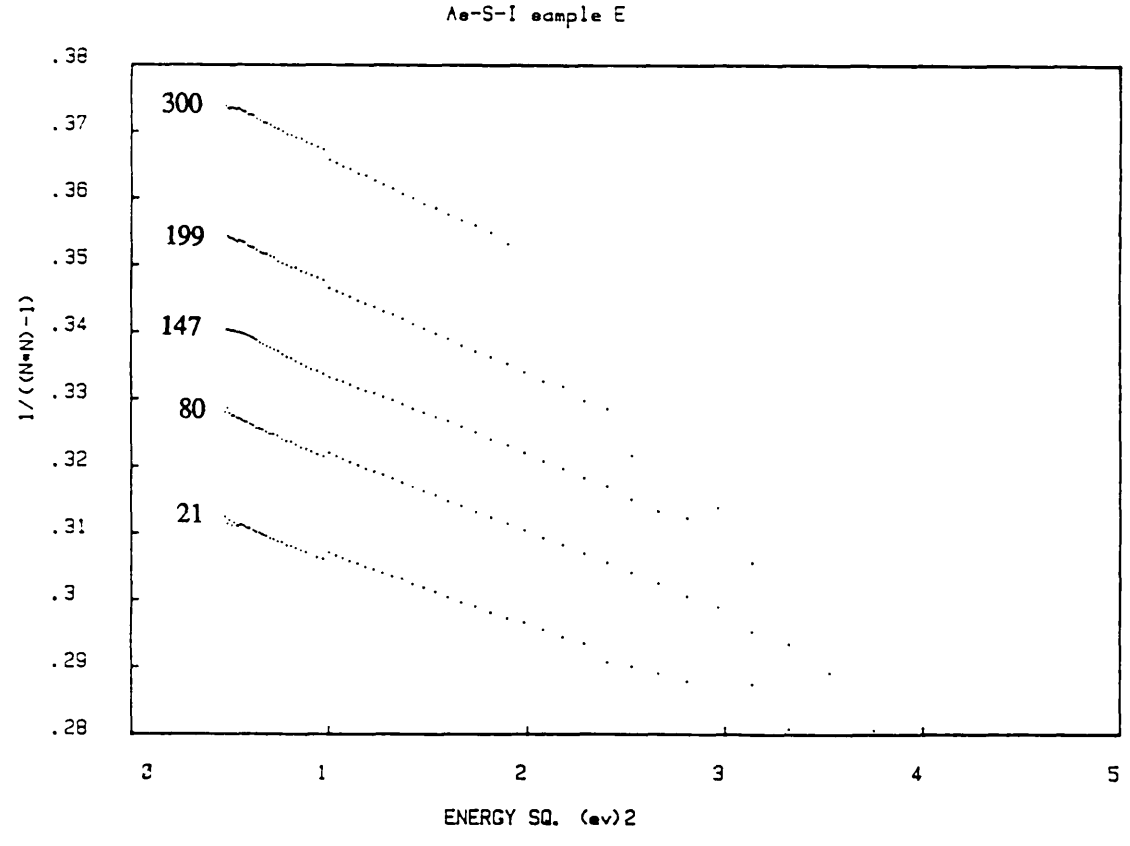


FIGURE 5.21: Dispersion of the refractive index for sample E.

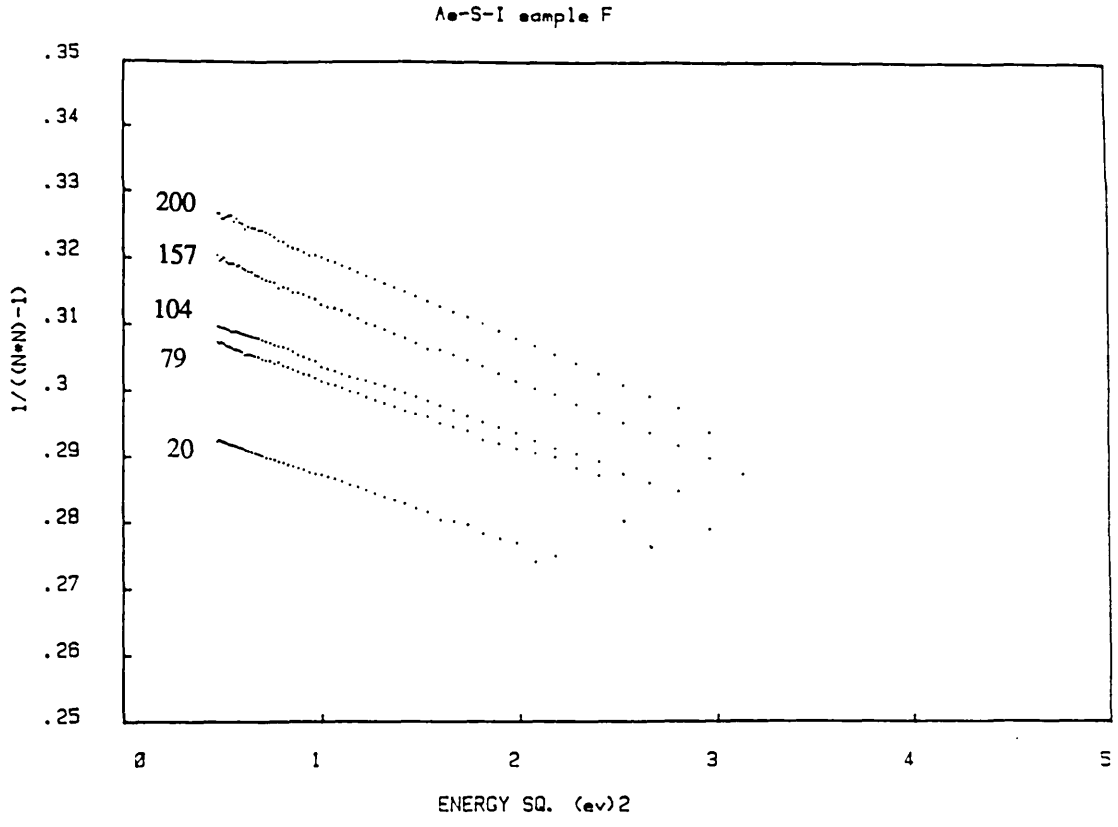


FIGURE 5.22: Dispersion of the refractive index for sample F.

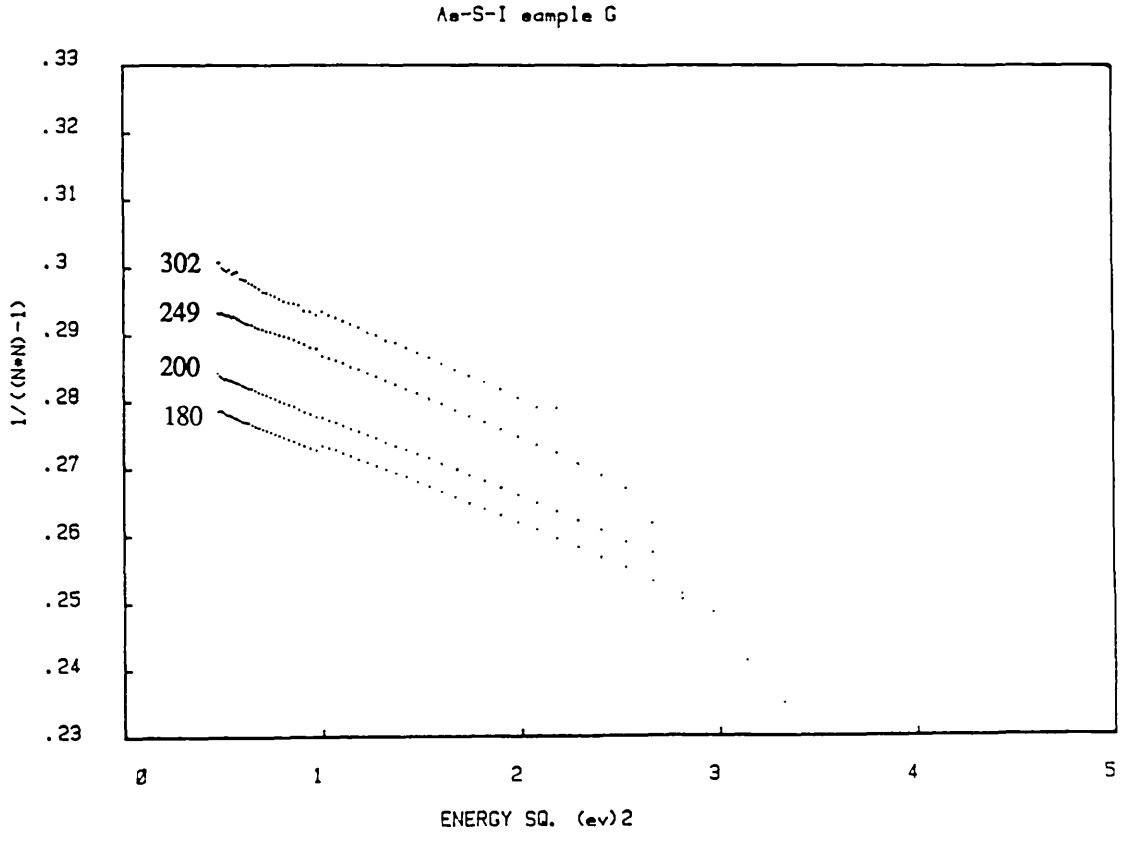


FIGURE 5.23: Dispersion of the refractive index for sample G.

The departure from linearity of samples C and D, at high temperatures, are obviously due to index fluctuations at these temperatures. Each set of measurements show a distinct jump at energy squared values of 1 eV^2 ; this simply corresponds to a slight displacement of the beam as a new filter is stepped in.

By extrapolating the straight line data of Figures 5.17 to 5.23 we can obtain the zero frequency refractive indices, n*(0) which are illustrated in Figure 5.24. Since n*(0) is temperature dependent we can either extrapolate or interpolate to find the value of n*(0) for each sample at 200 deg. C. This value can then be used to plot n*(0) as a function of composition, Figure 5.25. As we would expect, the changes in n*(0) with composition are consistent with the refractive index variations of Figure 5.16.

Refering back to equation 1.34 which was used to plot figures 5.17 to 5.23, we can extract the two energy parameters, E_d and E_o, from the gradient and ordinate intercept for each of the straight lines. Figure 5.26 shows the values of E_d, for each sample composition, which are seen to be temperature dependent. This temperature dependence is due to the changing sample density and as such is expected to be constant over the range of compositions studied. The values of E_o, figure 5.27, show no significant temperature dependance but are seen to decrease with increasing arsenic concentration.

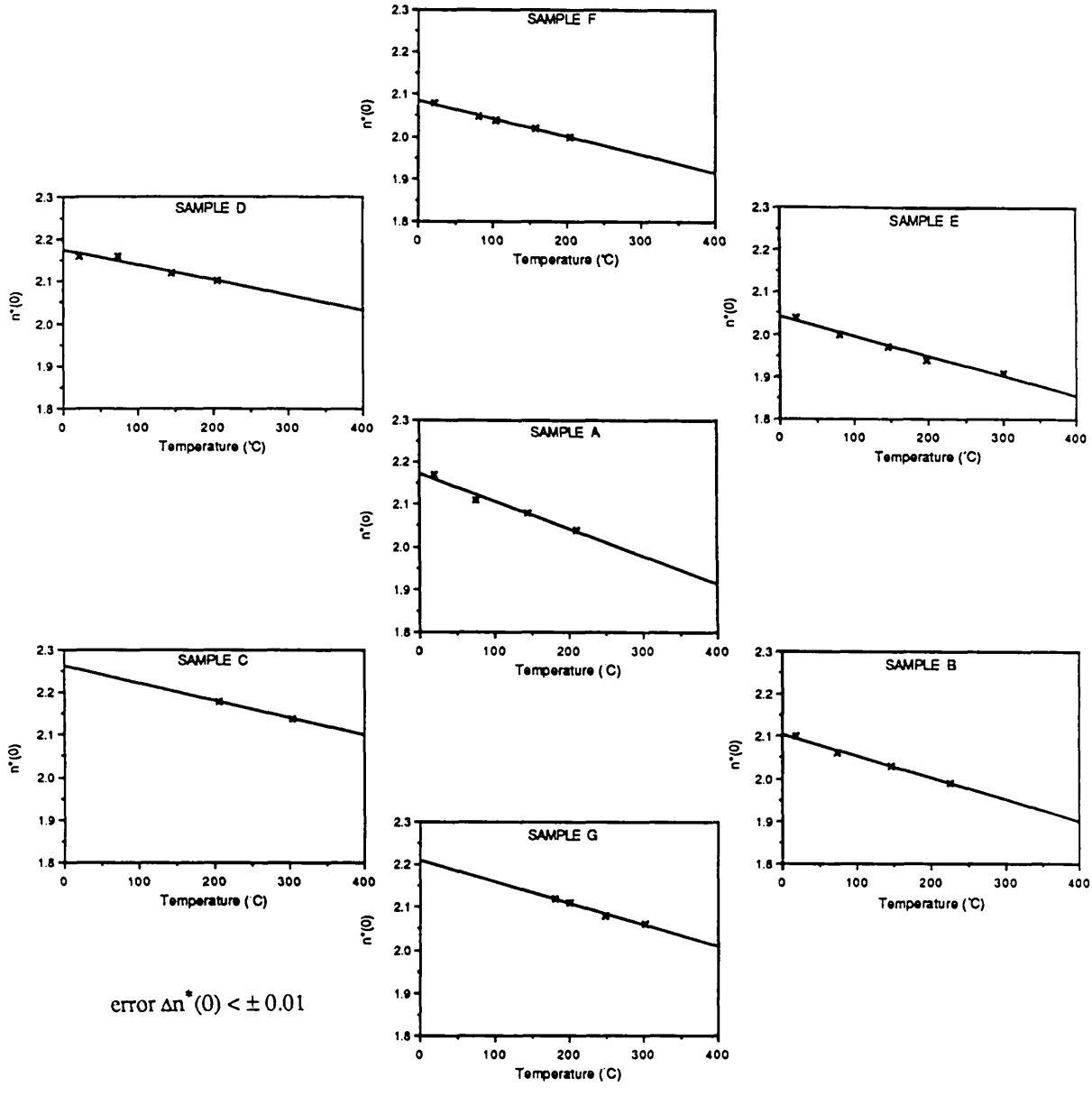


Figure 5.24: Zero frequency refractive index for samples A - G.

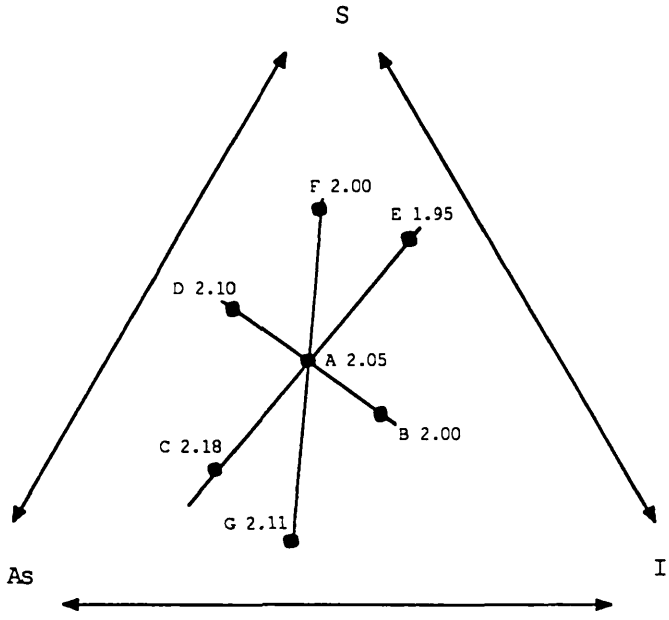


Figure 5.25: Compositional dependence of the zero frequency refractive index.

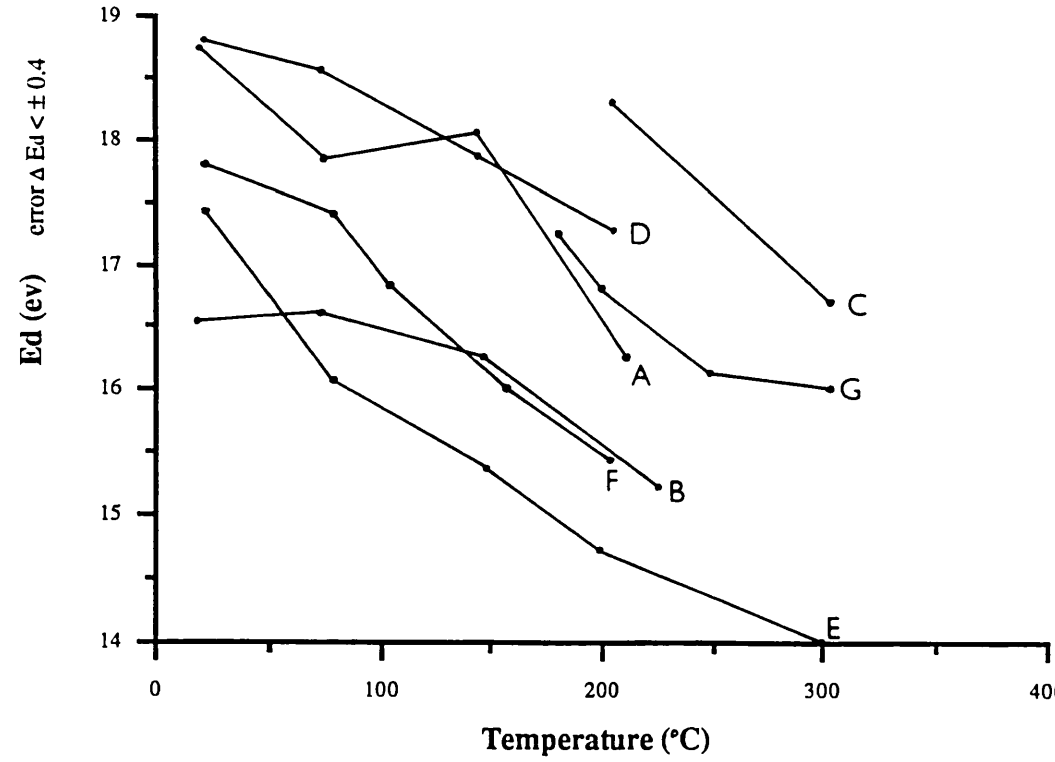


Figure 5.26: Calculated transition strength dispersion parameter, E_d, for As-S-I samples.

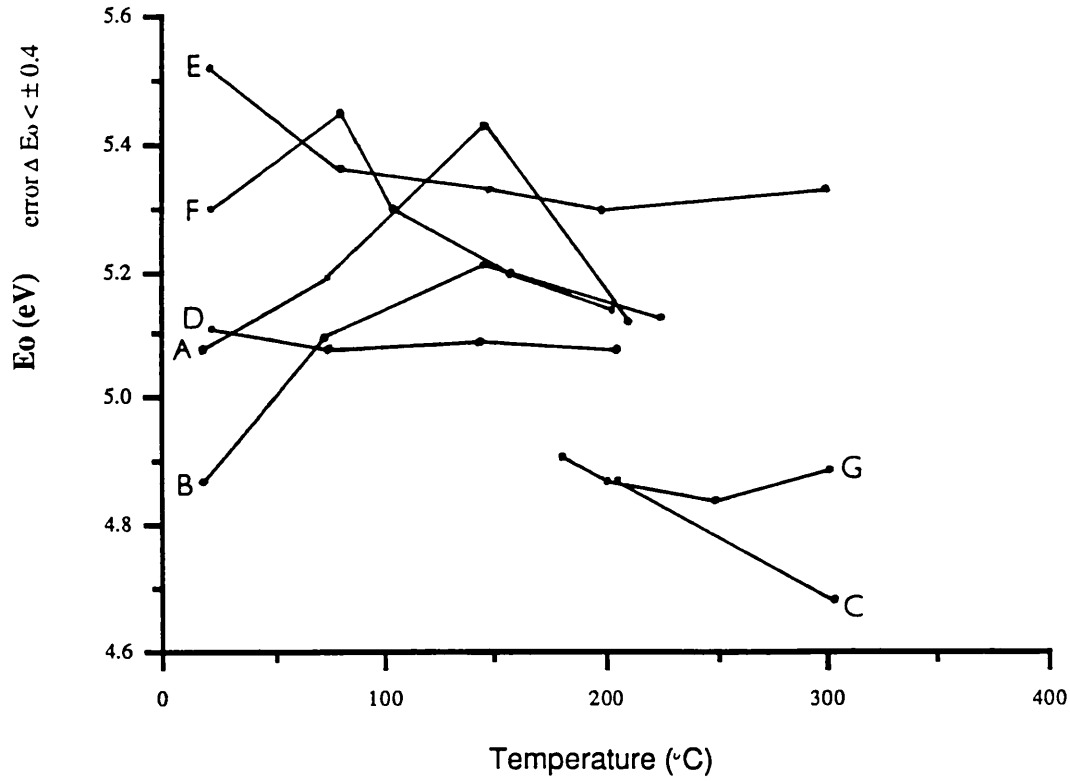


Figure 5.27: Calculated average energy gap dispersion parameter, E_o.

Sample Densities

The refractive index varies directly with the samples density, as is illustrated by its temperature dependence. Further insight into the index variations can be gained by studying the densities of each sample.

Several methods of measuring the sample density were considered and we chose to use the traditional technique using weighing bottles:-

i) Weigh empty bottle wt. B.

ii) Fill bottle with calibrating liquid of known density, L, and weigh wt. B + L (Calculate vol L = Vol B).

iii) Fill bottle with measuring liquid and weigh wt. B + L' (Calculate L').

iv) Weigh sample wt. S.

v) Fill bottle with sample and measuring liquid wt. B + S + L" (Calculate vol S and knowing wt. S we obtain the sample density S).

The sample being measured, had to be reclaimed from used optical cells so I only had 1.5 grams of each sample. The smallest commercially available weighing bottles are 10 ml, which are difficult to handle yet rather large compared to the volume of sample being measured. Hence despite using an accurate balance and all the care taken, the results still suffer quite large errors, $\pm$ 0.05 g cm^{-3} .

Water was used to calibrate the bottles but, because some samples are moisture sensitive, paraffin was used as the room temperature measuring liquid. Measurements were made at temperatures of 50, 100 and 150 deg C using diffusion pump oil as the measuring liquid, the maximum temperature being limited by the sample beginning to react with the oil. Table 2 presents the sample densities and the observed sample state at room temperature.

Constant Atomic Number Density

By assuming that the measured sample density is directly proportional to the ratio of elements in its composition we can calculate the number of atoms of each element per unit volume. The sum of these give the atomic number density. Supposing that this atomic number density is constant as the composition changes, then we can calculate the density changes as the composition alters. From our measured densities, at room temperature, the atomic number densities are found to show very little variation; thus confirming our supposition. Using the averaged number density, we can now set up a constant atomic number density model which predicts the density of any sample composition. The measured sample densities are shown as a function of composition, in Figure 5.28 together with the values predicted by our model. Our measurements correspond very well to the model's predictions. This shows that there is no

TABLE 2

SAMPLE DENSITY

	A	B	C	D	E	F	G
Condition at room temp.	Solid Brittle	Sticky Soft	Solid Brittle	Sticky Soft	Sticky Soft	Sticky Brittle	Solid Brittle
21	3.22	3.46	3.08	3.37	2.99	2.90	3.60
50	3.08	3.15	3.10	2.93	2.83	2.70	3.47
100	2.97	3.09	3.00	2.82	2.74	2.62	3.40
150	2.90	2.94	2.87	2.63	2.66	2.56	3.24

p error ± 0.05 g/cm^3

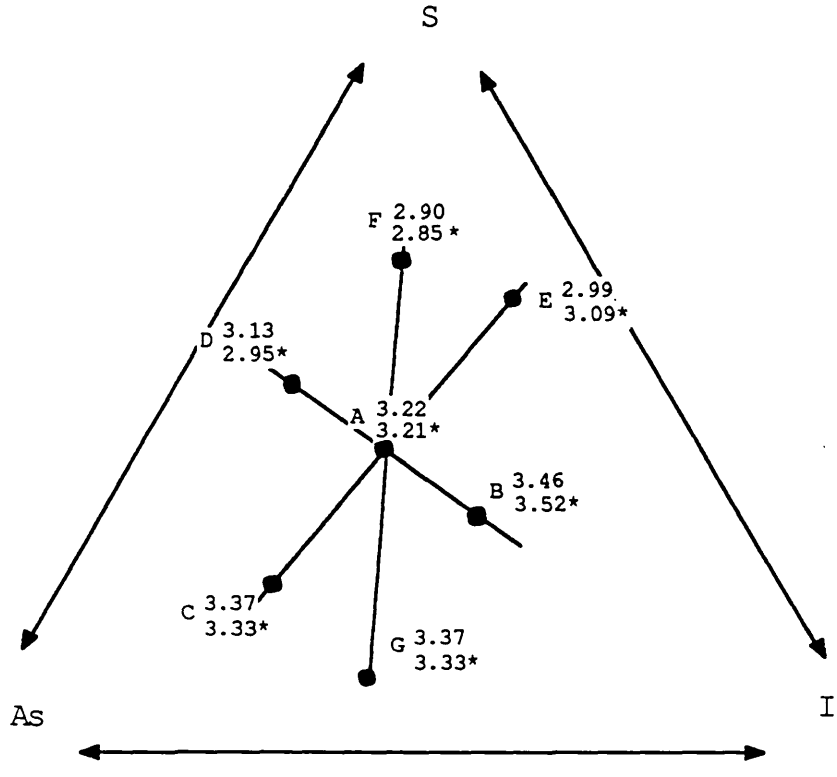


Figure 5.28: Comparison of the measured density with the predictions (asterisked) of a constant atomic number density model. Uncertainties are ± 0.05 gcm^{-3}

significant structural change over the range of compositions, and supports the suggestion that the structural change between regions is gradual.

From the density variation as a function of temperature we can estimate the coefficient of cubical expansion, for these samples, as 80 $\pm$ 10 x 10^{-5} / deg C which is comparable to that of many liquids. This expansion coefficient corresponds to a total volume change, over 200 deg. C., of ~ 20%. Such large volume changes support the suggestion that the low temperature index measurements were affected by the sample pulling away from the prism windows.

Equiatomic As - S - I

Most research has been done on the equiatomic composition which lies outside the range of compositions that we have studied. To make any comparisons with the literature we need to predict the results of an equiatomic composition:-

Index: If we recall that Figure 5.16 showed from the measured index for 1 μm at 200 deg. C., that the index is invariant for compositional changes in the direction xy. Figure 5.29 illustrates the measured equiatomic composition projected onto a line, st, perpendicular to xy. The index variation can now be plotted as a function of position along st, Figure 5.30, and the projection of the equiatomic composition, Q, gives the 1 μm index at 200 deg. C. as 2.13.

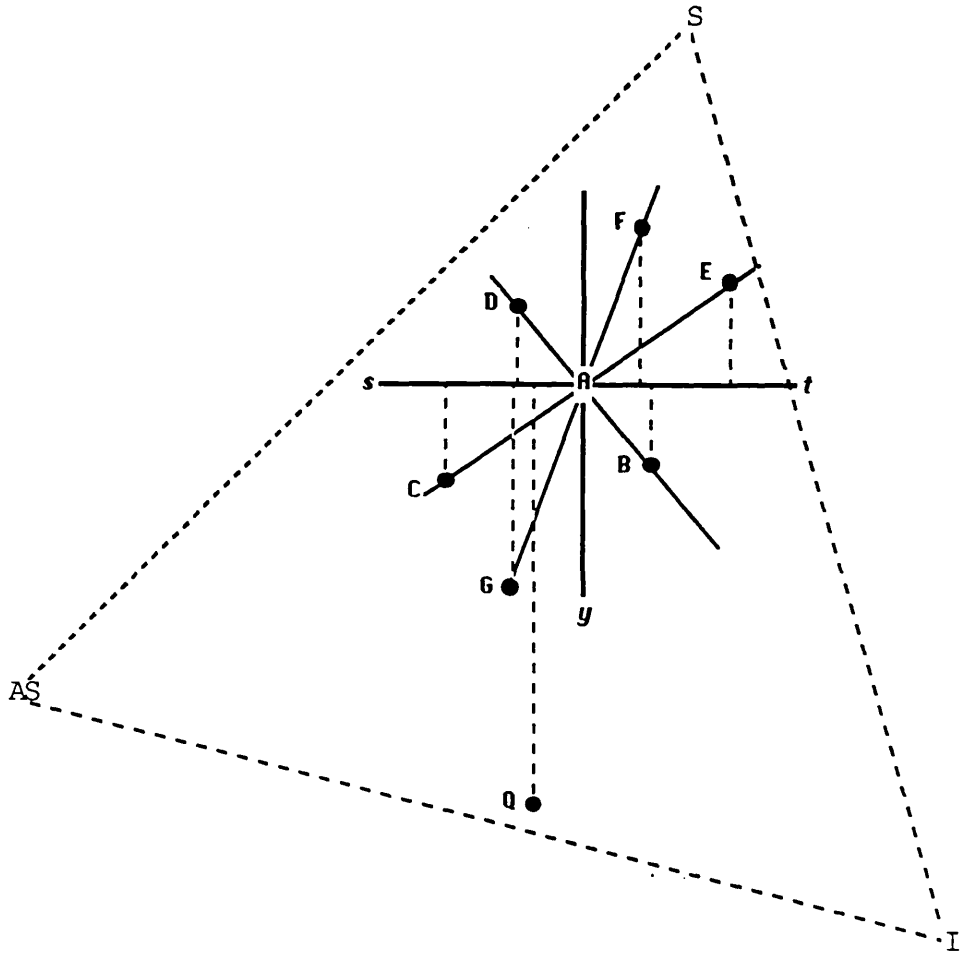


Figure 5.29: Projection of the measured sample (and the equiatomic composition) onto the line 'st'.This line represents the maximum rate of index change with composition.'

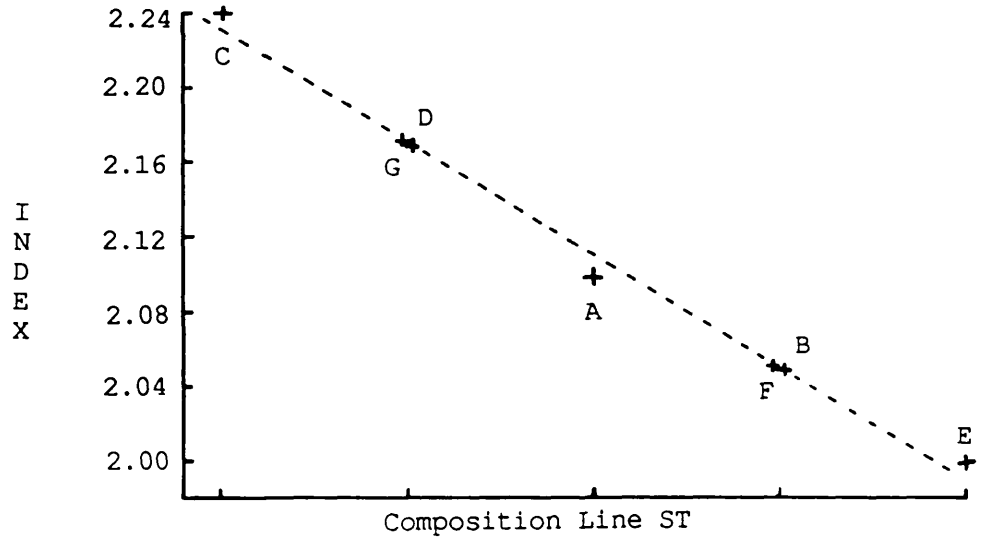


Figure5.30: Index variation plotted a function of position on the composition line 'ST'.

Using the index/temperature gradient of sample A, we can estimate that the room temperature refractive index would be 2.23 ±0.01.Following a similar procedure for the zero frequency refractive index we can estimate n*(0) for the equiatomic composition as 2.20±0.02

Density: Since the sample compositions studied are consistent with the constant atomic number density model we can extrapolate this model to predict the equiatomic density. Doing this, we obtain a density of 4.1±0.1 g/cm^{-3}

Absorption Edge: The onset of absorption, at room temperature, occurs in the range 0.66 μm to 0.69 μm, these values being taken as the wavelength at which the absorption coefficient rises to 20 cm^{-1} . As we reduce the sulphur content in moving from composition G to Q, we would expect a small absorption edge shift to longer wavelengths giving an edge position of 0.70±0.02 μm

Summary of Useful References

A. N. Borets et al (1975)

This paper studies the absorption edge of As, S, I. As, Se, I and Sb, S, Br at temperatures of 5, 22, 77 and 290 deg. C. From the graph presented we would expect the room temperature absorption coefficient to be 20 cm^{-1} at 0.82 μm (For As-Se-I system = 20 cm^{-1} at 0.88 μm).

V. A. Zuban and A. N. Borets (1974)

Results for the long wavelength (1 μm to 20 μm) refractive index and % transmission for As-S-I and As-Se-I are presented. At 1 μm the indices for As-S-I and As-Se-I are 2.43 and 2.48 respectively. The 20% transmission at 1 μm corresponds to an absorption coefficient for As-S-I of 46 cm^{-1}.

A. N. Borets (1983)

This is the second paper by Borets in which he demonstrates the validity of an optic-refractometric correlation using results from numberous non-metallic substances including As-S-I and As-Se-I. From a table of results we can extract n = 2.26 (As-S-I) and 2.32 (As-Se-I) which presumably is the extrapolated zero frequency refractive index.

P. P. Seregin et al (1977)

Uses Mossbauer spectroscopy to analyse the crystal to glass transitions of some semiconducting compounds and concludes that there is no change in the local structure of As-S-I and As-Se-I during this transition. This paper also quotes the densities of these samples in the crystalline and glassy states.

	Crystalline	Glass
As-S-I	4.36	3.91
As-Se-I	4.78	4.52

The results quoted in these references, and my extrapolated results for the equiatomic composition are presented in Table 3. With the exception of the long wavelength measurements of Zuban and Borets 1974, the refractive index and density predictions seem consistent with the literature. The refractive index values of Zuban and Borets are significantly higher but this would be explained by the high absorption edge at 1 μm. An absorption edge at this long a wavelength is itself inconsistent with other observations, and results.

TABLE 3

SOURCE	n	n*(0)	edge /μm	ρ g cm^{-3}
EXPERIMENTAL RESULTS	2.25 ±0.02	2.15 ±0.04	0.7 ±0.1	4.13 ±0.05
Borets et al (1975)	___	___	0.82	___
Zuban & Borets (1974)	2.43	___	0.97	___
Seregin et al (1977)	___	___	___	4.36
Borets (1983)	___	2.26	___	3.98

SECTION 2: ARSENIC-SELENIUM-IODINE SYSTEM

Structure and Properties of As-Se-I System

The substitution of selenium for sulphur in these ternary systems has several important and useful effects. The viscosity of the melts is reduced and the absorption edge shifts towards the infrared, making these glasses opaque in the visible. Due to the increased electron density, the refractive index will be higher than in equivalent As-S-I compositions. Once again there is an extensive region of low melting point glass formation; however, according to Kniep and Reski (1981), there is an increased tendency for crystallisation (compared with As-S-I).

The structure of glassy and molten As Se I was first investigated by Poltavtseu (1975). Using X-ray diffraction on stoichiometric As S I and As Se I samples, the structure of both were shown to consist of twisted chains (recall Figure 5.04). The structure and chemical stability of the As-Se-I system was studied by Khiminets et al (1978). Based on the findings of vibrational spectroscopy the glass forming region has been shown to have subregions, Figure 5.31, within which the chemical structure of the glass varies:-

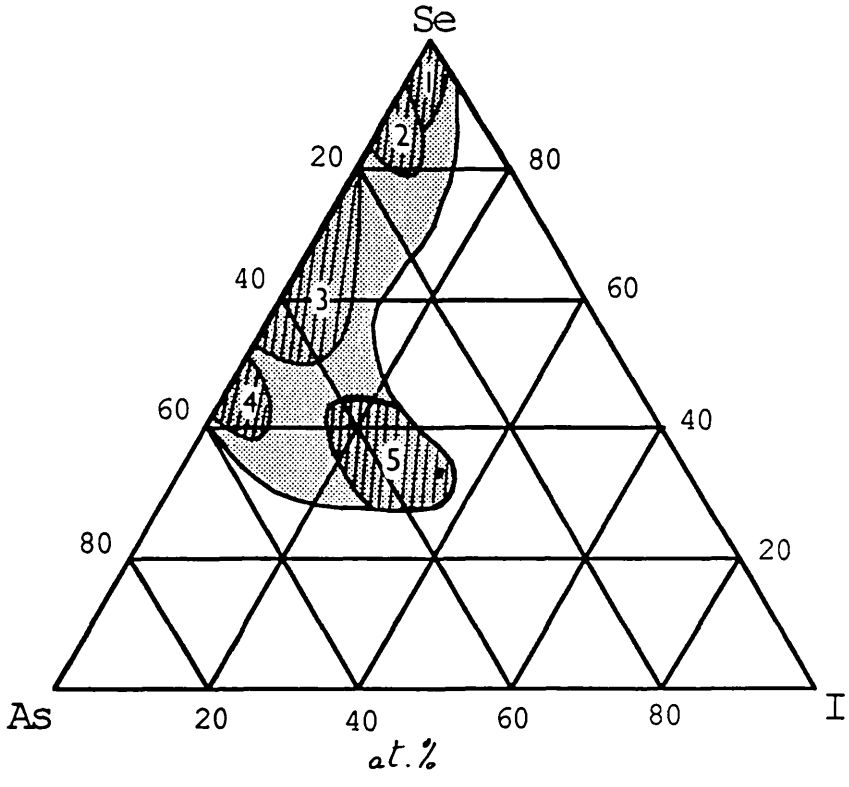


Figure 5.31: Subregions of As-Se-I glass formation with different structures

Ref. Khiminets et al (1978)

REGION 1: As < 2%; I < 10%

The glass is composed of Se_n chains and Se_8 rings in which groups containing As-I bonds are disseminated.

REGION 2: 2% < As < 20%; I < 10 at %

The glass is composed of Se_n chains joined by arsenic atoms; bonds of As with I are also present in them.

REGION 3: 22% < As < 45%; I < 15%

Formed by triangular pyramids of $AsSe_{3/2}$ in which bonds and angles, at the apices of the pyramids, differ slightly from the values for glassy arsenic triselenide due to the presence of iodine.

REGION 4: I < 15%; As:Se ratio ~1

Glass melts with a composition similar to the compound As_2Se_2 .

REGION 5: As > 30%; Se > 30%; I > 30%

Glass with an AS-Se-I chain structure similar to that of the glass forming As-S-I ternary compound, Figure 5.04.

Along the sections As_2Se_3 - AsI_3 and As_2Se_2 - As Se I , the ternary structural units of As Se I tend to be preserved down to As_2Se_3 or As_2Se_2 concentrations ~60 mole %, where bonds characteristic of these binary compounds are formed.

Experimental Details and Results

As-Se-I System

An initial study of the As-Se-I system was centred around the equiatomic composition. Samples were synthesised by directly reacting appropriate amounts of each element, using exactly the same techniques as for As-S-I compositions. Once again extreme care must be taken in handling the toxic elements; Selenium compounds are dangerous and may be absorbed in toxic quantities through the lungs, intestinal tract or damaged skin.

Three samples Se1, Se2 and Se3 were prepared with atomic compositions $As_{33}Se_{33}I_{33}$, $As_{41}Se_{33}I_{26}$ and $As_{33}Se_{41}I_{26}$ respectively. These compositions all lie within the ternary chain structure and are illustrated on the phase diagram, Figure 5.32.

In order to extract absorption data from the index experiments, the computer program was modified to record the threshold intensity values, as well as the resultant index at each wavelength. The threshold value is set at 85% of the peak intensity; therefore, by measuring the initial lamp intensities through the empty cell, the light absorbed by the sample may be extracted. Usually the prism used in index experiments gives a sample thickness of ~5 mm , thus the errors in measuring low absorptions is much less than in the thin layer absorption cell.

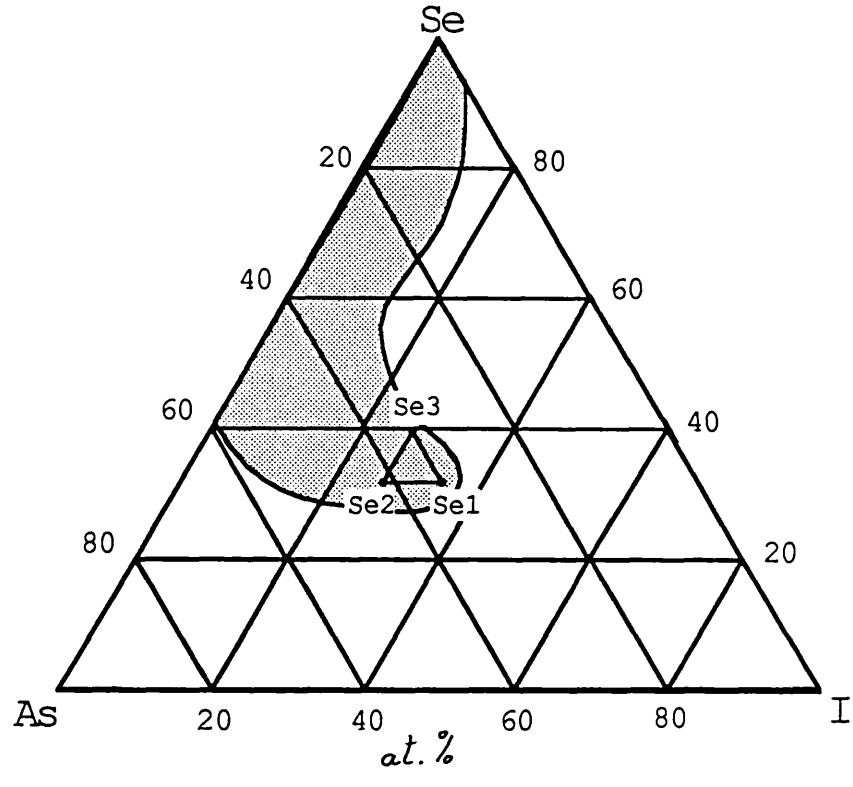


Figure 5.32: Initial three As-Se-I samples centred around the equiatomic composition.

The three samples were observed to melt down into the index cell between 150 deg. C. and 200 deg. C. although no transmission could be detected at these temperatures. With further heating a refracted beam could be detected and measurements were made; however, subsequent cooling once again causes a cut-off in transmission.

The index results for these three samples, together with the extracted absorption coefficient are shown in Figures 5.33 to 5.35. The absorption coefficients of a thin sample layer were also recorded, so that the reliability of extracting these coefficients during index measurements can be evaluated, Figure 5.33 (b). The two different ranges of these absorption measurements are due to the fact that the relatively thick sample of an index cell will not transmit sufficient light to measure absorption coefficients greater than ~10 cm^{-1} , whilst with a thin sample layer, the measurement of coefficients less than 10 cm^{-1} is dominated by errors due to noise fluctuations in the lamp intensity.

The range of temperatures over which measurements can be made is limited by two factors: at temperatures greater than about 400 deg. C., the peak transmitted lamp intensity drops and fluctuations in the index measurements, similar to those in the high temperature. As-S-I system, are observed. At low temperatures a much more sudden cut-off occurs as the sample is cooled. This cut-off seems to be reversible, with subsequent heating restoring the transmission. The nature of the cut-off is seen from the absorption measurements of Se6 to be similar to that observed for sample C and G in the

SAMPLE Se1

At.% Composition 33.3% As
33.3% Se
33.3% I

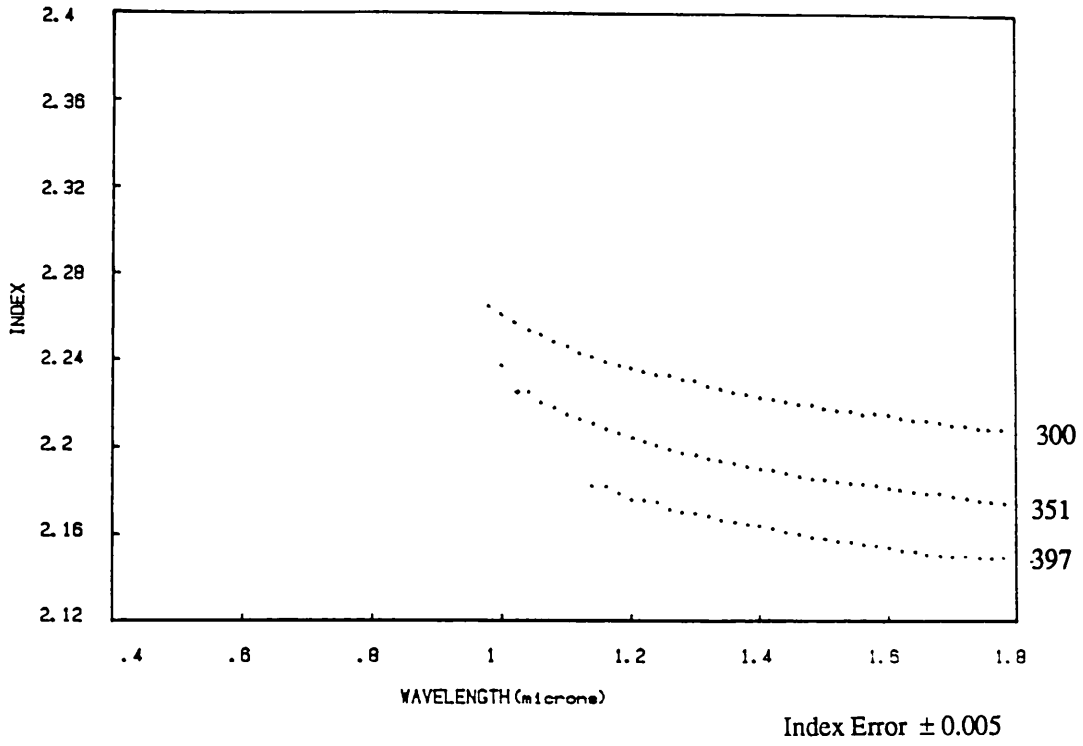


Figure 5.33(a): Refractive Index measurements.

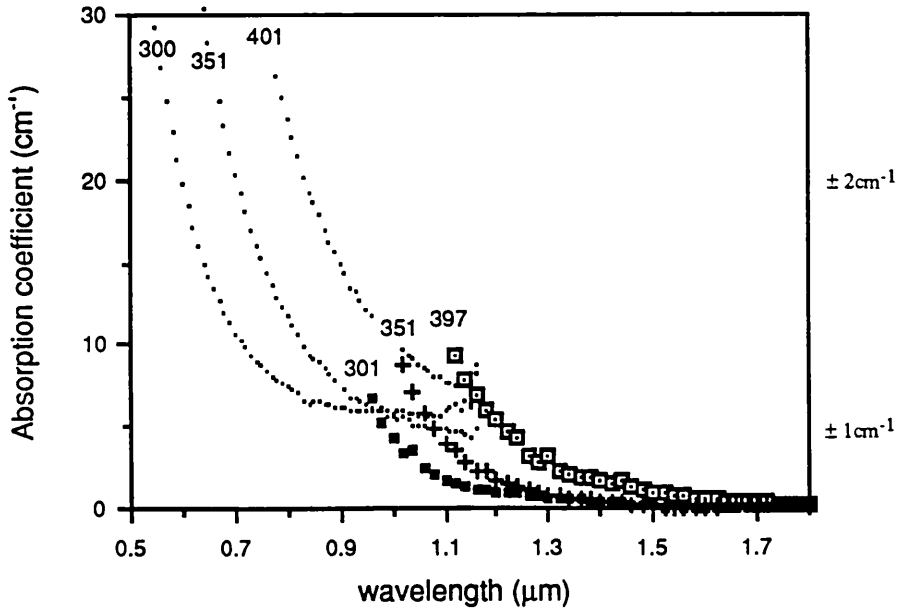


Figure 5.33(b): Comparison of index extracted absorption coefficents and thin sample measurements.

SAMPLE Se2

At.% Composition 41% As
33% Se
26% I

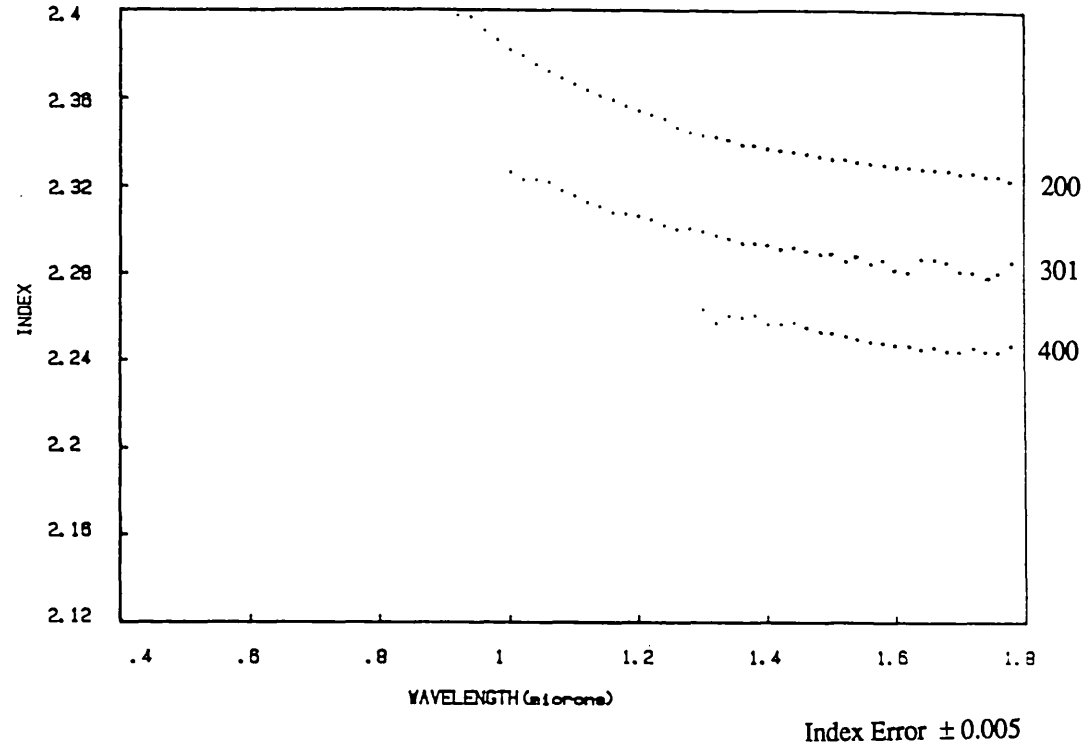


Figure 5.34(a): Refractive Index measurements.

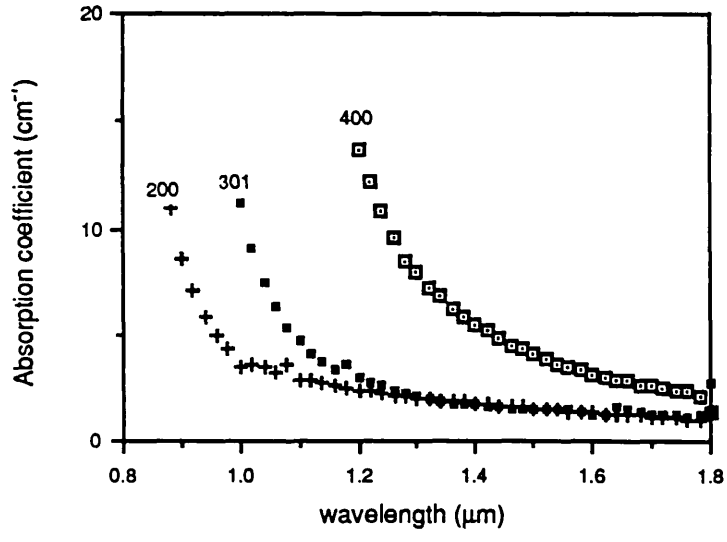


Figure 5.34(b): Absorption coefficients extracted from index experiment.

SAMPLE Se3

At.% Composition 33% As
41% Se
26% I

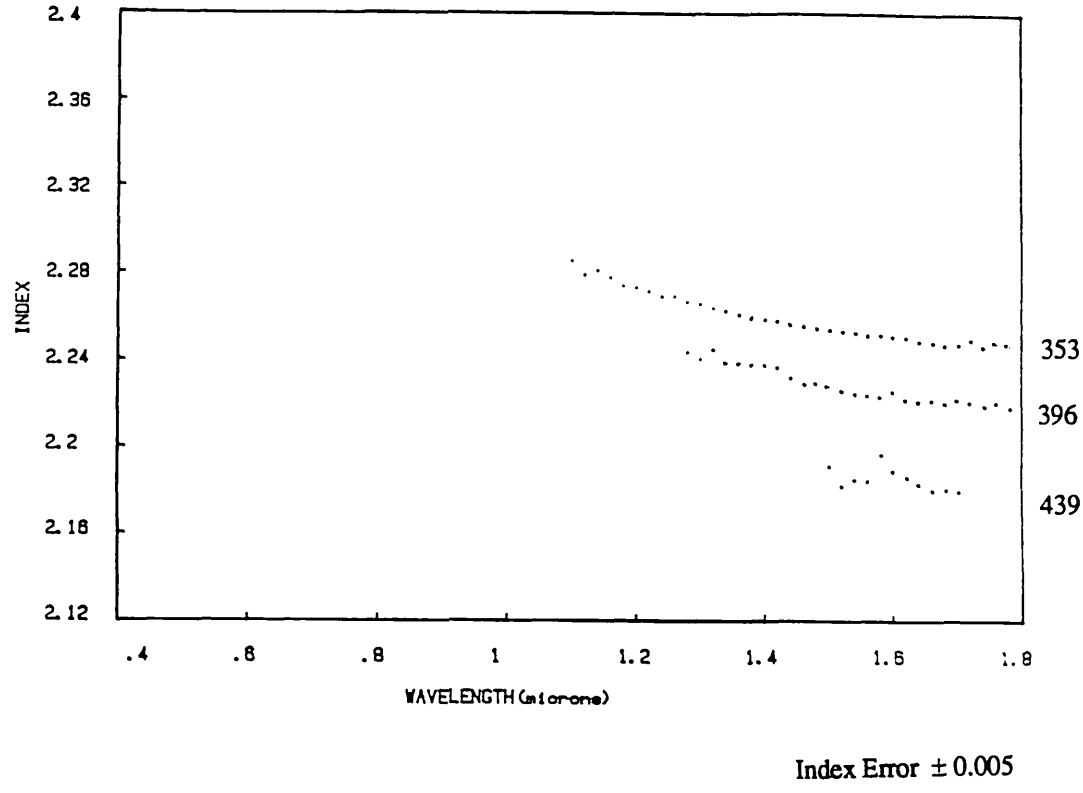


Figure 5.35(a): Refractive Index measurements.

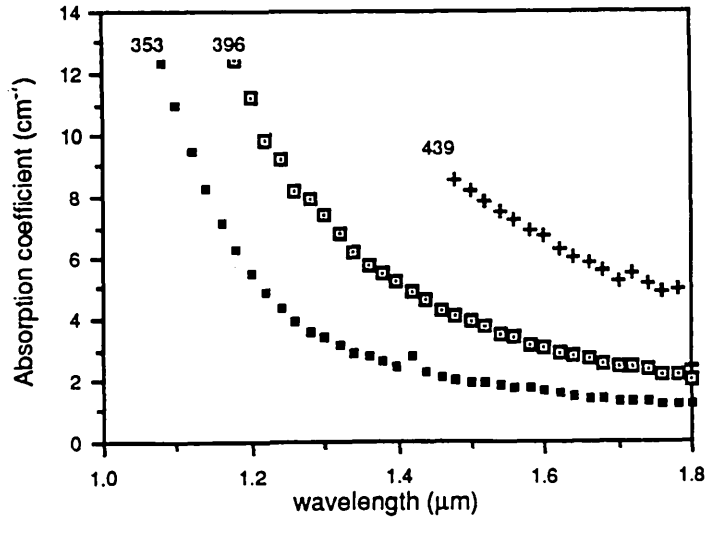


Figure 5.35(b): Absorption coefficients extracted from index experiment.

As-Se-I system (Figures 5.10 and 5.14). There is a constant shift of the absorption edge towards shorter wavelengths, whilst all the long wavelengths coefficients increase their absorption. Oxide impurities in arsenic selenide glasses were shown in chapter 4 to produce strong absorption bands, but since good transmission is found over certain temperature ranges, this is not thought to be the cause.

To investigate further the nature and dependency of this transmission cut-off, three more samples (Se4, Se5, Se6, Figure 5.36) with compositions $As_{47}Se_{33}I_{20}$, $As_{39}Se_{33}I_{28}$ and $As_{44}Se_{33}I_{23}$, were prepared. These samples were chosen with constant atomic percent selenium to enable the compositional dependence of the cut-off to be evaluated. The measured data and the transmission cut-off temperatures for these three samples are presented in Figures 5.37 (a) and (b).

Discussion

The range of temperatures at which measurements could be made was once again limited by a reversible transmission cut-off. The complete set of index data for samples Sel - Se6 can be summarized by plotting the measured index at 1.6 μm against temperature, Figure 5.38. Along the line of constant atomic percent selenium we may express the composition by $As_xSe_{33}I_{67-x}$ where x = 33,39,41,44,47. Figure 5.39

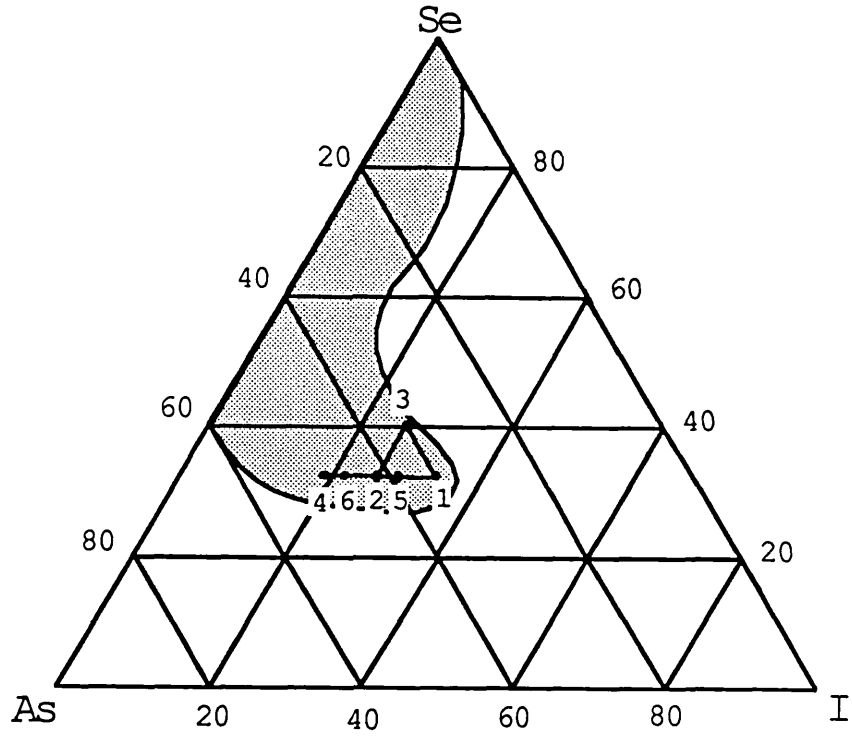


Figure 5.36: Compositions of the samples prepared to investigate the nature of the transmission cut-off temperature.

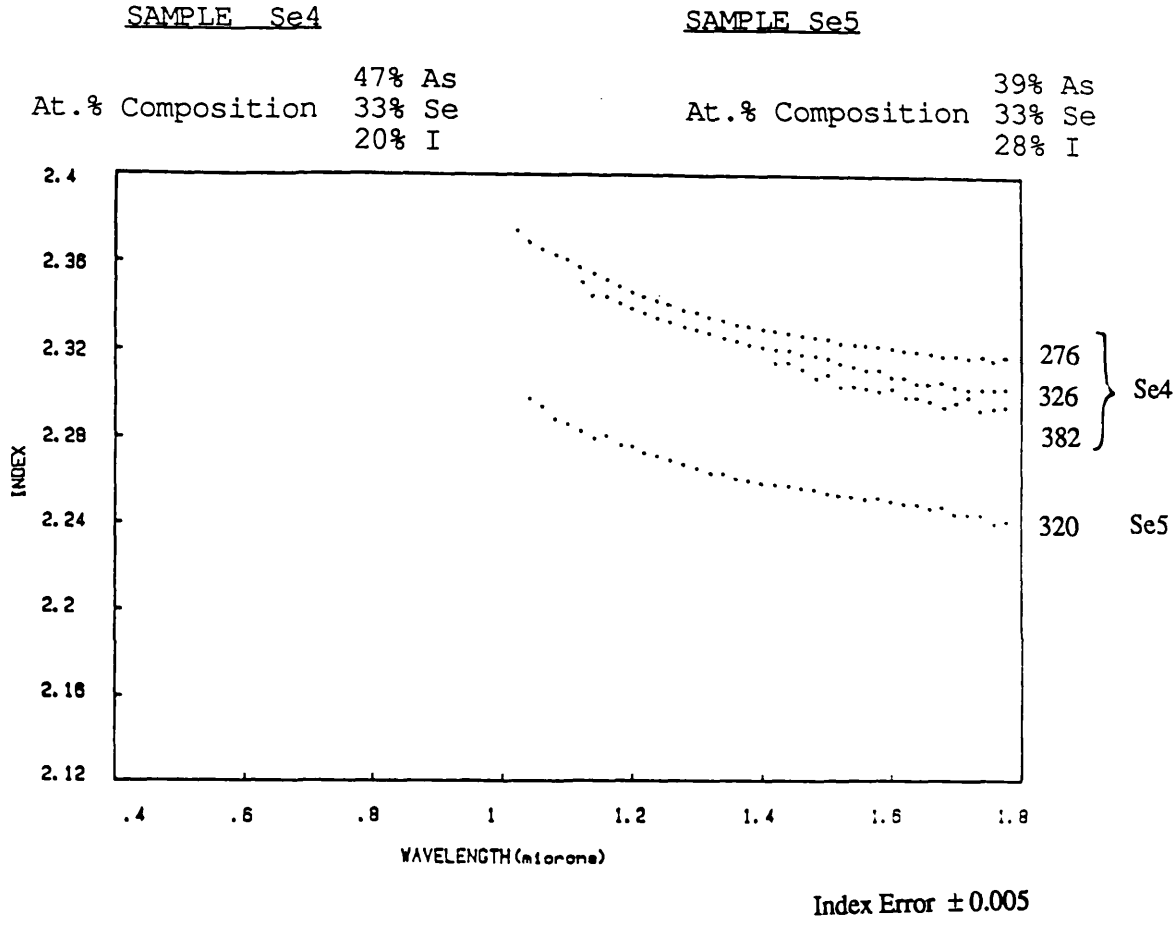


Figure 5.37(a): Refractive Index measurements for samples Se4 & Se5

SAMPLE Se6

At.% Composition
33% As
33% Se
33% I

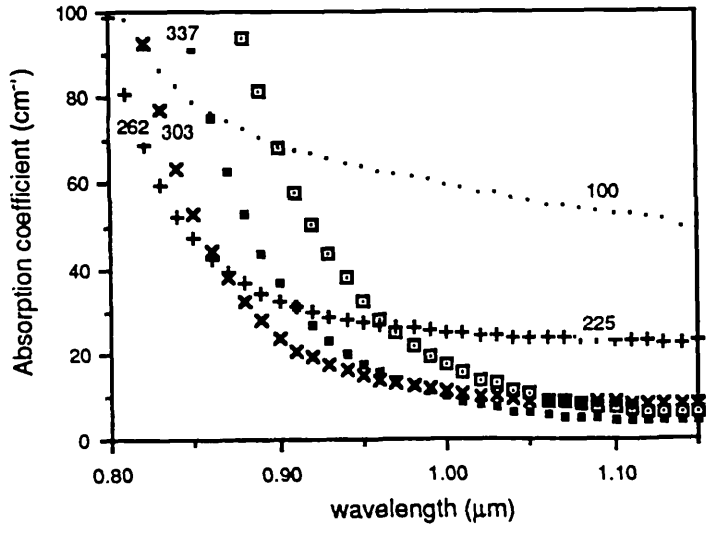


Figure 5.37(b): Absorption coefficients of sample Se6

shows both the index at 300 deg. C. (taken from Figure 5.38) and the transmission cut-off temperature, plotted as a function of arsenic composition x. The index is seen to increase linearly with arsenic composition, whilst the cut-off temperature is clearly not dependent on composition.

To study the heating and cooling effects on transmission, we measured the beam profile transmitted through the thin layer absorption cell of sample Se6. This profile normally has a width of 20'. At high temperatures (> 400 deg. C.) light is scattered within the sample, producing a drop in intensity, a broadening of the profile, and an increase in the background. As the sample cools, we observe a peak intensity followed by a rapid decline, during which there is no detectable increase in the beam width or the background intensities. Viewing the transmitted beam through an infrared converter confirms these observations, with no detectable scattering at lower temperatures whilst at high temperatures scattered light is observed from the entire sample. To show the reversibility of the transmission cut-off, we monitored the detected intensity at 1.4 μm, whilst heating and cooling the sample, Figure 5.40.

The observed cut-off in transmission was most likely due to the formation of a crystalline phase from the melt. Single crystals of the compound As Se I can be produced by very slow cooling (~ days) of As Se I melts. The structure of this phase As Se I was investigated by Kniep and Reski (1981) using X-ray diffraction, and is shown in Figure 5.41. To confirm such crystal formation a S.E.M and X-ray

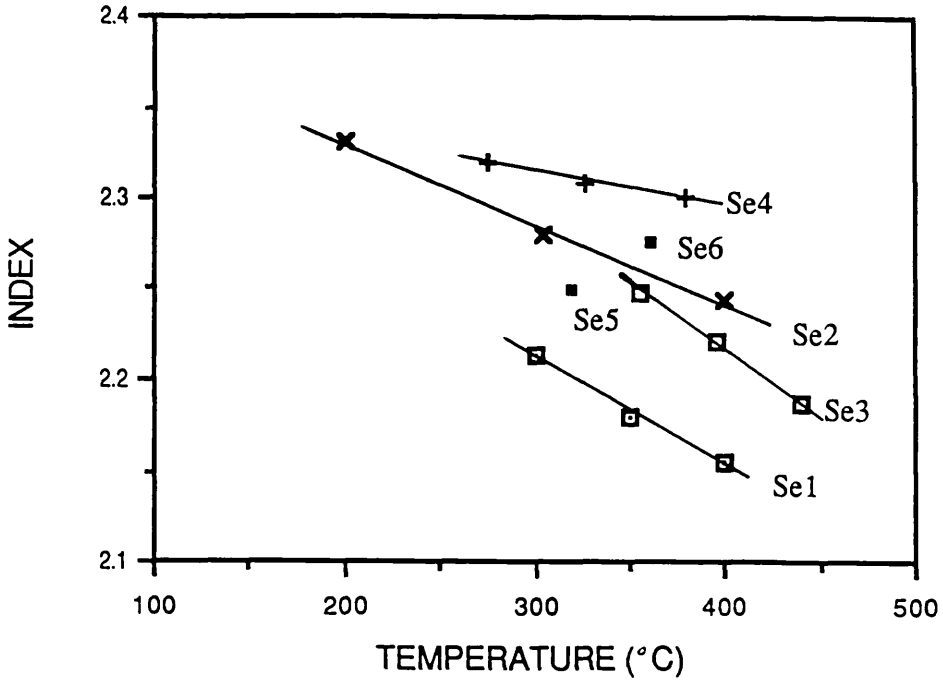


Figure 5.38: Summary of As-Se-I results; refractive index at 1.6 μm plotted as a function of temperature.

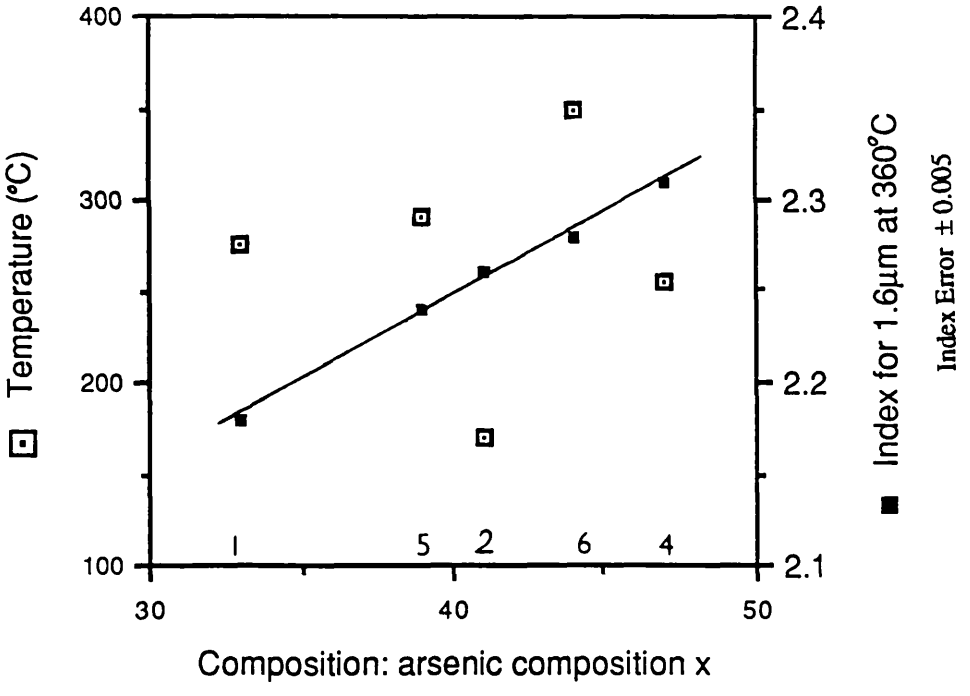


Figure 5.39: Composition dependence of the refractive index (at 300°C and 1.6 μm), and the cut-off temperature, ; for compositions $As_xSe_{33}I_{67-x}$ where x = 33,39,41,44,47.

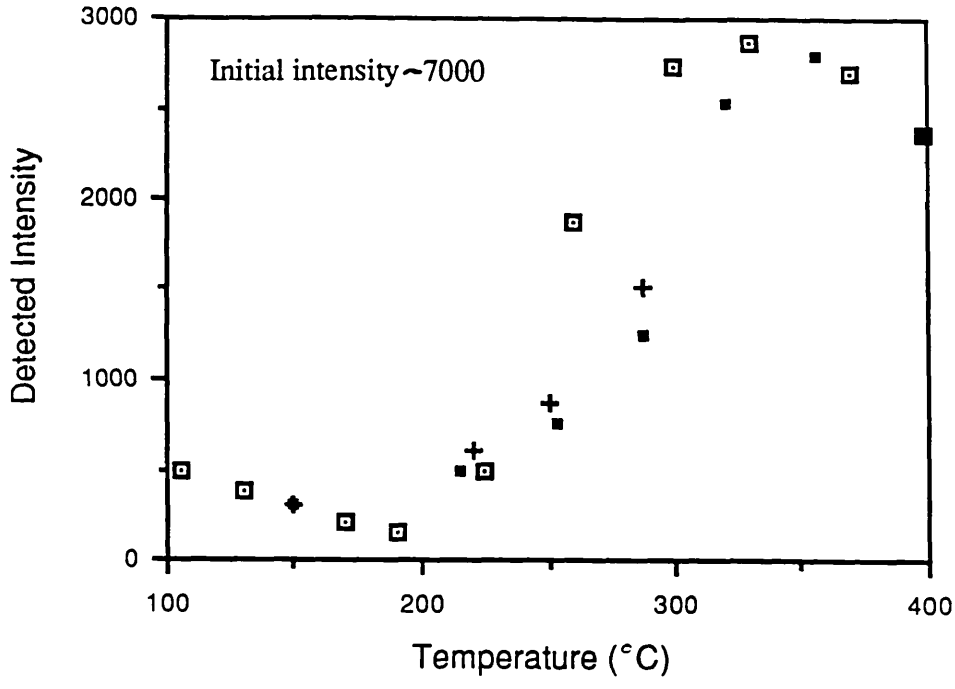


Figure 5.40: Heating/cooling curve for As-Se-I sample Se6 showing the reversibility of the transmission cut-off.

⊡ Initial Heating

■ Cooling

\+ Reheating

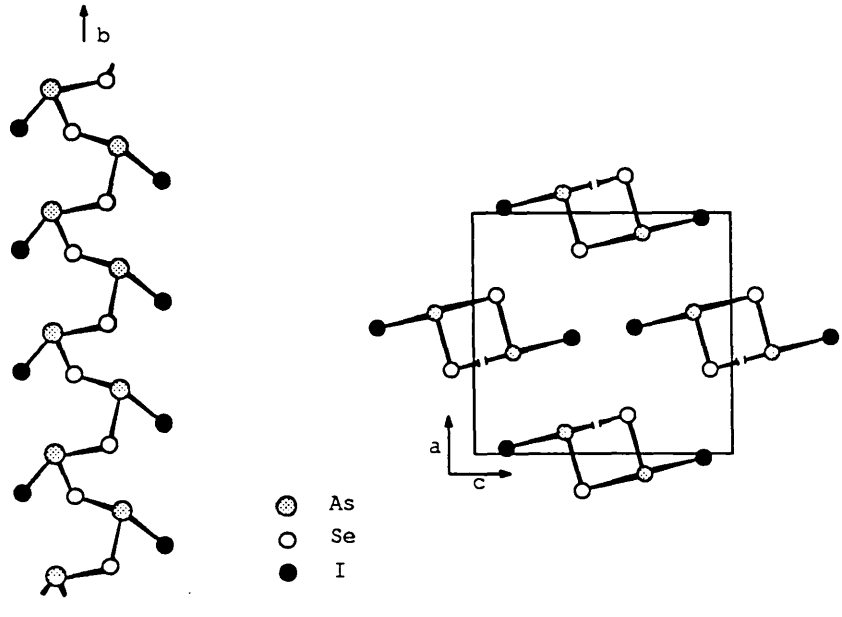


Figure 5.41: Structural units and their arrangement in crystalline As Se I (Ref. Kniep & Reski, 1981).

diffraction study of the samples was undertaken.

The very high magnification of a scanning electron microscope could not be achieved due to the local heating effect causing vapourisation. Holes, cracks and polishing scratches were observed but no evidence of any phase separation or crystallisation. The electron microscope's chemical analysis program (EDAX) did, however, provide a very useful check on the composition of these glasses.

TABLE 4

Sample	Intended Composition			Temperature Cut-Off	S.E.M. Analysis		
	As	Se	I	deg C	As	Se	I
Se1	33⅓	33⅓	33⅓	275	32	32	35
Se5	39	33	28	290	37	32	31
Se2	41	33	26	170	40	32	28
Se6	44	33	23	350	43	33	24
Se4	47	33	20	255	47	31	22

The X-ray diffraction analysis was carried out using a powder camera. The powder method is useful because single crystals are not required. Incident monochromatic radiation strikes the finely powdered specimen and diffraction occurs from individual crystallites which happen to be orientated with planes satisfying the Bragg equation. Figure 5.42 shows

the rings produced by sample Sel (Equiatomic As-Se-I). The several distinct rings all correspond to orders of diffraction from planar spacings given, for As Se I crystals, by Kniep and Reski (1981), thus showing these opaque samples contain some As Se I crystallites.

Comparison of Results

The only measurements with which to compare our results have been made by Russian workers on the equiatomic As Se I sample. Sample Sel has this same composition, however due to the transmission cut-off at 170 deg. C., all our results must be extrapolated down to room temperature.

From the rates of shift of absorption edge and index with temperature, and by using the measured dispersion properties, we can predict the optical properties of sample Sel:-

Sel (Composition $As_{33}Se_{33}I_{33}$)

Room Temperature	n =	(1.6 μm)
	n =	(1 μm)
	absorption edge	~0.8 μm

The position of the absorption edge given by Rodot et al (1971) {0.92 μm} and by Borets et al (1975) {0.88 μm} are both consistent with this prediction, as is the zero frequency refractive index value, 2.32, given by Borets (1983). The value of 2.48 (1 μm) from Zuban and Borets (1974) is obviously too high (as was their index value for As S I).

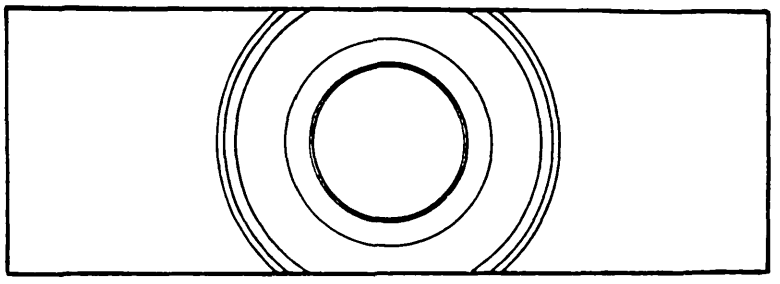


Figure 5.42: Position of X-ray diffraction rings from sample Se1.

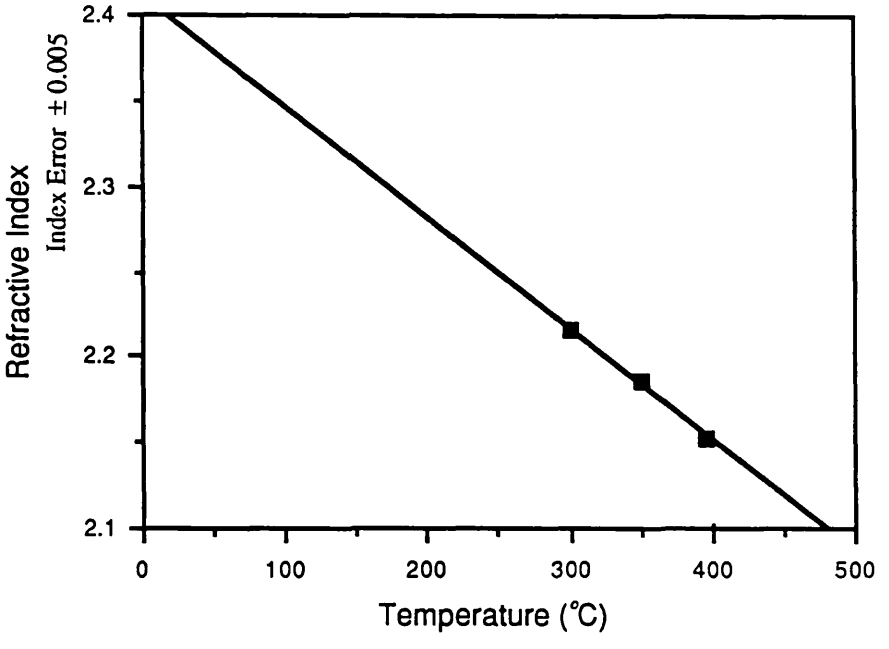


Figure 5.43: Extrapolation of index results for the equiatomic composition, Se1.

CHAPTER 6

SUMMARY AND CONCLUSIONS

Phosphorus Sesquisulphide with its low auto-ignition temperature and relatively high vapour pressure posed many technical and safety problems. These were eventually overcome by redesigning the heating block and enclosing the cell in an hermetically sealed box. The refractive index of molten P_4S_3 varies linearly with temperature from 1.90 (1 μm) at its melting point (173 deg. C.) to 1.78 (1 μm) at its boiling point (407 deg. C.). The dispersion is seen to follow the single oscillator dispersion equation of chapter 1, and by extrapolating the measured data we obtained the zero frequency refractive index, at the melting point, as 1.88. The absorption edge of P_4S_3 shows an exponential dependence on photon energy, with increasing temperature it shifts towards the red at a rate of 0.25 ± 0.05 meV/deg. C. Due to the difficulties in making measurements on molten P_4S_3, there is very little data with which to compare our results. One value for the density at the melting point is given by Mellor (1956) and this was used to calculate the molar refraction (56 ± 2 cm^3) and the electronic polarisability ($2.5 \pm 0.1 * 10^{-39}$ Fm^{-2}).

Arsenic-Sulphur-Iodine System: The ternary system of As-S-I glasses have a remarkable range of properties. In the region that we have studied, the melting point was found to

vary from 200 deg. C. to below room temperature, whilst the refractive index ranges from 1.92 to 2.32. The toxicity and vapour pressures of the synthesized glasses is much lower than that of the individual elements, thus making them relatively safe to handle. With the exception of two higher arsenic compositions, (samples C and G), the glasses remained transparent down to room temperature, although they did suffer from crazing and large thermal contraction. As the melts cooled, samples C and G were found to undergo a phase change, probably due to crystallisation. This reversible transition would cause a sudden cut-off in transmission, at a temperature dependent on the cooling rate. By increasing the cooling rate, the transition could be suppressed, so that a quench cooled sample formed a stable glass at room temperature. Quench cooled sample C would provide the highest practical refractive index in this As-S-I system and its value is predicted as ~2.32 (by extrapolation of index/temperature graph).

Measurements of sample density correspond very well to a compositional model of constant atomic number density. This shows that there is no gross structural changes over the range of compositions studied.

Arsenic-Selenium-Iodine System: A brief study of As-Se-I glass formation was made in the region of the equiatomic composition. The substitution of selenium for sulphur produced melts which have an absorption edge in the near

infrared and possess very high refractive indices (~ 2.3 at 200 deg. C.). When cooled, crystallites of As Se I form reversibly within the sample and produce a cut-off in transmission. Within the region of study, the cut-off temperature was found to be independent of composition and ranged from 170 to 350 deg. C.

Review of Other Low Melting Point Ternary Systems

The optical properties of As-S-Br glasses was studied by Fischer and Mason (1962). These glasses were yellow in colour and, compared to similar As-S-I compositions, they have higher softening temperatures, lower refractive indices and are less sensitive to moisture.

Flaschen et al (1960 b) investigated the physical properties of As-S-Tl and As-Se-Tl glasses. The molten glasses must be kept in a nitrogen atmosphere to avoid toxic fumes from oxidation effects. Their low temperature softening points, high fluidities and resistance to moisture make them useful as hermetic sealing compounds for electrical components. The structure of these glasses is probably similar to the As S I chain structure, so that the thallium acts as a monovalent chain terminator and effectively reduces the samples melting point. Infrared absorption measurements made by Frerichs (1953) show that an increasing thallium content rapidly shifts the absorption edge into the near infrared. The refractive indices of these

glasses is undoubtedly high, but its trade off with melting point, phase stability and edge shift has not been studied.

Suggestions for Further Work

With the safe confinement of toxic samples, our refractometer lends itself to studies of many liquids and melts for which data may be absent or unreliable.

Further investigations of low melting point ternary glasses would be useful to understand and extend the range of available properties. Multiple component systems could then be designed to optimise these optical and physical properties, giving uses in bulk optical materials and high refractive index immersion media.

In comparing the two systems, As-S-I and As-Se-I, one clear difference is the greater stability of the sulphide glass. This is consistent with the work of Kniep and Reski (1981), who found it much harder to produce single crystals of As S I. A study of this devitrification process would prove interesting but necessitates the use of a high temperature x-ray diffractometer.

REFERENCES

P. A. Akishen; N. G. Rambidi; Y. S. Ezhov
Russ. J. Inorg. Chem., 1960, 5, 358

J. R. Arnold
J. Chem. Phys., 1946, 14, 351

A. N. Borets
Ukr. Fiz. Zh., 1983, 28(9), 1346

A. N. Borets; P. P. Puga; D. V. Chepur
Ukr. Fiz. Zh., 1975, 20(2), 296

C.F. Callis; J. R. van Wazer; J. R. Shoolery; W. A. Anderson
J. Am. Chem. Soc., 1957, 79, 2719

T. P. Chattopadhyay; W. May, H. G. von Schnering;
G. S. Pawley
Zeitschrift fur Kristallographic, 1983, 165, 47

A. P. Chernov; S. A. Dembovskii; V. I. Makhova
Izv. Akad. Nauk. SSSR, Neorg. Mater., 1970, 6(4), 823

A. Donaldson
Ph.D Thesis, 1983

R. A. Dwek; D. E. Richards; D. Taylor; G. J. Penny;
G. M. Sheldrick
J. Chem. Soc. (A), 1969, 935

S. S. Flaschen; A. D. Pearson; W. R. Northover
J. Applied Phys., 1960 a, 31, 219

S. S. Flaschen; A. D. Pearson; W. R. Northover
J. Am. Ceram. Soc. 1960 b, 43, 274

A. G. Fischer; A. S. Mason
J. Opt. Soc. Am., 1962, 52, 721

R. Frerichs
J. Opt. Soc. Am., 1953, 43(12), 1153

M. Gardner
Chem. Soc. (Dalton), 1973, 691

V. S. Gerasimenko; V. V. Khiminets; O. V. Khiminets;
I. D. Turyanitsa
Fiz i Khim Stekla, 1977, 3(4), 343

A. R. Hilton
Applied Optics, 1966, 5(12), 1877

T. E. Hopkins; R. A. Pasternak; E. S. Gould; J. R. Herndon
J. Phys. Chem., 1962, 66, 733

V. V. Khiminets; V. S. Gerasimenko; O. V. Khiminets
Izv. Akad. Nauk SSSR, Neorg. Mater., 1983, 19(11), 62

L. Koudelka; M. Pisarcik
J. Non. Cry. Sol., 1984, 64, 87

R. Kniep; H. D. Reski
Angew. Chem. Int. Ed. Engl., 1981, 20, 212

Y. C. Leung; J. Waser; L. R. Roberts
Chem. Ind., 1955, 948

F. C. Lin; S. M. Ho
J. Am. Ceram. Soc., 1962, 46, 24

J. W. Mellor
A Comprehensive Treatise on Inorganic and Theoretical Chemistry, 1956

W. E. Moffitt
Trans. Faraday Soc., 1948, 44, 987

T. S. Moss
Optical Properties of Semi-Conductors, 1959

D. Palik
Handbook of Optical Constants of Solids, 1985

L. Pauling; M. Simonetta
J. Chem. Phys., 1952, 20(1), 29

Y. G. Poltavtsev
Izv. Akad. Nauk. SSSR, Neorg. Mater., 1975, 11(10), 1742

H. Rodot; A. Hruby; J. Horak
Czech. J. Phys. B, 1971, 21, 1213

M. T. Rogers; K. J. Gross
J. Am. Chem. Soc., 1952, 74, 5294

J. A. Savage; S. Nielsen
Infrared Phys., 1965, 5, 195

C. Schutz-Sellack
Ann. Phys. Chem., 1870, 139, 182ff

P. P. Seregin; P. P. Sivkov; F. S. Nasredinov;
L. N. Vasilev; Y. V. Krylnkov
Phys. Stat. Solidi A, 1977, 39(2), 437

F. Urbach
Phys. Rev.,1953, 92, 1324

S. H. Wemple; M. DiDomenico
Phys. Rev. Lett., 1969, 23(20), 1156

S. H. Wemple
Phys. Rev. B, 1973, 7(8), 3767

F. Wooten
Optical properties of Solids, 1972

V. A. Zuban; A. N. Borets
Ukr. Fiz. Zh., 1974, 19(2), 331

ACKNOWLEDGEMENTS

I wish to thank my supervisor, Dr. A. D. Caplin, who during the course of this work, has given me much advice, support and encouragement. In addition I would like to express my thanks to Dr. A. Donaldson, for giving me an excellent introduction to this project.

I would like to thank the technicians, academic staff and my fellow students, from both the Metal Physics and Optics Groups for their guidance, assistance and friendship.

The financial support of an industrial research grant is gratefully acknowledged.

Many thanks are especially due to my family, and to Miss D. Rogers, for their personal support, patience and encouragement.